ABSTRACT

Title of Dissertation: NEW NANOPARTICLE CHARACTERIZATION TECHNIQUES BY DIFFERENTIAL MOBILITY ANALYSIS

Kaleb Duelge, Doctor of Philosophy, 2022

Dissertation directed by: Professor Michael R. Zachariah, Department of Chemical and Biomolecular Engineering and Department of Chemistry and Biochemistry

Nanoparticles are being used increasingly in new fields for new applications. Thorough characterization of particle properties such as size, aggregation, and mass are key to understanding particle behavior. In this dissertation I discuss a variety of new measurement approaches using the aerosol-based technique: differential mobility analysis (DMAS). This technique consists of the combination (hyphenation) of several components, the primary being an ion mobility chamber for the spatial separation of nanoparticles. The specific aerosol source and detector used is flexible and allows for wide applicability of the technique.

The applications discussed here relate to a variety of everyday scenarios. Medicinal protein particles are studied to improve the health outcomes associated with this growing class of medicine. Nanoparticle catalysts are studied to improve the activity and repeatability, analogous to how a catalytic converter is used in cars to reduce combustion emissions. Detailed size measurements are made for gold nanoparticles, a class of particles that have been used for cancer

treatments and as carrier particles, for example to transport medicine to a particular location within the body. Finally, determination of nanoparticle size is studied by comparing results from different instruments, as determining size in the nanometer scale is more complicated than an analogous measurement of a macroscopic sphere (for example, measuring the length with a ruler and comparing the result to the length derived from the mass of a sphere with a known density).

In the second chapter, I demonstrate protein aggregation kinetics measurements by DMAS and asymmetrical flow field flow fractionation. Thermal aggregation was conducted in traditional formulation buffers and good agreement was determined between the two techniques. These are potential alternative instruments to the gold standard, size exclusion chromatography, used by the biopharmaceutical industry.

In the third chapter, I demonstrate a calibration technique for mass distribution measurements by DMAS using inductively coupled plasma mass spectrometry for detection. Determination of the total mass of a sprayed ionic standard was sufficient to calibrate measurements of monodisperse gold nanoparticles of various shapes. A disagreement was determined between the ionic standard and a polydisperse distribution of titania coated with small gold nanoparticles. A multiple charge correction was applied that significantly improved the agreement, though the issue remained.

In the fourth chapter, comparison measurements are presented for monodisperse gold nanoparticles made in two operational modes of DMAS: step voltage mode and scan voltage mode. The step voltage mode remains at each voltage for a certain dwell time (on the order of 30 s), while the scan voltage mode continuously changes voltages. Good agreement was determined for the two approaches when calibrated using a nanoparticle size standard. Additionally, the scan voltage mode data were analyzed with an alternative calibration method: a direct measurement of the

sheath volumetric flow rate. The data from the two scan voltage mode calibrations bracket the measurement made in step voltage mode. This agreement suggests that scan voltage mode measurements for certification of nanoparticle size standards could be used in the future if a few additional uncertainty terms are explored.

In the fifth chapter, traceable measurements with quantitative uncertainty analyses are compared for a size standard. The measurement by DMAS is compared to atomic force microscopy, scanning electron microscopy, and electro-gravitational aerosol balance. The measurement by DMAS was bracketed by the other techniques, with microscopy measuring a slightly smaller size and electro-gravitational aerosol balance measuring a slightly larger size. The measurements all agreed within 3%, but some of the differences exceeded the 95% confidence intervals of the measurements. These differences may be significant if these techniques are used to develop future size standards.

# NEW NANOPARTICLE CHARACTERIZATION TECHNIQUES BY DIFFERENTIAL MOBILITY ANALYSIS

by

Kaleb Duelge

Dissertation submitted to the Faculty of the Graduate School of the
University of Maryland, College Park, in partial fulfillment
Of the requirements for the degree of
Doctor of Philosophy
2022

Advisory Committee:
Professor Michael R. Zachariah, Chair
Professor Philip R. DeShong
Professor Lyle D. Issacs
Professor Peter Nemes
Professor Raymond J. Phaneuf

©Copyright by
Kaleb Duelge
2022

## Acknowledgements

I would like to thank Dr. Michael R. Zachariah for his continued support and guidance over the years and his generous funding of my research. Dr. Vincent Hackley helped me to transition to NIST and shared a variety of ideas and useful opportunities. Dr. George Mulholland is a great mentor and constantly taught me about new aspects of aerosol science. Dr. John Pettibone generously chose to collaborate with me and introduced me to nanoparticle catalysts. Dr. Jeremie Parot contributed AF4 measurements and was always available to commiserate and discuss research ideas during our hundreds of hours in the lab together. Dr. Justin Gorham is a very responsive group leader and helped me with funding when my writing took longer than expected. Dr. Tae Joon Cho helped me with nanoparticle synthesis issues. Dr. Scott Brown introduced me to the industry perspective on research and shared the stunning power of Teflon tape with me. Dr. Tom Cleary graciously shared his aerosol instrumentation for troubleshooting purposes and calibration. Dr. Natalia Farkas and Dr. John Kramar contributed SEM and AFM measurements and useful discussion. Dr. Keiji Takahata shared the JSR SC-010-S particles and relevant data. Dr. Antonio R. Montoro Bustos provided sp-ICP-MS data and expertise. Dr. Jiaojie Tan introduced me to the DMA and helped me start my first project. Dr. Philip R. DeShong, Dr. Lyle D. Issacs, Dr. Peter Nemes, and Dr. Raymond J. Phaneuf all committed their time and effort to help improve this dissertation. This work was supported in part by a grant from the National Institute of Standards and Technology, Materials Measurement Science Division (Award No. 70NANB17H057).

Finally, I would like to thank my non-work friends, my parents, my amazing partner: To-Lam, and To-Lam's parents. Without your continued support I would not be where I am today.

# Table of Contents

# List of Figures

# List of Tables

# List of Abbreviations

DMAS – Differential mobility analysis
mRNA – Messenger ribonucleic acid
MALS – Multi-angle light scattering
DLS – Dynamic light scattering
SAXS – Small angle x-ray scattering
UV-Vis – Ultraviolet-visible light absorbance
SEM – Scanning electron microscopy
TEM – Transmission electron microscopy
AFM – Atomic force microscopy
NTA – Nanoparticle tracking analysis
SEC – Size exclusion chromatography
AF4 – Asymmetrical flow field flow fractionation
AUC – Analytical ultracentrifugation
Sp-ICP-MS – Single particle inductively coupled plasma mass spectrometry
DMA – Differential mobility analyzer
nES – Nano electrospray
CPC – Condensation particle counter
ICP-MS – Inductively coupled plasma mass spectrometry
GED – Gas exchange device
NIST – National institute of standards and technology
IgG – Immunoglobulin G
MacroIMS – Macro-ion mobility spectrometer
SMPS – Scanning mobility particle sizer
GEMMA – Gas-phase electrophoretic mobility molecular analyzer
BSA – Bovine serum albumin
α-chymo – α-chymotrypsinogen
AuNP – Gold nanoparticle
Au@$TiO_2$ – Gold nanoparticles adsorbed to titania nanoparticles
AuNR – Gold nanorods
AuNC – Gold nanocubes
Pt@AuNP – Platinum coated gold nanoparticle
SRM – Standard reference material
QC1 – Quality control 1, 30 nm gold nanoparticles
QC2 – Quality control 2, 60 nm gold nanoparticles
RM – Reference material
CV – Coefficient of variation
SI – International system of units
PSL – Polystyrene latex
EAB – Electro-gravitational aerosol balance
NMIJ – National metrology institute of Japan

# Chapter 1: Introduction

## *1.1 Determining Nanoparticle Size*

Nanotechnology is an important component of modern society. It is in our electronics, cosmetics, transportation, medicine, imaging, and industrial processes. A timely example is the mRNA-based COVID-19 vaccines which are contained in nanoparticle liposomal carriers on the order of 100 nm.[1] The liposomes are key components in the formulation, as they significantly improve the delivery of mRNA to cells.[2] Nanoparticles are in the air we breathe and the water we drink, and they can have negative health impacts. I use the definition that a nanoparticle is any particle between 1 nm and 100 nm in size (though some agencies alternatively call this the mesoscale). This definition is a bit vague and leads to another immediate question: what does particle size mean? For spheroidal particles we consider particles in terms of a sphere-equivalence, or, in other words, the diameter of a sphere with the same value of the property of interest (such as electrical mobility) as the actual particle. There are many ways to measure particle diameter, and these will be discussed presently. Many instruments measure a particle diameter, but the specific type of diameter being measured is not always the same. For example, the hydrodynamic diameter which refers to the nanoparticle dispersed in liquid and the surrounding layer of fluid that travels with it. This stands in contrast to the core diameter, which refers only to the nanoparticle. There are area-, mass-, and volume-equivalent-diameters, which refer to diameters derived from alternative properties. These different forms of diameter are important for different applications. The hydrodynamic diameter is an important feature to determine the fate of nanoparticles in the human body. Particles below 10 nm tend to be rapidly cleared by the kidneys[3], while larger particles are cleared by the reticuloendothelial system. Also, particles within the human body are rapidly coated with protein, and the composition of this protein coating (often called a corona) is

dependent on the size of the nanoparticle.[4] This is likely one mechanism by which the fate of nanoparticle in the body is determined, as the corona determines interactions between the nanoparticle and the body. Other properties are also important to the functionality of particles. One example is surface chemistry. In the case of particles in the human body, nanoparticles coated in polyethylene glycol tend to be ignored by macrophages and are cleared more slowly from the body. Other features include shape, homogeneity, density, aggregation state, surface charge, and concentration. Some of these features tie back to the primary feature, size. For example, the aggregation of a population of particles can be quantified by temporal size measurements. Nanotechnology is a growing industry because nanoparticles tend to have different properties from bulk material. The same can be said for microscale particles, though the differences in behavior tend to increase as the particle size decreases. This is because the surface-to-volume ratio is much larger for nanoparticles than for larger particles, and these strained surface atoms behave differently from the bulk. Also, quantum confinement effects are important for electro-optics, and exclusion of extended defects are important for mechanical properties. Size measurements are the focus of this dissertation, as particle size is a key parameter for many characteristics of interest.

### *1.2 Potential Instrumentation*

There are many approaches to measuring the size of nanoparticles. There are light scattering techniques, such as multi-angle light scattering (MALS) and dynamic light scattering (DLS), which determine the particle size based on interactions with light. Particles of different sizes tend to scatter light in different directions, for example small particles scatter light in all directions while larger particles tend to scatter primarily in the forward direction (away from the light source). The Rayleigh-Gans approximation can characterize particles smaller than the

wavelength of light, while the Lorenz-Mie electromagnetic theory is used for larger particles.[5] Small angle light scattering measurements can be used to determine the radius of gyration that reflects the average radial distance to the center of mass. Small angle x-ray scattering (SAXS) is a similar technique that uses x-rays as the light source. The scattered light intensity is measured at various angles, and the angular information is presented as a scattering modulus, $q$, based on the wavelength of the light source. Models applied to this raw data can determined a volume-weighted diameter distribution.[6] An alternative measurand from electromagnetic theory is light absorption, where the energy from light is taken up by a sample. For nanoparticles, the surface electrons of the particle collectively oscillate when they interact with light of specific energies. The ultraviolet-visible light absorbance (UV-Vis) band of nanoparticles shifts to longer wavelength as the size increases. Absorbance measurements are additionally dependent on particle shape, distance between particles, and the dielectric function of the medium, so these measurements alone are not sufficient to convey size information.[7] Dynamic light scattering (DLS) measures temporal changes to scattered light intensity at a particular angle and relates this value to the diffusion coefficient for particles. This value can then be related to the hydrodynamic diameter of the particle. Multiple scattering, in which the scattered light from one particle is then scattered by a second particle before reaching the detector, is an issue for this class of measurement methods and sets the maximum concentration that can be measured. These examples illustrate how interactions with light can be used to determine particle size information.

There are microscopic techniques such as scanning electron microscopy (SEM) and transmission electron microscopy (TEM) that measure cross sections of particles based on interactions with an electron beam. These techniques measure an area-equivalent diameter and tend to measure the core particle because the image contrast is related to atomic mass (metal

particles have high contrast compared to the surrounding carbon grid). A key advantage is that microscopy also collects shape information. However, these measurements are made under high vacuum, which can influence some particles, and beam damage is a persistent issue.[8] Tomographic methods and imaging at various tilt angles can be used to compile three dimensional representations of particles. Atomic force microscopy (AFM) measures particle height or length by displacement of a probe tip scanning across a surface. Significant corrections and experience are required to use the probe tips properly.[9] All microscopy techniques tend to be limited in terms of sample size (field of view and number of images), as it is difficult to measure sufficient number of particles to properly represent the entire population. Advances in measurement and data analysis automation are improving, however.

Nanoparticle tracking analysis (NTA) measures the trajectories of particles diffusing in solution and determines a hydrodynamic diameter. A laser is used to illuminate the nanoparticle suspension and a microscope focuses the light onto a camera. Both NTA and DLS determine a hydrodynamic diameter, but a number distribution is gathered by NTA, while DLS is an ensemble measurement.

There are chromatographic techniques, such as size exclusion chromatography (SEC), that separate particles based on the ability to enter small pore spaces. Asymmetrical flow field flow fractionation (AF4) separates particles by differential flow in a parabolic flow profile. These are commonly used to study bionanoparticles and measure the hydrodynamic diameter, but they are limited by column or channel health (the ability to separate particles as expected by theory), as these tend to clog and fail over time and need to be cleaned regularly. Also, particles are separated by size, but determining the size of an unknown particle based only on elution time is nontrivial.

Generally, AF4 is used as a separation technique and coupled with online detectors such as MALS and DLS to determine particle size.

Analytical ultracentrifugation (AUC) separates particles based on their mass by the centrifugal force. More massive particles reach the bottom of the container faster and are detected by optical techniques such as UV-Vis absorption spectrometry or interferometry. The hydrodynamic diameter is determined from the sedimentation coefficient, a proportionality constant that relates the mass transport of a sample to the surface area and the magnitude of the centrifugal field. A key advantage is that this technique does not rely on chromatographic separation, though the calculations do require some knowledge of system parameter such as particle density.[10] Finally, single particle inductively coupled plasma mass spectrometry (sp-ICP-MS) can be used to determine a number-weighted mass distribution. A dilute aerosol is broken apart into component atoms by a plasma and the mass concentration of different elements can be determined. The key distinction from more common ICP-MS measurements is that rapid measurements, on the order of ms, are made of individual nanoparticles entering the plasma. Calibrating with a nanoparticle of known mass allows for mass measurements one nanoparticles at a time.

There are many approaches to measuring particle size, and different techniques measure different sizes in different ways. Each technique has inherent advantages and disadvantages. Some of the measurements are *in situ*, measuring the particles in their native environment, such as MALS, DLS, SAXS, AF4, and AUC. Other measurements require a transition to a different phase and therefore incur some uncertainty as to the relationship between the measured particle and the native particle. Also, some measurements detect individual particles, such as microscopy and sp-ICP-MS, and on the other hand, there are measurements such as MALS and DLS that only

determine an average particle size. Between these two extremes, there are techniques such as AF4 and SEC that make bulk measurements after size separation and thereby reduce the uncertainty associated with measuring an entire size distribution simultaneously. Each type has advantages and disadvantages, though generally the measurement of individual particles is ideal if sufficient particles are measured. In this case, I chose to work with another technique not yet described: differential mobility analysis.

### *1.3 Differential Mobility Analyzer*

Differential mobility analysis (DMAS) is a technique consisting of several parts. The primary component is the differential mobility analyzer (DMA), a column used to separate aerosols by mobility. The mobility ($Z_p$) of a particle is the speed at which it travels within an applied field, in this case, an electric field.

$$Z_p = \frac{v}{E} \tag{1.1}$$

The balance of the electrostatic force and drag force determines the velocity of charged particles.

$$Z_p = \frac{neC_c(D_p)}{3\pi\mu D_p} \tag{1.2}$$

$n$ is the number of charges, $e$ is the elementary charge, $C_c$ is the Cunningham slip correction (described below), $\mu$ is the viscosity of the gas, and $D_p$ is the mobility diameter. The mobility diameter is the diameter of a sphere with the same mobility as the actual particle. As the drag force has a diameter dependence ($D_p^1$ in the continuum regime and $D_p^2$ in the free molecular regime), it is possible to determine a particle diameter from a measured mobility.

Based on the cylindrical geometry of the DMA (with a cross section shown in Figure 1.1), an explicit expression for the mobility of a particle that exits the DMA at the centroid of the DMA transfer function can be determined.[11]

$$Z_p = \frac{q_{sh} \ln (r_2/r_1)}{2\pi LV} \tag{1.3}$$

$q_{sh}$ is the sheath flow rate, $r_2$ is the outer electrode radius, $r_1$ is the inner electrode radius, $L$ is the length of the DMA from entrance slit to exit slit, and $V$ is the voltage of the inner electrode (relative to the grounded outer electrode). The sheath flow is the carrier flow that moves the particles from the top of the chamber to the bottom. Combining Equations 1.2 and 1.3 gives the key equation for determining diameter by this instrument.

$$\frac{D_p}{C_c(D_p)} = \frac{2neLV}{3\mu q_{sh} \ln (r_2/r_1)} \tag{1.4}$$

Many of these terms are fixed, so for a given geometry and volumetric flow rate, a series of voltages are applied to determine a size distribution. Figure 1.1 illustrates how particle size affects the particle trajectory through the DMA.

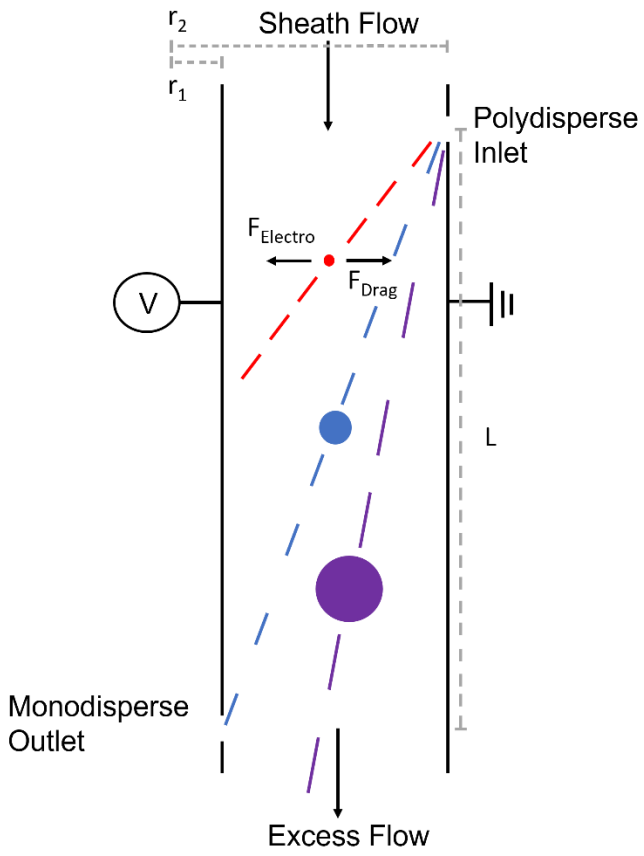


**Figure 1.1:** Schematic of a vertical cross section of the coaxial separation zone of the DMA. A polydisperse aerosol enters the DMA inlet and experiences electrostatic attraction toward the inner electrode and drag towards the outer electrode. Only particles within a narrow mobility diameter range will reach the DMA outlet and continue to the detector.

The Cunningham slip correction, $C_c$, is an empirical correction for the changing relationship between diameter and the drag force.

$$C_C(D_p) = 1 + K_n[\alpha + \beta \exp(-\gamma/K_n)] \quad (1.5)$$

$\alpha$, $\beta$, and $\gamma$ are empirical constants. The first order approximation of the drag force assumes no slip at the surface of the particle (the relative velocity of the gas at the surface of the sphere is zero), which is true when the particle is much larger than the gas molecules, because the gas acts as a uniform, viscous fluid. However, as the particle size decreases to approach the size of the gas

molecules, the drag force is determined by collisions with individual gas particles and the "no slip" approximation does not hold.[12] The slip correction is dependent on the Knudsen number, $K_n$, which is a relationship between the mean free path of the gas ($\lambda$) and the diameter of the particle.

$$K_n = \frac{2\lambda}{D_p} \tag{1.6}$$

The mean free path of the gas is the average distance a gas molecule travels before it collides with another gas molecule. This value is not directly measured but is calculated from the kinetic theory relationship for viscosity. Temperature and pressure measurements are needed to accurately determine the gas viscosity and mean free path.

$$\mu = \mu_0 \left(\frac{T}{T_0}\right)^{1.5} \left(\frac{T_0 + 110.4\ K}{T + 110.4\ K}\right) \tag{1.7}$$

$$\lambda = \lambda_0 \left(\frac{T}{T_0}\right) \left(\frac{P_0}{P}\right) \left(\frac{1 + (110.4\ K)/T_0}{1 + (110.4\ K)/T}\right) \tag{1.8}$$

$\mu$ is the gas viscosity at a given temperature, $\mu_0$ is the gas viscosity, 1.832 x $10^{-5}$ kg $m^{-1}$ $s^{-1}$, at standard temperature, $T$ is the temperature in Kelvin, $T_0$ is the standard temperature: 296.15 K, $\lambda_0$ is the mean free path (67.3 nm) at standard temperature and pressure, $P$ is the pressure, and $P_0$ is the standard pressure: 101.33 kPa.[13,14]

Initial electrical mobility measurements were made for atmospheric studies in the early 1900s.[15] Along a similar vein, the first particle size distribution measurements were made in 1923. The first DMA was developed in 1957 for climate studies of sub-micrometer particles.[16] The DMA was then used with a bipolar charger to produce monodisperse aerosols of known size. This work led to the first commercial DMA in the 1970s. The initial design was modified and optimized and the relationship between the classifier parameters and the mobility and transfer function was

derived. A data inversion method for determining aerosol size distributions based on the measured particle mobility distribution was then developed.[11] In 1989, a scanning electrical mobility spectrometer was developed, in which the mobility selecting voltage is changed continuously.[17] This allowed for much faster measurements of particle size distributions. In 1997 the nano DMA was developed, which has a shorter column optimized for particles in the 3 nm – 50 nm size range.[18] Advances with electrospray allowed for the measurement of smaller particles, and measurements of proteins were demonstrated.[19] This was followed by a burst of studies on bionanoparticles and engineered nanoparticles such as transition metal nanoparticles.[20,21,22]

## *1.4 Aerosol Sources*

Another component of DMAS is an aerosol source. Since DMAS is an aerosol technique and the particles of interest in this dissertation are colloids (nanoparticles dispersed in liquid), a spray technique is needed to transition from solid particles in a liquid to solid particles in a gas. Two of the most common techniques are electrospray and nebulization. Electrospray applies an electric field to the tip of a capillary transmitting a conductive fluid. The droplets that exit the spray chamber are monodisperse with diameters on the order of hundreds of nanometers, which is ideal for aerosol size measurements of nanoparticles. Alternatively, nebulization relies on a jet of air to disrupt the fluid and produces polydisperse droplets on the order of a few micrometers. Nebulization tends to be more stable and has fewer sample requirements.

### *1.4.1 Electrospray*

The foundation of electrospray was discovered by Taylor in 1964.[23] Studies of droplet disintegration were previously of interest due to relevance to thunderstorms and early studies led to some understanding of the behavior of conductive fluids in strong electric fields. Droplets

tended to deform when exiting a capillary with a strong electric field applied to the tip. Taylor demonstrated that the balance of surface tension and the electrostatic force can result in a characteristic conical shape, known as a Taylor cone. This stable spray zone emits a meniscus, a narrow stream of fluid on the order of a micrometer in diameter, that can disintegrate into a steady stream of small droplets depending on the spray mode. Based on this significant finding, electrospray units were designed. They consist of a capillary to transmit fluid, where either the capillary or the fluid must be conductive, and a voltage applied to the tip. A grounded metal plate, often with a ring geometry, is used to direct the produced droplets as shown in Figure 1.2. The spray mode is determined by a variety of factors, such as the applied voltage, the liquid flow rate, and the capillary tip geometry. Some mechanism is required to force the fluid through the capillary, generally this involves either a syringe pump or a pressurized chamber at one end of the capillary.

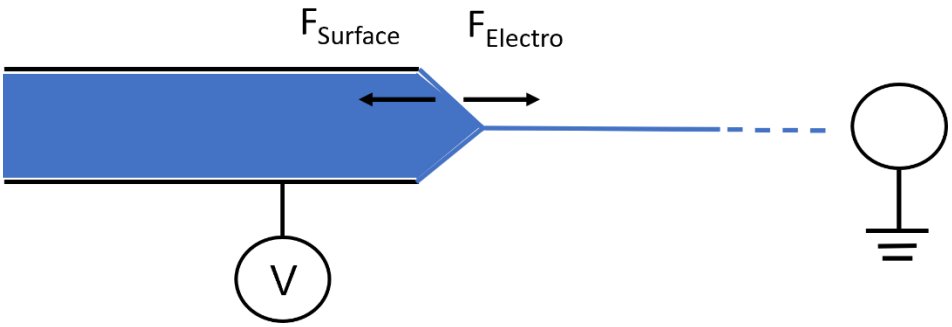


**Figure 1.2:** A capillary with an applied voltage carries liquid to a tip where the balance of surface tension and the electrostatic force result in the formation of a Taylor cone and the generation of small droplets directed to a grounded exit ring.

Electrospray is a technique commonly used for mobility measurements, though it is also used for a variety of other techniques such as mass spectrometry. The nano electrospray (nES), an electrospray with a liquid flow rate on the order of hundreds of nL $min^{-1}$, is an ideal spray source for the applications described here because the droplets that exit the spray chamber are in the same size range as the particles of interest, from roughly 100 nm – 500 nm, and the droplet distribution

is monodisperse, with a coefficient of variation (one standard deviation of the size distribution divided by the mean size) on the order of 15%. These are important characteristics due to droplet induced aggregation.[24] This is an artifact created by spray procedures. If more than one particle is contained within a single droplet, after evaporation of the liquid the resulting aerosolized particle will be a dimer, though the two particles were initially monomers in solution. Droplet aggregation is related to the particle size, droplet size, and particle concentration. Generally, dilute samples of large particles that are of similar size to the droplet show minimal droplet aggregation. The nES can produce negligible droplet aggregation for nanoparticles while nebulizers tend to cause significant droplet aggregation. Another droplet induced effect is the increase in size of aerosolized particles compared to their size in liquid if nonvolatile salts are in solution. The droplet that contains the particle of interest also contains nonvolatile material that dries onto the surface of the particle as the droplet evaporates. Figure 1.3 illustrates the possible consequences of droplet evaporation. To minimize nonvolatile material effects, we tend to disperse nanoparticles in ammonium acetate buffer, because it is volatile and evaporates with the droplet (it does not increase the size of the aerosolized particle). However, the contribution of nonvolatile salts can be corrected for if the droplet distribution is known, and the correction works best for a monodisperse distribution of droplets. Overall, nES is an ideal spray source for mobility measurements of nanomaterials because it limits droplet induced aggregation and offers a simple correction for increased size due to salt coating.

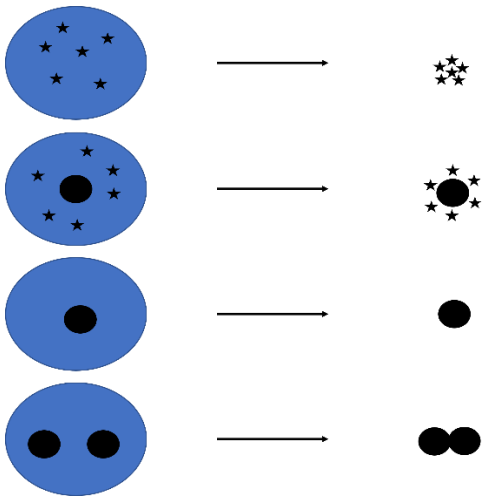

**Figure 1.3:** Droplets on the left dry to form aerosols on the right. Stars indicate nonvolatile molecules and small black circles indicate nanoparticles. From the top, a droplet containing only nonvolatile molecules produces a salt particle. In line two, a droplet containing nonvolatile molecules and a nanoparticle produces a nanoparticle coated with salt. Next, a droplet containing only a nanoparticle produces a clean nanoparticle (the aerosol size is representative of the size in solution). Finally, a droplet containing two nanoparticles produces a droplet induced dimer.

*1.4.2 Nebulizer*

Nebulizers spray by mechanical means, forcing a flow of liquid against a pressurized flow of gas that causes a jet and breaks the liquid apart into small droplets. Nebulizers tend to produce larger droplets than electrospray, on the order of several micrometers, and produce more polydisperse distributions of droplets. Often impactors are used to remove the largest droplets. Small particles can follow streamlines of air. They have minimal mass and momentum, so when carrier air flow changes direction the particles are also able to change direction. Impaction involves a controlled flow to a surface that blocks the direction of air flow. Small particles are able to redirect, but large particles tend to collide with the surface due to inertia and are removed from the gas phase.[25]

There are several configurations used for nebulization. Concentric nebulizers are commonly used with inductively coupled plasma mass spectrometry or optical emission

spectroscopy. They involve two parallel flows separated by a glass wall, an inner liquid flow that carries the particles of interest, and an outer gas flow that breaks the liquid flow apart at the tip, where the two flows meet. Alternative configurations, such as the atomizer, involve compressed air passing through a narrow orifice that results in a jet zone. When liquid enters the jet, it is broken apart into small droplets. The fast flow of the gas produces a low-pressure zone that pulls liquid through a capillary into the jet. Due to the larger droplets produced by nebulization, drying is often necessary before mobility measurements can be made. This is done by passing the aerosol through a heated tube furnace or a diffusion drying tube filled with desiccant. The primary advantage of nebulization is that no electrolyte is required. This means that nanoparticles can be sprayed in any buffer or pure water, though the salt coating mentioned with regards to the electrospray also occurs during nebulization. Nebulizers tend to have higher liquid flow rates than electrospray and therefore require more sample. At these higher flow rates, more pump options are available. The pneumatic pumps used for the inductively coupled plasma techniques are very consistent and result in more stable flow rates than the nES. Nebulizers are a useful spray technique, but the droplet distribution produced is less conducive to mobility measurements of nanomaterials than the nES.

### *1.5 Neutralizer*

The DMA separates particles based on the balance of their electrostatic and drag force. As only charged particles experience the electrostatic force, only charged particles are selected for by the DMA. As a result, the charge distribution of the aerosol has a direct impact on the measurement by DMAS. It is important that the charge distribution is known so that a representative size distribution can be derived from the mobility distribution. A radioactive source charges the surrounding gas, creating a bipolar charge environment consisting of both positive and negative

charges that collide with the aerosol particles and stick.[26] An equilibrium, diffusion-based charge distribution results as the aerosol flows through the charge neutralizer. The radioactive source is either an alpha emitter, Po-210, or a beta emitter, Kr-85. It neutralizes the particles after the droplet evaporate. For the nES, this charge chamber is placed immediately after the spray chamber to minimize the loss of the initially highly charged particles. Given a minimum level of radioactivity and residence time, a known charge distribution will be applied to the particles. This charge distribution is dependent on the particle size and was determined by Wiedensohler.[27] For diffusion charging, the fraction of charged particles increases with the diameter of the particle. Particles around 10 nm tend to be mostly uncharged, with about 9% of particles carrying a +1 or -1 charge. Larger particles carry more charge. Particles around 100 nm are more likely to be charged than uncharged, with 48% of particles carrying a +1 or -1 charge and 9% carrying a +2 or -2 charge. The term neutralizer refers to the fact that the overall charge of the environment is roughly neutral. However, there is a slightly higher proportion of negatively charged particles than positively charged due to the difference in diffusivity of negatively and positively charged gas ions.[28] A newer charge source is the soft x-ray source that emits light at sufficient energy to create a bipolar charge environment via photoionization. The soft x-ray source does not require renewable radioactive material and has a more nearly equal distribution of positive and negative charges. Regardless of the specific source used, the purpose of the neutralizer is to apply a known charge distribution to the aerosol.

### *1.6 Detectors*

A variety of detectors can be used to detect the aerosol output from the DMA. The DMA itself merely acts as a bandpass filter, emitting a monodisperse aerosol. Any detector that is

compatible with aerosols can be used. The most used is the condensation particle counter (CPC), an optical detector that grows particles to a size that is easier to count. More recent work has focused on the use of the inductively coupled plasma mass spectrometer (ICP-MS), a mass measurement that is very sensitive for high atomic mass elements such as transition metals. These are the two detectors used in this dissertation, though a few alternative detectors will be mentioned briefly for context.

### *1.6.1 Condensation Particle Counter*

The CPC consists of three key components: a preparation chamber, a condensation chamber, and a laser for particle counting. Aerosolized particles enter a preparation chamber where the surrounding air becomes saturated with a given working fluid. The high vapor concentration of the working fluid prepares the particle for growth. Next the particles enter a condensation chamber that results in heterogeneous nucleation on the particle of interest. Given sufficient time for growth, the steady state size from surface growth is independent of the initial particle size. This means that all particles that enter the condensation chamber will exit at roughly the same diameter, on the order of several micrometers. The size and uniformity allow for counting individual particles based on the light scattered by the particles passing through the laser beam.[29] This process is shown in Figure 1.4. Individual particles are counted by pulses of scattered light up to a concentration on the order of 100 000 particles per $cm^3$ gas, depending on the instrument model, at which point a continuous measurement is used to extrapolate a concentration. Butanol and water are the two most common fluids used for particle growth. For butanol, the condensation chamber is cooled because the thermal diffusivity of air is greater than the mass diffusivity of butanol. This means that the sample flow will be cooled before the butanol can diffuse to the walls, so butanol

condenses on the nanoparticles rather than the walls. For water, the opposite is true, and the condensation chamber is heated and wetted. This keeps the water vapor in the sample flow instead of condensing on the cooled walls.[30] A limitation of the CPC is that the supersaturation required for heterogeneous nucleation (Gibbs-Thomson effect) increases significantly as the particle size decreases. This means that each instrument model has a smallest detectable size, which is characterized by the Kelvin diameter.

$$\frac{P}{P_s} = exp\frac{4\Gamma M}{\rho RTD_{p,K}} \tag{1.9}$$

Where $P$ is the vapor pressure, $P_s$ is the saturation vapor pressure, $\Gamma$ is the surface tension of the working fluid, $M$ is the molecular weight of the working fluid, $\rho$ is the density of the working fluid, $R$ is the gas constant, $T$ is the temperature (K), and $D_{p,K}$ is the Kelvin diameter. This size limit is determined by the supersaturation of the working fluid, which is in turn limited by homogenous nucleation. When the supersaturation is too high, the butanol or water vapor will condense into droplets of butanol or water, without a nanoparticle nucleus. This results in erroneous detection of particles. The lower size limit of detection for CPCs is defined by $D_{50}$, the diameter at which half of the total particles will be detected. This size tends to be around 2.5 nm for the newest instrument models. The pressure drop across a well-defined orifice is used to accurately determine the gas flow rate and relate the raw data, particles counted during a period of time, to a number concentration, particles per $cm^3$ gas. A second method allows the direct measurement of the charged particles by using an electrometer.[31] The electrometer is a similar detector that was used more prior to the development of the CPC. The electrometer measures the current produced by charged aerosols from which the number concentration of the charged particles can be determined for a known charge distribution. Electrometers can detect a higher

maximum aerosol concentration than the CPC, but the minimum concentration is also higher. Electrometers are easier to calibrated directly and are then often used to calibrate CPCs. Overall, the CPC is a common aerosol detector that grows particles and counts them individually by light scattering.

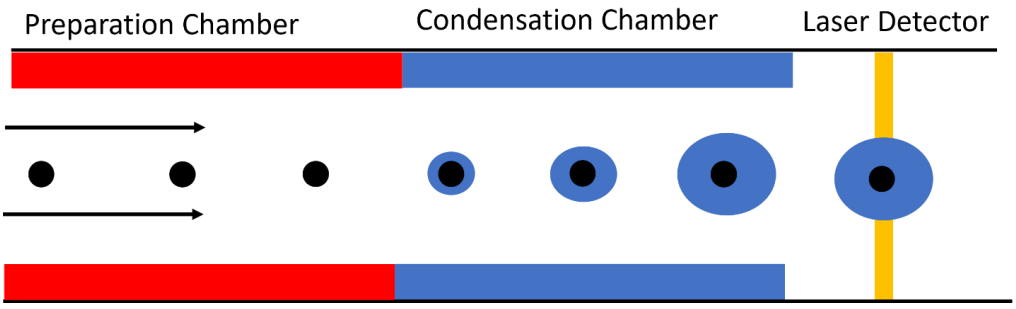


**Figure 1.4:** A schematic of a butanol CPC. An aerosol enters a heated preparation chamber saturated with butanol vapor, travels to a cooled condensation chamber that induces butanol condensation on the particles, and finally individual particles are counted optically.

*1.6.2 Inductively Coupled Plasma Mass Spectrometer*

The Inductively Coupled Plasma Mass Spectrometer is being used more frequently as a detector for monodisperse aerosols exiting the DMA.[32,33] The aerosol enters a high temperature plasma and is broken apart into individual atoms and charged. The ions are then separated by mass-to-charge ratio in an octopole and are detected by an electron multiplier. As the instrument detects atoms, the measurement is proportional to the mass concentration of the specific mass-to-charge ratio sampled, and calibration curves for generic ICP-MS measurements relate instrument response to solution concentration of the element of interest. The plasma is generated by passing argon through a strong electromagnetic field generated by a radio frequency coil with an oscillating current on the order of 20 MHz as shown in Figure 1.5.[34] A spark causes an initial loss of electrons from some argon atoms. These free electrons propagate the plasma by colliding with other argon atoms and ionizing them. The region of the plasma that the aerosol enters is generally on the order

of 6 000 K and is therefore able to evaporate the aerosolized droplets and break apart nanoparticles into component elements. The ions then flow through two small orifices, the sampling and skimmer cones, needed to retain the high vacuum of subsequent components of the instrument. The ions then pass through the ion optics, a series of metal discs with applied voltages that shape and direct the ion beam. The ion optics physically blocks particulates, photons, and neutral species, while atomic ions are directed around obstacles to the mass analyzer.[35] Within the mass analyzer, most commonly a quadrupole or octopole, the ions are separated based on their mass-to-charge ratio. A series of metal rods (four or eight) with a direct current applied to some rods and a radio frequency applied to others selects for ions with atomic resolution. Alternative mass analyzers include time of flight and magnetic sector analyzers, but these are not commonly used for ICP-MS and will not be discussed further. The ions of the selected mass-to-charge ratio then reach the detector, typically an electron multiplier. When the ions contact the surface of the detector, electrons are emitted within the detector. These primary electrons then impact new areas of the detector and result in the emission of secondary electrons. As a result, the arrival of an ion results in the generation of millions of electrons that are detected as a pulse of current.

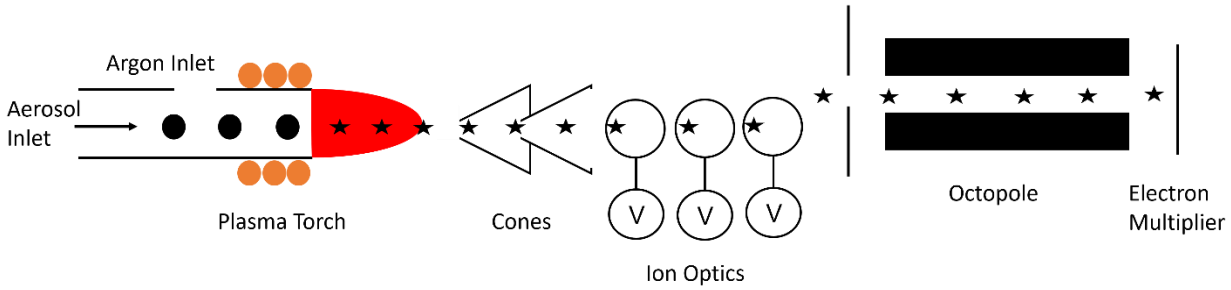


**Figure 1.5:** A model ICP-MS, where black circle aerosol particles are converted into atomic ions indicated by stars. The ions pass through narrow cones to the ion optics that shape the ion beam and direct it to the octopole while removing interferences. The octopole selects for a specific mass-to-charge ratio and those ions are detected by the electron multiplier.

With the DMA in mind, one limitation of the ICP-MS is that it requires argon for the plasma generation. The DMA is mostly commonly run with air, due to availability, but it can use any nonreactive gas. However, both the DMA and the nES are limited by the electrical breakdown of the gas. The nES is not able to use as wide of a voltage range as the DMA and generally requires a stronger electric field, on the order of $10^6$ V $m^{-1}$. Therefore, the nES is used almost exclusively with air and possibly a stabilizing gas such as carbon dioxide. As a result, some of the gas exiting the DMA is air, and the argon content of the gas may not be high enough for the plasma to ignite. Measurements using the nES, DMA, and ICP-MS use a gas exchange device (GED) to increase the concentration of argon in the gas to the ICP-MS. The GED, shown in Figure 1.6, consists of a porous glass membrane contained within a glass cylinder. The aerosol flow size-selected by the DMA travels within the membrane while pure argon is pumped into the outside space. The argon flows in the opposite direction of the aerosol to promote diffusional exchange of argon and air. For conditions commonly used in the experiments described here (1 L $min^{-1}$ aerosol flow rate, 3 L $min^{-1}$ argon GED flow rate), the argon concentration increases 57% within the aerosol flow due to the GED.[36]

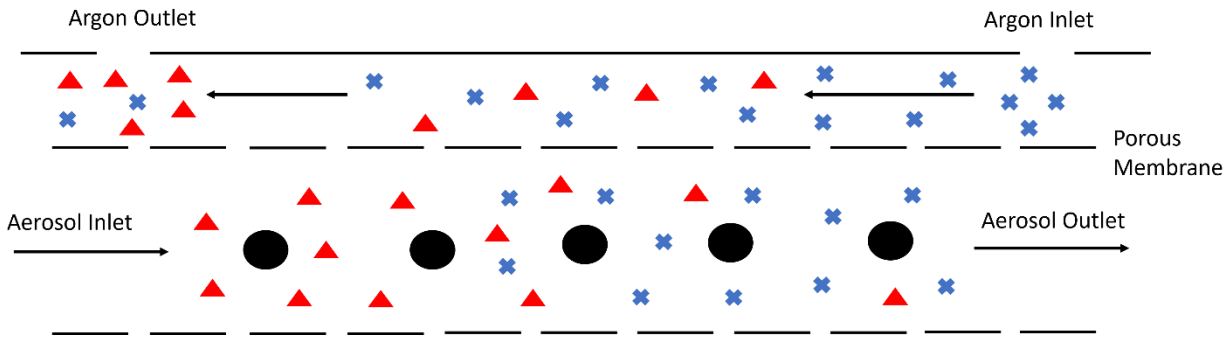


**Figure 1.6:** A model of the GED, where black circles are aerosolized nanoparticles, red triangles are air molecules, and blue crosses are argon molecules. The aerosol enters the GED dispersed primarily in air and exits dispersed primarily in argon. The gas molecules can diffuse across the porous membrane while the nanoparticles remain in the central flow.

### *1.7 Differential Mobility Analysis*

A full complement of instruments needed for a measurement of size, consisting of a spray source, DMA, and detector is called DMAS. The two configurations most used here are nES-DMA-CPC and nES-DMA-GED-ICP-MS. The first measures the particle number distribution while the second measures the particle mass distribution of selected mass-to-charge ratios. For nES-DMA-CPC measurements, the raw data are voltage applied to the DMA and number concentration ($N_{CPC}$) measured by the CPC. The voltage corresponds to a particular mobility ($Z_p$), so the raw data are mobility distributions. The measured number concentration is equal to an integral of the product of the transfer function of the DMA ($\Omega(Z_p, V)$) and the mobility distribution of the aerosol prior to separation by the DMA ($F(Z_p) = dN/dZp$).

$$N_{CPC}(V) = \int \Omega\,(Z_p, V) F(Z_p) dZ_p \tag{1.10}$$

However, the size distribution ($G\left(D_p(Z_p)\right) = dN/dDp$) is the actual quantity of interest. Using the relationship between the mobility distribution and the diameter distribution one obtains the corresponding expression in terms of the number distribution. It contains the transfer function of the DMA, the charging probability of the particle ($p(D_p(Z_p))$) and a term to convert the integral from mobility space to diameter space.

$$N_{CPC}(V) = \int \Omega\,(Z_p, V) G\left(D_p(Z_p)\right) p(D_p(Z_p)) \left|dD_p/dZ_p\right| dZ_p \tag{1.11}$$

This conversion term can be derived from the relationship between mobility and diameter selected by the DMA.

$$\left|dD_p/dZ_p\right| dZ_p = \frac{1}{x}\left|\frac{C_c'(D_p)}{C_c(D_p)} - \frac{1}{D_p}\right|^{-1} dx \tag{1.12}$$

The derivation is simplified using a unitless mobility, $x$.

$$x = \frac{2\pi LVZ_p}{q_{sh}\ln(r_2/r_1)} \tag{1.13}$$

$L$ is the length of the DMA from entrance slit to exit slit, $V$ is the voltage of the inner electrode, $q_{sh}$ is the sheath flow rate, $r_2$ is the outer radius, and $r_1$ is the inner radius. The transfer function is triangular and ranges from points (1-$\delta$, 0) to (0, 1) to (1+$\delta$, 0) in the $x$ coordinate system, where $\delta$ is the ratio of the aerosol flow rate to the sheath flow rate.

$$\delta = \frac{q_a}{q_{sh}} \tag{1.14}$$

The charging probability has been solved using tandem DMA measurements, where a first DMA is used to produce a monodisperse aerosol, and a second separates the different charge states by mobility. An empirical fit was determined for +1 charged particles from 1 nm to 1 000 nm in diameter.

$$p\left(D_p\left(Z_p\right)\right) = 10^{\left[\sum_{i=0}^{i=5}(a_i)\left(log\frac{D_p}{nm}\right)^i\right]} \tag{1.15}$$

$a_0$= -2.3484, $a_1$= 0.6044, $a_2$= 0.4800, $a_3$= 0.0013, $a_4$= -0.1544, and $a_5$= 0.0320.[27]

One way to solve for the diameter number distribution is to assume that the size distribution changes slowly with diameter compared to the transfer function. With this assumption, most of the terms in Equation 1.11 can be removed from the integral as constants, leaving the integral of the transfer function from $x = 1 - \delta$ to $x = 1 + \delta$. As described above, the transfer function is a triangle with base $2\delta$ and height 1, so the integral of the transfer function is equal to $\delta$. The diameter distribution of the aerosol before the DMA can then be calculated.

$$G(D_p) = \left[N_{CPC}(V)\left|\frac{C_c'(D_p)}{C_c(D_p)} - \frac{1}{D_p}\right|\right] / \left[(\delta)\left(p(D_p)\right)\right] \quad (1.16)$$

These equations are traditionally applied to number concentration measurements by the CPC, though the same logic applies to measurements with alternative detectors. For example, mass concentration measurements by the ICP-MS, $M_{ICP-MS}(V)$, are analogous to $N_{CPC}(V)$, and can be used to solve for the mass distribution before the DMA, $H\left(D_p(Z_p)\right)$, which is analogous to $G\left(D_p(Z_p)\right)$.

### *1.8 Coupled Instrumentation*

Each instrument described here has standalone strengths that could be used independently. However, the focus of this work is on the advantages of the combined instruments. For example, the DMA can be used to select a monodisperse aerosol. However, without a detector this is of limited value. The CPC counts particles and determines a number concentration. This can be used independently as a warning system to detect particle generation in industrial settings. With the combined instruments, DMA-CPC, number concentration measurements can be made at narrow intervals of the size distribution. For the example given above, detection of particle generation in industrial settings, the coupled technique can determine the size range in which most of the particles occur. The size range and the mass concentration are important in understanding the health risk of the aerosol. The same thought process applies to a variety of other examples. As nanoparticle products become more complex, the related problems and questions that arise often require more complicated instrumentation to acquire new information. An alternative hyphenation of the DMA is to select for particles that are then deposited on to microscopy grids. This can allow

for simplified microscopic analysis for complex samples with many variables, as fractions can be collected with a particular size selected for different grids. The DMA has also been combined with the aerosol particle mass analyzer and ICP-MS to determine mass distributions, and elemental analysis by ICP-MS. The DMA can theoretically be coupled with any aerosol detector, such as spectroscopic techniques that could be used to study changes in particle surface coating with size. The combination of multiple techniques often gives more information than the sum of the individual components and can be used to make novel measurements.

### *1.9 Instrument Configurations*

Several instrument configurations will be used in this dissertation. The most used configuration is presented in Figure 1.7, though different DMA flow rates were used in different chapters. In chapter 2, the sheath (carrier) and excess (waste) flows are 10 L $min^{-1}$, and the monodisperse and polydisperse flows are 1 L $min^{-1}$. In chapters 4 and 5, the sheath and excess flows are 20 L $min^{-1}$, and the monodisperse and polydisperse flows are 1 L $min^{-1}$. The same flow ratio (20:1) was used for the scan voltage measurements in chapter 4, but the recirculation flow system was incapable of a sheath and excess flow of 20 L $min^{-1}$. Figure 1.8 shows the configuration used in chapter 3, and Figure 1.9 shows the alternative configuration used in chapter 4 for the scan mode measurements.

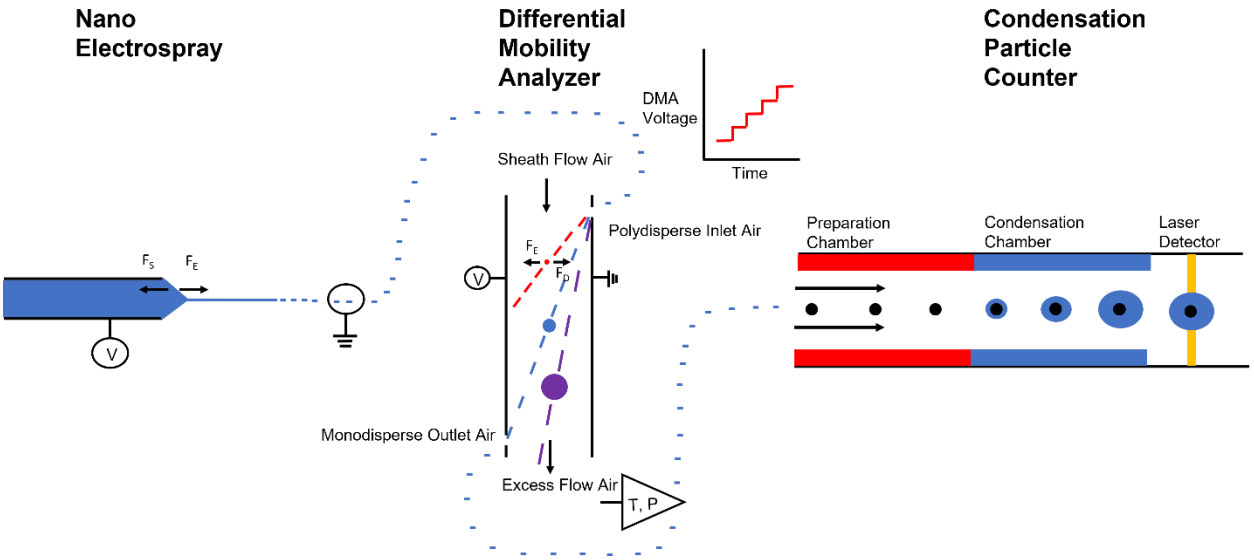


**Figure 1.7:** The DMAS (step voltage) instrument configuration used in chapters 2, 4, and 5. The nES converts a colloidal solution to an aerosol. The dried aerosol is size separated by different voltages applied to the DMA. In chapter 2, the nano DMA is used (4.978 cm length), while in chapters 4 and 5 the long DMA was used (44.369 cm length). The temperature and pressure of the excess flow was measured. The size-selected particles travel to the condensation particle counter and grow to several microns to be counted optically.

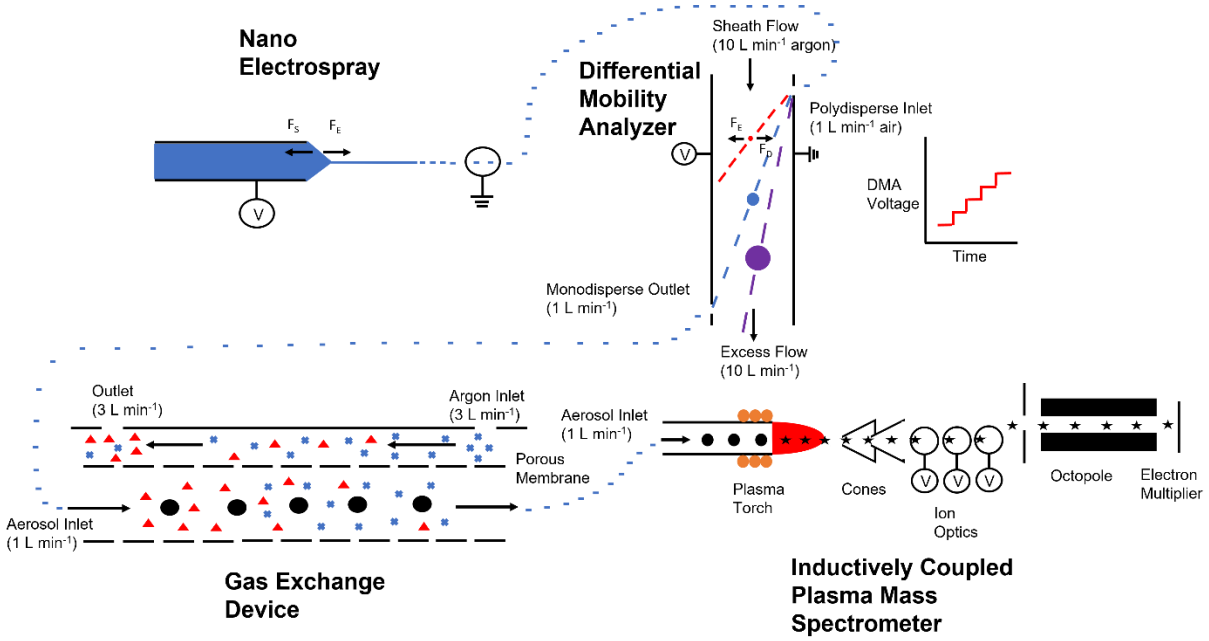


**Figure 1.8:** The DMAS instrument configuration used in chapter 3. The nES converts a colloidal solution to an aerosol. The dried aerosol is size separated by different voltages applied to the DMA. The gas is a mixture of air from the nES and argon from the DMA sheath flow. The aerosol travels through the GED where the argon content of the gas increases due to diffusion across a porous membrane. The argon-enriched aerosol travels to the ICP-MS, where the plasma breaks the nanoparticles into atomic ions. A cloud of produced ions is selected for by the cones and ion optics. The octopole separates the ions by mass-to-charge ratio, and the selected ions are detected by the electron multiplier.

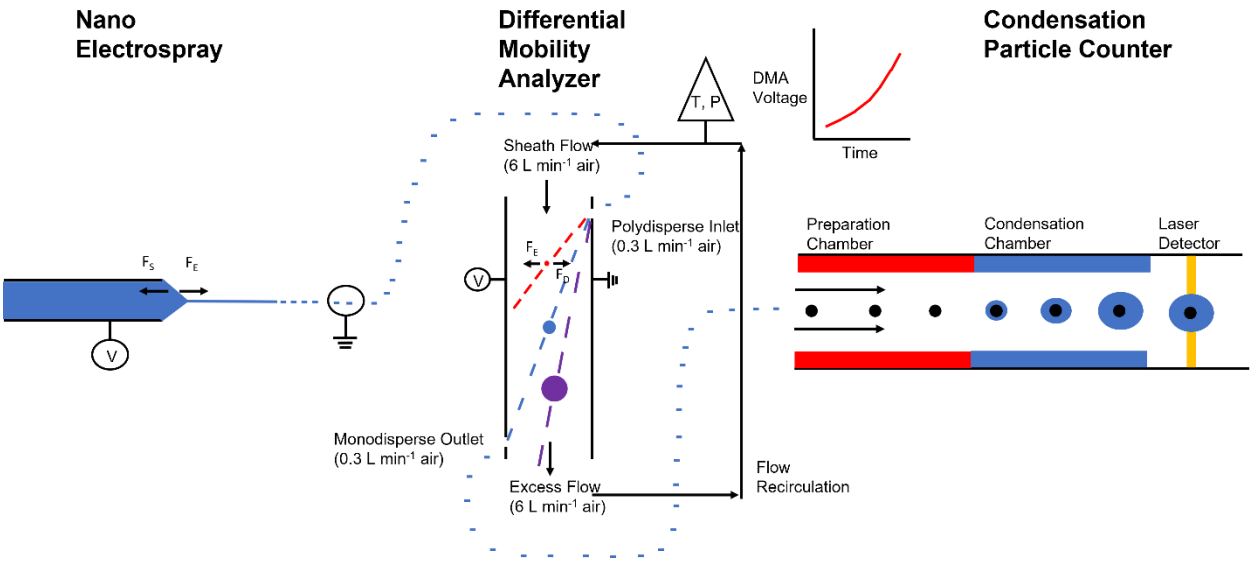


**Figure 1.9:** The DMAS (scan voltage) instrument configuration used in chapter 4. The nES converts a colloidal solution to an aerosol. The dried aerosol is size separated by continuously changing voltages applied to the DMA. The long DMA was used (44.369 cm length), and the temperature and pressure were measured in the flow recirculation, where the excess flow is recycled to be used again as the sheath flow. The size-selected particles travel to the condensation particle counter and grow to several microns to be counted optically.

## *1.10 Topics*

This dissertation focuses on new characterization methods of nanoparticles by DMAS. Chapter 2 demonstrates protein aggregation measurements by DMAS and AF4. The comparison with an *in-situ* method allows for better understanding of the effects of electrospray and aerosolization on aggregation. As discussed before, droplet induced aggregation from the nES needs to be minimized so the measured rates reflect aggregation in solution. Similar rates and activation energies were determined by the two techniques, suggesting alternate techniques can be used by the pharmaceutical industry beyond the traditional SEC.

Chapter 3 covers calibrated mass distribution measurements by nES-DMA-GED-ICP-MS. The calibration was made by summing the total mass across the distribution and comparing ionic standards of known mass concentrations with gold nanoparticles with unknown mass

concentrations. The method was validated by comparing with other total mass measurements, such as gravimetric analysis and acid digestions measurements by ICP-MS. Overall, good agreement was determined between ionic standards and monodisperse gold nanoparticles, but measurements of polydisperse metal oxide particles resulted in significant overestimation of mass concentration. A multiple charge correction was applied that reduced overcounting for the metal oxide particles.

Chapter 4 focuses on the accurate measurements of two gold nanoparticle samples with the DMA operating in step voltage mode. In recent years, the scan voltage mode operation of the DMA has become much more widely used than the step mode because of the much shorter time for measuring a size distribution. In step voltage mode the DMA stays at one voltage until the aerosol travels from the DMA to the detector, so it is simple to pair CPC number concentration measurements with DMA voltages. In scan voltage mode the DMA rapidly scans through voltages so the relationship between CPC number concentration measurements and DMA voltages is less clear. It is of interest to know the relative performance of the DMA in the scanning mode compared with the more accurate stepping mode. A series of measurements were carried out in the scan mode using the same 60 nm calibration particles to calibrate the measurements. Good agreement between step and scan mode was determined for two potential nanoparticle size standards when using the traceable calibration standard.

Chapter 5 compares the results for size measurements of a single standard by four different instruments. Two different traceability pathways including DMAS measurements traceable via the 100 nm SRM 1963a were used to relate the measured diameter to the meter, and there were significant differences between some of the measurements. Overall, all techniques agreed within 3%, which is impressive due to the different measurands probed by each instrument, and is likely sufficient for general use, though some of the error bars did not overlap, suggesting additional

uncertainty components may exist. This has the possibility to create issues for accurate size measurements in the future, as two of the pathways are being used to independently certify new standards.

Finally, chapter 6 includes conclusions and potential future work.

# Chapter 2: Quantifying Protein Aggregation Kinetics using Electrospray Differential Mobility Analysis

## *2.1 Introduction*

Aggregation is an important concern in the protein therapeutics industry. Aggregation can reduce the dose of active drug, resulting in variable efficacy. More importantly, aggregates can trigger a severe immune response including anaphylaxis and in some cases death. As a result, protein products must be thoroughly screened for aggregates throughout the production process. The most basic regulatory requirement for injections is the United States Pharmacopeia Reference Standard 788, which sets particle-per-container specifications as detected by light obscuration. This standard is used by quality control personnel to screen products prior to distribution. Ideally, aggregate formation is prevented much earlier in the product cycle. Aggregation kinetics are measured extensively during formulation and in the initial stages of production, and the buffer, pH and excipients are optimized to produce a stable formulation. Different stress conditions are applied, including shaking, stirring, heating and changing pH to mimic situations that can be encountered during the manufacturing process. The challenge, however, is to measure aggregation verifiably at all potential growth stages, from both a process control standpoint as well as a view to the science of protein aggregation. Many measurement approaches have been adopted to evaluate aggregates and aggregation rates, including light scattering, sodium dodecyl sulfate polyacrylamide gel electrophoresis, analytical ultracentrifugation, fluorescence, optical absorbance, calorimetry and field-flow fractionation[37]. The most commonly used technique in industry currently is size exclusion chromatography[38], although no single technique has been established that has satisfied all characterization needs. Absolute aggregation kinetics data are fraught with a range of interference effects including adsorption[39], membrane interaction[40],

aggregate disruption[41], dilution effects[42], and convolution[43]. Thus, there is a considerable need for assessing methods in terms of absolute and relative accuracy and precision.

In the present work, a lesser known but rapid, high-resolution aerosol-based technique, differential mobility analysis (DMAS, see Figure 2.1),[*] is applied to quantify the thermally induced aggregation kinetics of two selected proteins in an extensive and systematic study. This work builds on two previous studies conducted at the National Institute of Standards and Technology (NIST). Pease et al. showed that DMAS can resolve and accurately size IgG aggregate oligomers prepared by pH-induced unfolding and chemical-induced crosslinking.[44] Subsequently, Guha et al. compared DMAS with the "gold standard," SEC, for thermal aggregation of IgG.[45] The latter study examined oligomer size and concentration, while also determining and comparing aggregation rates between the two techniques (where aggregation was carried out in an ammonium acetate buffer to support the electrospray process). Ammonium acetate is an ideal and commonly used electrolyte for DMAS due to its volatility; nonvolatile salts will interfere with DMAS and alter the size of classified aggregates. However, ammonium acetate is not relevant for the measurement of protein aggregation, and can itself induce unfolding leading to aggregation.[46] In building on these earlier studies, this new method determines protein aggregation rates using the monomer loss approach combined with DMAS. In the current work, aggregation was conducted in common protein formulation buffers followed by post-reaction dilution into ammonium acetate. The aggregation rates are therefore determined by the buffer used during thermal treatment. Using this method, protein aggregation kinetics are quantified under a range of conditions and demonstrate the full capacity for application of DMAS as an alternative technique relevant to

[*] DMA is also referred to in the literature as macro-ion mobility spectrometer (MacroIMS), scanning mobility particle sizer (SMPS) and gas-phase electrophoretic mobility molecular analyzer (GEMMA).

protein drug development and manufacturing. To cross-validate this method and determine whether the measured kinetics are reliable, a direct orthogonal comparison is provided between DMAS and asymmetrical flow field-flow fractionation (AF4), a liquid-based method that separates particles according to their diffusivity (hydrodynamic size).[47] AF4 was selected in this case over SEC so that protein samples could be analyzed in the formulation buffers without any change in buffer composition or ionic strength. A more detailed description of AF4 is provided in the supplemental information.

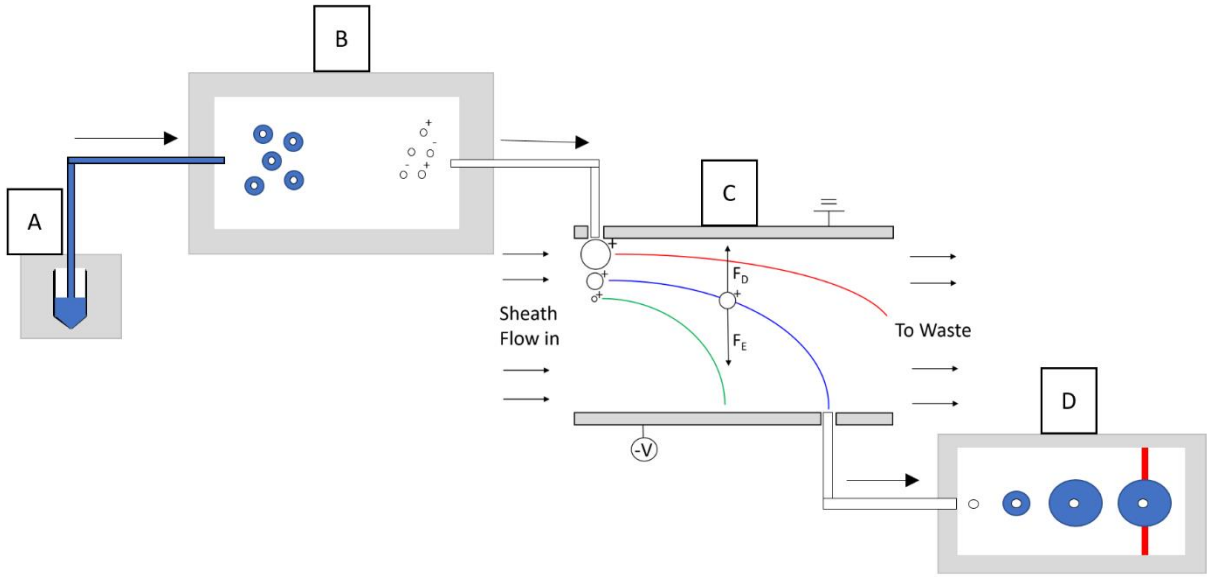


**Figure 2.1:** DMAS method for the separation of nano scale particles. The protein solution is placed in a pressurized chamber and passed through a small capillary (A). The solution is electrosprayed into a neutralization chamber that yields particles with a -1, 0 or +1 charge (B). The +1 charged aerosol is separated by size in the differential mobility analyzer (C). The particles are counted optically by a condensation particle counter (D).

To facilitate this investigation, two well characterized and widely available model proteins were selected, namely bovine serum albumin (BSA) and α-chymotrypsinogen A (α-chymo). Both proteins are stable in solution at room temperature for at least one day and have been previously

studied in kinetic experiments.[37, 48] BSA is a 66.3 kDa globular protein with an isoelectric point (pI) of 4.8 and a hydrodynamic diameter of 7.0 nm.[49] α-chymo is a 25.7 kDa globular protein with a pI of 9.2 and a hydrodynamic diameter of 4.4 nm.[50] Commercial α-chymo contains a small amount of chymotrypsin that can cleave peptide bonds above pH 5, so experiments were conducted at pH 3.5.[51] Neither protein is used as a therapeutic, but human serum albumin is used as a carrier for paclitaxel in Abraxane, an approved treatment for metastatic cancer. On the other hand, α-chymo is the inactive precursor to chymotrypsin, a proteolytic enzyme produced in the pancreas.

### *2.2 Materials and Methods*

BSA (>96%), α-chymo (essentially salt-free, lyophilized powder), sodium phosphate dibasic (>99%), citric acid (99.5%), ammonium acetate (>99.99%) and sodium citrate dihydrate (>99.9%) were purchased from Sigma Aldrich (St. Louis, MO, USA).[#] Sodium phosphate monobasic (99%) was purchased from Alfa Aesar (Haverhill, MA, USA). Solutions were prepared using 18.2 MΩ·cm deionized water (Model 2121AL, Aqua Solutions, Jasper, GA, USA). BSA solutions were prepared by dissolving lyophilized BSA in 0.1 mol $L^{-1}$ phosphate buffer at pH 7.0. α-chymo solutions were prepared by dissolving lyophilized α-chymo in 0.01 mol $L^{-1}$ citrate buffer at pH 3.5 and were filtered before use (0.2 μm, Whatman, Maidstone, UK). Protein concentration was determined spectroscopically at 280 nm using published 1% mass extinction coefficients: 6.58 for BSA[49] and 19.7 for α-chymo.[52] Protein solutions were diluted to the working concentration and volume, then aliquoted to protein lo-bind microcentrifuge tubes (Eppendorf, Hamburg, Germany). For temperature studies, protein samples were heated in a water bath (Model WD05V11B, VWR,

[#] The identification of any commercial product or trade name does not imply endorsement or recommendation by the National Institute of Standards and Technology.

Radnor, PA, USA) and quenched in an ice bath at the designated time point. Each sample was analyzed by both AF4 and DMAS. Aliquots for DMAS were diluted to 0.009 mg $mL^{-1}$ in 0.4 mol $L^{-1}$ ammonium acetate at pH 7.0 or 0.02 mol $L^{-1}$ ammonium acetate at pH 3.5, for BSA and α-chymo, respectively. Ammonium acetate provides sufficient conductivity for the nano electrospray process and leaves no aerosol residue. Aliquots for AF4 were injected into the instrument without modification.

The customized DMAS system used in this study (Figure 1.7), similar to those reported by others,[53] consists of three principal components: the nano electrospray (nES, Model 3480, TSI, Shoreview, MN, USA), differential mobility electrode column (DMA) (Model 3085, TSI), and condensation particle counter (Model 3776, TSI). Protein solutions were placed in the nES pressure chamber set to 26 kPa (3.7 psi) and sprayed through a 40 μm inner diameter fused silica capillary. 40 μm capillaries were used rather than the more common 25 μm capillaries to prevent clogging. Protein was electrosprayed with an air flow rate of 1 L $min^{-1}$ and a $CO_2$ flow rate of 0.2 L $min^{-1}$. The sheath flow was 10 L $min^{-1}$ air. The sheath flow was selected as an optimal compromise between resolution and the limit of detection. The nES voltage was set to 2 kV – 3 kV, with a resulting current of 300 nA – 1100 nA, to produce a Taylor cone. The electric field strength was on the order of $10^6$ V $m^{-1}$. The resulting aerosol was neutralized by a Po-210 α-source (Model P-2042, TSI) to produce a bipolar aerosol with some positively charged, negatively charged, and uncharged particles. The DMA was operated to select positively charged protein particles. The data were collected with a step size of 0.2 nm and a step time of 5 s using a custom LabVIEW (National Instruments, Austin, TX, USA) program to control the high voltage power supply (Model 205B-10R, Spellman, Hauppauge, NY, USA). The BSA monomer yielded a mobility diameter of 6 nm – 7.6 nm with a peak at 6.8 nm. The α-chymo monomer yielded a

mobility diameter of 4.2 nm – 5.6 nm with a peak at 5 nm. These sizes are consistent with previously published work using DMAS[44, 45, 54], though the sizes measured in this work were slightly larger than the uncoated monomers due to residual non-volatile buffer (sodium phosphate or sodium citrate) that coats the protein particles. The unheated protein sample was electrosprayed for one hour before data collection to minimize capillary adsorption effects. A step-ramping voltage was applied to the separation column, selecting for a series of sizes based on certain physical considerations of the instrument outlined in Equation 2.1,[11]

$$\frac{D_p}{C_c(D_p)} = \frac{2neLV}{3\mu q_{sh} \ln (r_2/r_1)} \tag{2.1}$$

$D_p$ is the selected mobility diameter, $C_c$ is the Cunningham slip correction, $n$ is the number of elementary charges on the particle, $e$ is the elementary charge, $L$ is the length of the DMA, $V$ is the voltage of the DMA, $\mu$ is the viscosity of the sheath gas, $q_{sh}$ is the flow rate of the sheath gas, and $r_2$ and $r_1$ are the outer and inner radii of the DMA, respectively. To evaluate the number count, the raw data were corrected for charging efficiency and the DMA column transfer function.[55] When particles are neutralized by the α-emitter, a size-dependent modified Boltzmann charge distribution is applied to the population of particles. Based on the size of the particles, a known percentage will have various charges, primarily -1, 0 and +1. Only particles with a single positive charge were size selected and counted, so the number concentration was multiplied by a correction factor to account for the other charge states of the total population. For example, only 1.9% of 5 nm particles will have a single positive charge, so the measured number concentration was multiplied by 52.6.[27] The separation resolution of the instrument is determined by the ratio of the sheath flow to the sample flow and the size of the particle.[11] The conditions of the present work have a mobility resolution of 12%. For small particles in the free molecular flow regime, the size

resolution is half the mobility resolution,[56] so the window (band pass) of selected particles increases from 0.18 nm at 3 nm to 0.6 nm at 10 nm. The number concentration at each step was divided by the corresponding size window.

Each time point of the kinetic plots consists of nine measurements by DMAS. Chauvenet's criterion was used to analyze outliers of the DMAS measurements.[57] The difference between the suspected outlier and the mean of the nine measurements was divided by the standard deviation and compared to a probability percentage table of a Gaussian distribution. Points with less than a 50% probability of falling within the distribution were rejected. A maximum of one measurement per time point was analyzed for rejection and no more than four total measurements were rejected from a single experiment.

For AF4 analysis, an Eclipse DualTec separation system (Wyatt Technology Inc., Santa Barbara, CA, USA) was used connected to a degasser (Gastorr TG-14, Flom Co., Ltd, Tokyo, Japan), 1260-series isocratic pump (Agilent Technologies, Santa Clara, CA, USA), 1260 ALS series autosampler (Agilent Technologies) and a 1200 series UV-Vis absorbance diode array detector (Agilent Technologies). For the separation, a 145 mm short channel was equipped with a 350 μm spacer and a regenerated cellulose membrane with a 10 kDa cutoff. The UV signal was detected at 280 nm. The elution, injection and cross flow rates were fixed at 0.5 mL $min^{-1}$, 0.2 mL $min^{-1}$ and 3 mL $min^{-1}$ respectively. The injection volume was varied, based on the sample concentration, to inject 50 μg – 60 μg of protein. The focus flow and cross flow rates, during the relaxation and the elution, were optimized as a function of the size distribution of the sample and are summarized in Table 2.1. AF4 data were obtained and analyzed using OpenLab (Agilent Technologies) and Astra 6.1.4.25 software (Wyatt Technology). The monomer peak was manually

defined and integrated with the absorbance signal between 13 min – 16 min elution time for BSA and 10.5 min – 14 min for α-chymo.

**Table 2.1:** AF4 method parameters.

| Flow Type | Duration (min) | Focus Flow (mL $min^{-1}$) | Cross Flow (mL $min^{-1}$) | Elution Flow (mL $min^{-1}$) |
|---|---|---|---|---|
| Elution | 1 | - | - | 0.5 |
| Focus | 2 | 2 | - | - |
| Focus & Injection | 5 | 2 | - | - |
| Elution | 20 | - | 3 | 0.5 |
| Elution | 5 | - | - | 0.5 |

## *2.3 Results and Discussion*

The monomer and the dimer were distinguishable using both techniques, and thus the temporal, relative monomer decline was used as the primary observation of aggregation. This separation is important because it indicates that any larger species will not coelute with the monomer. The decline of the isolated monomer determines the measured rate of aggregation. Figure 2.2a shows the DMAS measured number-based size distribution of BSA as a function of heating time, indicating the BSA monomer had a mobility diameter of 6 nm – 7 nm. Figure 2.2b shows the AF4 measured fractogram of BSA as a function of heating time, indicating the BSA monomer elutes between 13 min – 16 min. To correct for background signal from residual non-volatile buffer (artifact particles formed during aerosolization) a baseline correction was applied for DMAS as shown in the figure. The monomer peak area was then determined by subtracting the total area under the monomer peak by the area of the background for each time point and normalized to the unheated sample. The ratio of the dimer diameter to monomer diameter is indicative of the packing of the monomer during binding (the smaller the ratio, the closer the monomers are packed together).

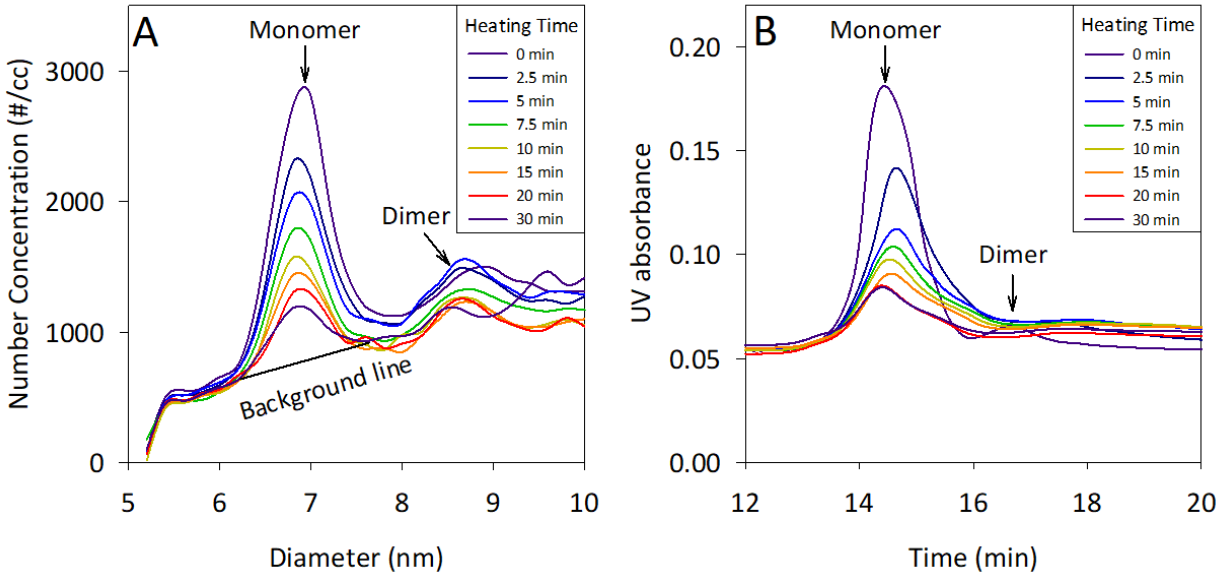


**Figure 2.2:** (a) DMAS determined number-based size distribution for 1 mg $mL^{-1}$ BSA. The monomer was determined to have a mobility diameter of 6 nm – 7.6 nm. The monomer area decreased with increasing heating time at 70 $^{o}$C. The monomer area does not include the area below the background line caused by non-volatile salt. The data points are connected with a smooth line. (b) AF4 fractionation of 1 mg $mL^{-1}$ BSA. The monomer eluted between 13 min – 16 min, and the area under monomer peak decreased with increasing heating time at 70 $^{o}$C. The data points are connected with a smooth line.

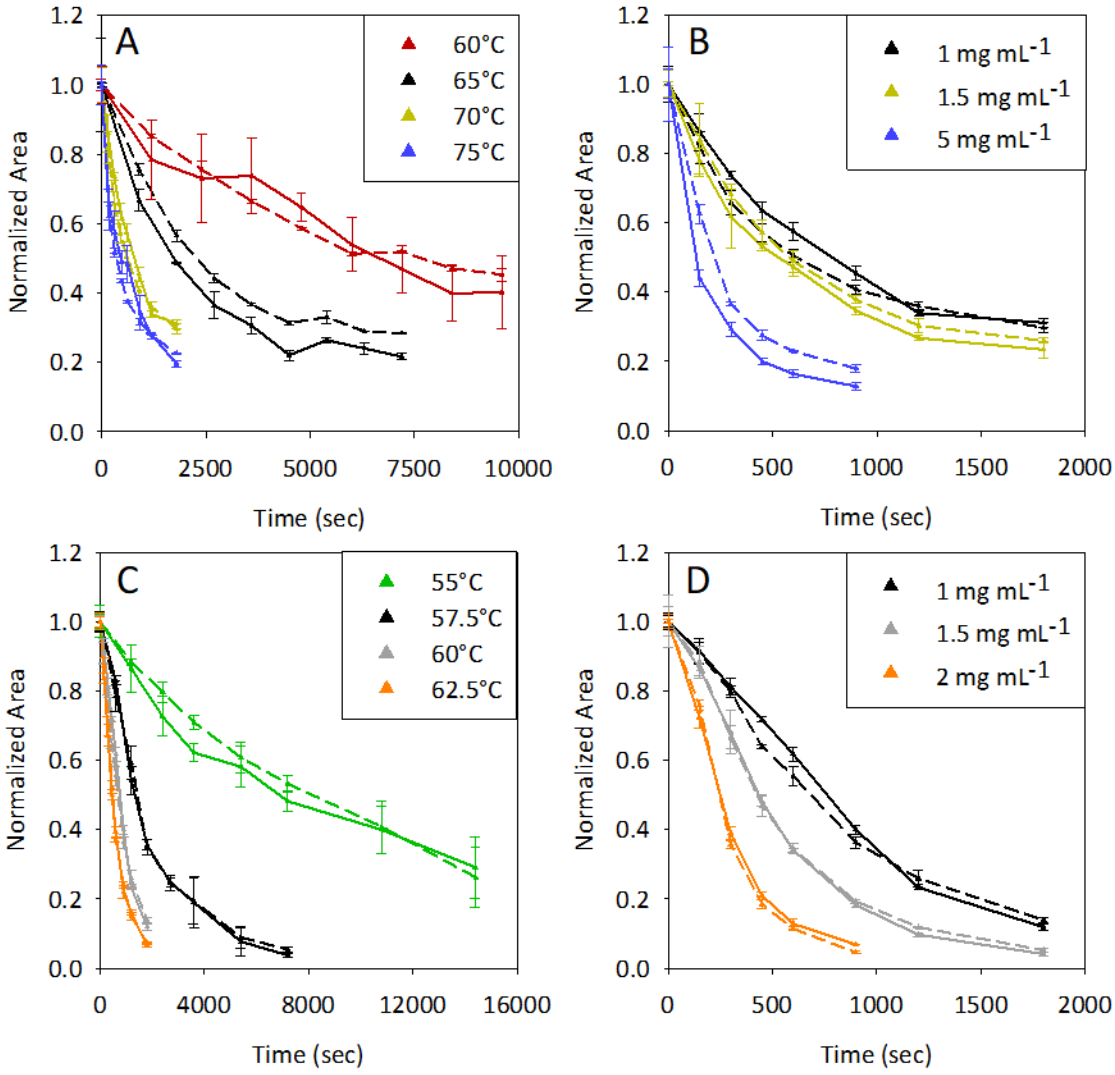


**Figure 2.3:** Normalized protein monomer peak area as a function of time and incubation temperature or incubation concentration measured by DMAS (solid lines) and AF4 (dashed lines). Lines are guides only. (a) 1 mg $mL^{-1}$ BSA incubated at different temperatures. (b) BSA heated at 70 $^{o}$C and incubated at different concentrations. (c) 1 mg $mL^{-1}$ α-chymo incubated at different temperatures. (d) α-chymo heated at 60 $^{o}$C and incubated at different concentrations.

As expected, the rate of aggregation for both proteins increased at higher concentration and temperature. These results are summarized in Figure 2.3 as the mean of three independent samples. For AF4, each sample was analyzed once, while for DMAS each sample was analyzed three times under repeatability conditions. For AF4, the error bars indicate one standard deviation of the three

measurements. For DMAS, the three repeatability measurements were averaged for each sample and the error bars indicate one standard deviation of the three means. The normalized monomer peak area was multiplied by the concentration of the unheated solution and divided by the molar mass to convert to molarity. The goodness-of-fit (using $R^2$) for the linear regression of molarity vs. time, ln (molarity) vs. time, and $(\text{molarity})^{-1}$ vs. time was then used to assess if the aggregation was best represented as zero, first, or second order, respectively.

Results included in the supplemental information show that BSA exhibits second order behavior and α-chymo is most consistent with a first order monomer decay. The aggregation rate for BSA is proportional to the molarity, while the rate for α-chymo is proportional to the molarity squared. This suggests BSA aggregation is limited by monomer-monomer collisions, while α-chymo is limited by monomer thermal unfolding or monomer addition to aggregates. When elevated temperature is used as a stress, aggregation is minimal below the melting temperature of a protein. This indicates that the unfolding of the protein is critical in thermal aggregation. A first order kinetic rate suggests a single protein population is the limiting reactant for aggregation to occur. The aggregation rate for α-chymo varies with initial protein concentration. This suggests that the monomer interacts with another species (e.g., an aggregate) that is an important co-determinant of the rate of aggregation. Also, the unfolding rate of α-chymo is much faster than the aggregation rate.[58] This suggests that α-chymo aggregation is limited by monomer addition rather than unfolding. The driving force of the aggregation is the hydrophobic effect, the collection of hydrophobic components to reduce interaction with water. The cores of proteins tend to be more hydrophobic, so unfolding due to heating increases the hydrophobicity of the protein surface. The hydrophobic effect is based on minimizing the entropy of water, as water molecules form more rigid structures when interacting with hydrophobic materials. For second order kinetics, the protein

molecules are also unfolded, but the collision between two monomers is the limiting step. The ln (molarity) vs. time and (molarity)$^{-1}$ vs. time data were fit with a weighted least squares regression to account for differences in the standard deviation at various times and to determine the most representative slope and uncertainty for a linear fit.[57]

$$y = A + Bx \tag{2.2}$$

$$B = \frac{\Sigma w \Sigma wxy - \Sigma wx \Sigma wy}{\Sigma w \Sigma wx^2 - (\Sigma wx)^2} \tag{2.3}$$

$$\sigma_B = \sqrt{\frac{\Sigma w}{\Sigma w \Sigma wx^2 - (\Sigma wx)^2}} \tag{2.4}$$

Where $A$ is the intercept, $B$ is the slope, $\sigma_B$ is the uncertainty of the slope and $w_i = \sigma_i^{-2}$. The rate constants are compiled in Tables 2.2 and 2.3. Note that the BSA rate constant for 70 $^o$C and 1 mg mL$^{-1}$ is the mean (with one standard deviation) of three experiments performed on three separate days: (120 ± 20) L mol$^{-1}$ s$^{-1}$ and (94 ± 10) L mol$^{-1}$ s$^{-1}$, by DMAS and AF4, respectively. This is significantly higher than (62 ± 2) L mol$^{-1}$ s$^{-1}$ reported previously using AF4.[37] The difference might be attributable to BSA batch variations. Also, the rate constant obtained here for 1 mg mL$^{-1}$ α-chymo heated at 60 $^o$C was (110 ± 10) s$^{-1}$ by DMAS and AF4. This is close to 93 s$^{-1}$ reported previously using size exclusion chromatography.[48] Li et al. reported a half-life of about 14 min, compared with about 11 min determined in the present study using both DMAS and AF4. In this work, the rate constants increased with increasing temperature. The rate constant for α-chymo increased with increasing concentration, while the rate constant for BSA decreased or remained the same with increasing concentration.

**Table 2.2:** Rate constants for the aggregation of BSA measured by DMAS and AF4.

| BSA Condition | | Second Order Rate Constant (L $mol^{-1}$ $s^{-1}$) | |
|---|---|---|---|
| **Concentration (mg $mL^{-1}$)** | **Temperature (ºC)** | **DMAS** | **AF4** |
| 1 | 75 | 130 ± 10 | 130 ± 10 |
| 1 | 70 | 120 ± 20 | 94 ± 10 |
| 1 | 65 | 32 ± 1 | 23 ± 1 |
| 1 | 60 | 9 ± 1 | 9.1 ± 0.1 |
| 5 | 70 | 110 ± 10 | 75 ± 1 |
| 1.5 | 70 | 94 ± 3 | 73 ± 2 |
| 1 | 70 | 120 ± 20 | 94 ± 10 |

**Table 2.3:** Rate constants for the aggregation of α-chymo measured by DMAS and AF4.

| α-chymo Condition | | First Order Rate Constant (1E-5 $s^{-1}$) | |
|---|---|---|---|
| **Concentration (mg $mL^{-1}$)** | **Temperature (ºC)** | **DMAS** | **AF4** |
| 1 | 62.5 | 160 ± 10 | 150 ± 10 |
| 1 | 60 | 110 ± 10 | 110 ± 10 |
| 1 | 57.5 | 52 ± 1 | 45 ± 2 |
| 1 | 55 | 9.7 ± 0.9 | 8.8 ± 0.5 |
| 2 | 60 | 300 ± 10 | 340 ± 10 |
| 1.5 | 60 | 200 ± 10 | 180 ± 10 |
| 1 | 60 | 110 ± 10 | 110 ± 10 |

The activation energy was determined using an Arrhenius plot, with (absolute temperature)$^{-1}$ vs. ln (rate constant) as shown in Figure 2.4. The non-linear plots indicate that the studied proteins are non-Arrhenius in the given temperature range. This indicates a change in the rate determining step at different temperatures. The change in the aggregation rate decreased at higher temperatures. The low temperature region for BSA, from 60 ºC – 70 ºC was linear and was used to calculate the activation energy. The obtained value contains information regarding the thermal unfolding of the protein and the collision required to produce a dimer. The energies reported here for BSA, (240 ± 20) kJ $mol^{-1}$ and (190 ± 10) kJ $mol^{-1}$ by DMAS and AF4 respectively,

are of similar magnitude to those reported in the literature for other proteins: 350 kJ $mol^{-1}$ – 550 kJ $mol^{-1}$.[38, 59]

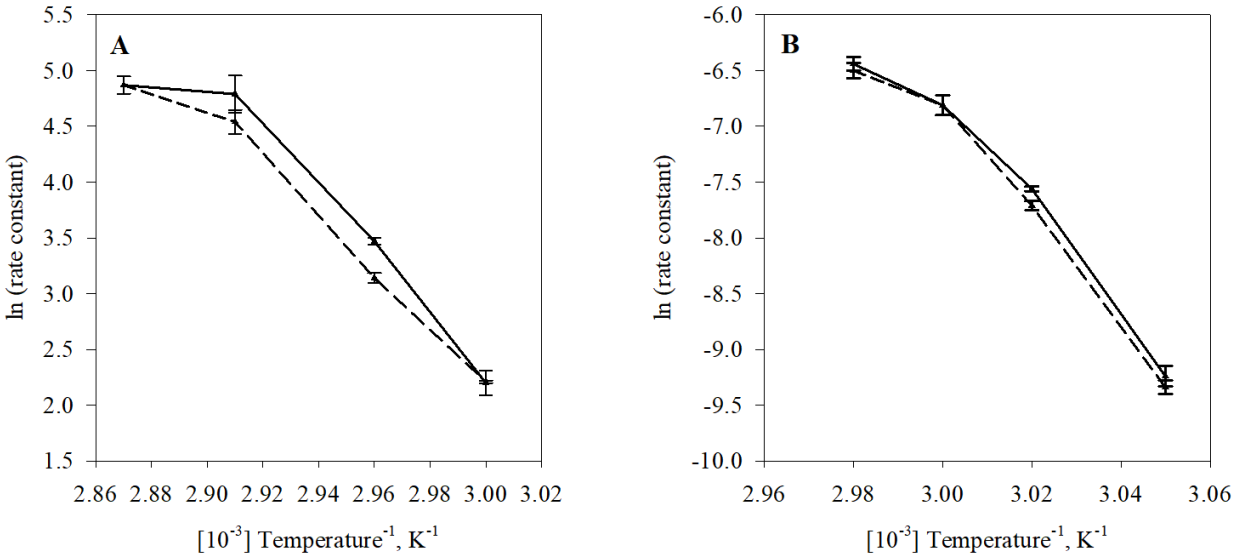


**Figure 2.4:** Arrhenius plots of BSA and α-chymo determined by DMAS (solid lines) and AF4 (dashed lines) rate measurements. Lines are guides only. (a) Arrhenius plot of BSA from 60 °C – 75 °C. The linear region from 0.00291 $K^{-1}$ – 0.003 $K^{-1}$ was used to determine the activation energy. (b) Arrhenius plot of α-chymo from 55 °C – 62.5 °C. The non-linear behavior indicates different rate limiting behavior at different temperatures.

The rates measured by DMAS were generally equal to or slightly faster than those by AF4. Many aspects of the measurement techniques could result in a faster measured rate. For example, DMAS requires a dilution and buffer exchange, uses a fused silica capillary and can cause droplet-induced aggregation during the nES process (Figure 1.3). DMAS requires a volatile buffer and dilute protein solution for the nES, so the protein samples were diluted into ammonium acetate immediately before analysis. Non-volatile buffer components can lead to peak broadening, an elevated baseline and a shift in detected diameter values. An undetermined maximum non-volatile buffer concentration exists (specific to the given protein and conditions) that will prevent protein detection even with dilution in ammonium acetate. The salt particles produced during

aerosolization will completely mask the protein signal. BSA was in a higher concentration of non-volatile buffer (0.1 mol $L^{-1}$ phosphate buffer) than α-chymo, so a higher ionic strength of ammonium acetate was required. The higher ionic strength produces smaller droplets in the nES process.[60] These smaller droplets contain less of the non-volatile salt and therefore mask the protein to a lesser degree. An alternative buffer exchange method, centrifuge filtration, showed no significant difference in the rates measured by DMAS (results not shown). The observed difference between DMAS and AF4 data is similar for both BSA and α-chymo, which suggests that the ionic strength of the dilution buffer does not have a significant effect on the kinetics. Another possible contribution to the differences in the observed rates could be due to proteins adhering to the fused silica capillary.[54] Protein loss to the capillary surface would be convoluted with aggregated protein, as both result in the loss of monomer. This effect was minimized by equilibrating the capillary with the unheated protein sample for one hour prior to data collection. Future work could investigate capillary surface modification to reduce protein adsorption and limit the required equilibration time. Finally, the nES process can cause aggregation if two protein monomers are contained within a single droplet (i.e., coincidence).[24] This artifact would be detected as a protein dimer, because the two monomers merge as the droplet evaporates. This could cause an apparent monomer loss if the nES droplet size varied with time. This effect was minimized by spraying a Taylor cone at the same applied voltage and diluting the protein sufficiently. Overall, there are many potential sample and instrumental causes of the observed rate differences, though many have been accounted for in the current work. An extensive cause and effect analysis was beyond the scope of the present work.

AF4 creates less concern for instrumental influences on the measured aggregation rate. Only the focus step, the concentrating of injected protein on the surface of the membrane prior to

separation, is likely to cause artifacts. This process could potentially result in protein adsorption or aggregation. Since the membrane is negatively charged, positively charged particles tend to stick to its surface. It was observed that positively charged α-chymo absorbed onto the regenerated cellulose membrane, and several injections were required to reach a steady state (i.e., membrane saturation). In addition, a loss in separation efficiency was observed after many injections and separations. The initial smooth, Gaussian distribution of the monomer devolved into a tailed elution of protein at longer retention times, likely due to protein-protein attraction at the membrane surface. A new membrane was used after every two experiments as the monomer peak began to shift and distort. This will likely be a problem for any aggregation measured below the pI of the protein. An alternative means to deal with this is to treat the membrane with a cationic surfactant to electrostatically repel the protein.[61] This strategy was not pursued as it adds further uncertainty due to protein-surfactant interactions.

### *2.4 Conclusions*

This study investigated the application of an aerosol-based technique, differential mobility analysis (DMAS), as an alternative method to quantify protein aggregation kinetics. Building on two previous studies, the method described here is more generally applicable, as it can be used to assess protein aggregation in any buffer. Additionally, DMAS was directly cross-validated with an orthogonal liquid-based separation technique, asymmetrical-flow field-flow fractionation (AF4). Consistent rate constants were obtained between the two methods; second order for bovine serum albumin (BSA) and first order for α-chymotrypsinogen A (α-chymo). The two techniques have different advantages that lend themselves to specific applications. AF4 yielded more consistent data, as one standard deviation of the monomer peak area was 1% – 5%, compared to

5% – 10% for DMAS. However, the DMAS method is much faster in practice; the AF4 method required 34 min for analysis, while the DMAS analysis was complete in just 4 min after a single, 1 h capillary equilibration, an important advantage for thorough characterization of various aggregation conditions. As a result, this study accommodated three times as many measurement results by DMAS compared with AF4. Also, AF4 uses substantial amounts of mobile phase during separation; roughly three liters of buffer were required per experiment. In contrast, DMAS uses a gas phase to separate the particles, resulting in minimal waste. Finally, approximately 100 μg of protein was injected per measurement for AF4, compared with 100 ng for DMAS. In this respect, AF4 is comparable to SEC, the current gold standard method in industry. DMAS has potential for screening valuable proteins in limited supply, as an entire kinetics study requires only 2 mg (limited primarily by buffer evaporation during heating). However, DMAS has several limitations, including dilution, buffer exchange, buffer volatility, capillary adsorption and droplet aggregation that, while controlled to the extent possible in this study, could be improved in future developments. Future work could also include hyphenation of DMAS with mass spectrometry to determine concurrent kinetic and structural information, for instance whether there is a specific aggregation-prone region and how this might change with different applied stresses, and further optimization of the electrospray process for proteins to reduce protein loss artifacts and further reduce overall analysis time.

## *2.5 Supplemental Information*

### *2.5.1 Asymmetrical-flow field-flow fractionation (AF4) Overview*

AF4 is an analytical technique for size-fractionation of particles over a wide range, from roughly 1 nm up to several hundred nanometers.[47] This technique separates particles in a mobile

solution phase with an applied cross flow field based on particle diffusive properties (i.e., diffusion coefficient), which is in turn related to hydrodynamic size. Separation is performed in a semi-permeable channel, with an impermeable upper surface and a permeable bottom plate consisting of a porous frit material covered by an ultrafiltration membrane. Particles are concentrated onto the membrane at a specific point by a focus flow with opposing flows coming from the inlet and the outlet of the channel as shown in Figure 2.5. In normal mode, particles simultaneously diffuse away from the membrane in relation to their diffusion coefficient, which can be related to the size of the particles. When the focus flow stops, the laminar parabolic flow carries the particles through the channel, with the smaller particles (highest diffusion coefficient) nearer to the center of flow and the larger particles closer to the membrane or accumulation wall. As a result, smaller particles elute first and can be detected in various ways, including absorbance, fluorescence, multi-angle light scattering and dynamic light scattering.

AF4 has been compared to other analytical techniques for the characterization of protein aggregation. AF4 was found to have an intermediate resolution between size exclusion chromatography (SEC) and analytical ultracentrifugation (AUC).[62] When compared to SEC, AF4 was found to be less prone to loss of aggregates and incomplete determination of protein oligomer distributions during aggregation. AF4 also has more flexibility in terms of mobile phase selection and shows consistent recovery.[63] AF4 tends to show more peak asymmetry and peak drift than SEC.[64] Overall, AF4 shows consistent data with SEC with less of a propensity to lose larger aggregates during analysis.

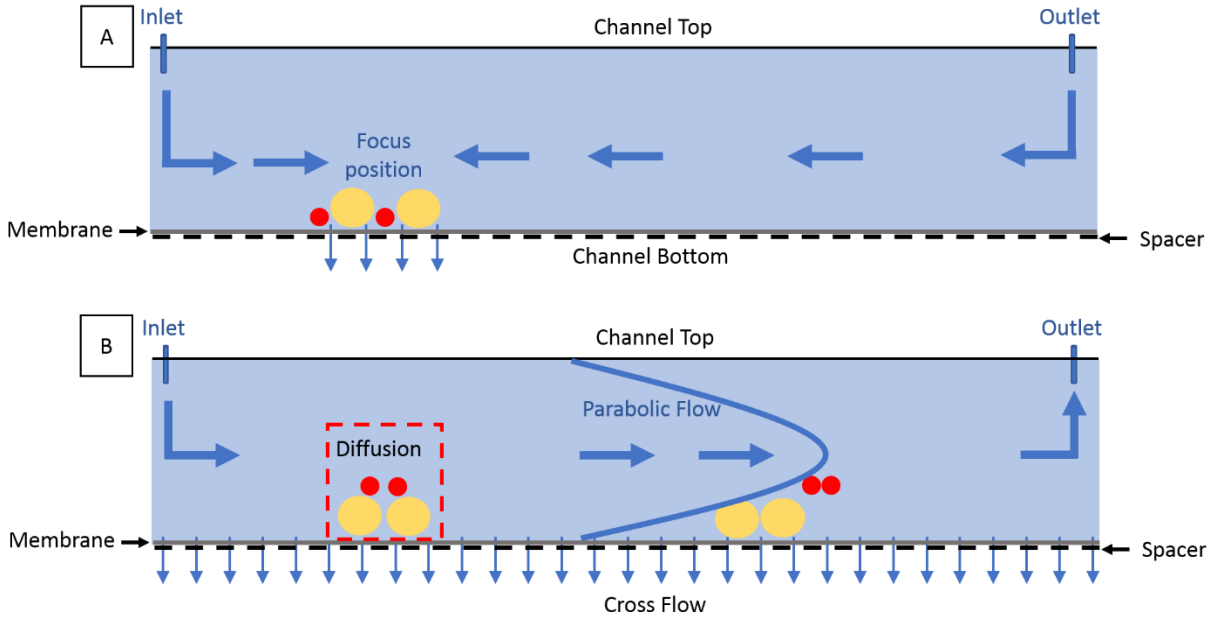


**Figure 2.5:** AF4 method for the separation of nano scale particles. Balanced entry and exit flows form a narrow band of analyte on the membrane during focusing (A). Particles diffuse away from the membrane, separating based on their size (B). When the exit flow stops, a laminar flow carries particles through the chamber and the smaller particles are detected first.

*2.5.2 Aggregation Rate Order Determination*

The molarity vs. time plots for various aggregation conditions were also converted to ln (molarity) vs. time and $(\text{molarity})^{-1}$ vs. time. The $R^2$ values for each plot were compared to determine if the aggregation was fit best as zero, first or second order. Figures 2.6, 2.7 and 2.8 are examples of the three fits for differential mobility analysis measurements of 1 mg $mL^{-1}$ BSA incubated at 70 $^{o}$C. The $R^2$ values for all experiments are included in Table 2.4. The error bars indicate one standard deviation of the means of three samples (each sample was measured three times).

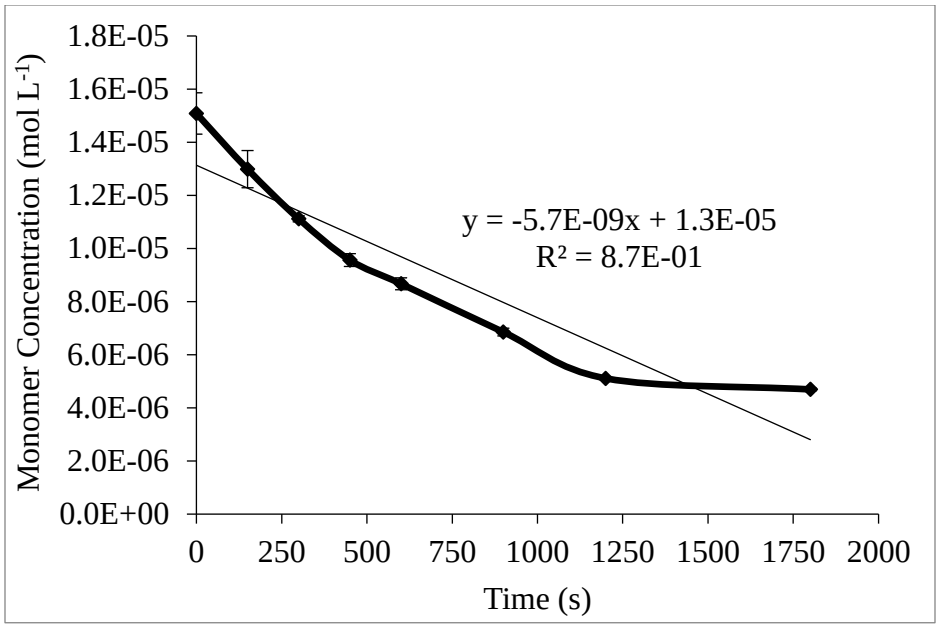


**Figure 2.6:** The monomer concentration vs. time plot (zero order) for 1 mg $mL^{-1}$ BSA incubated at 70 $^{o}$C. The $R^2$ value is 0.87.

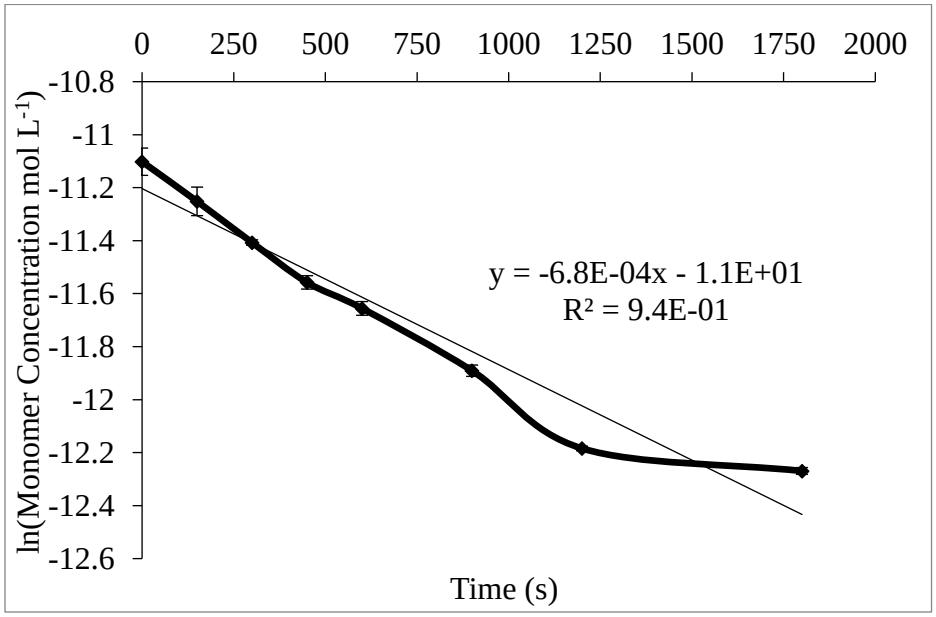


**Figure 2.7:** The ln (monomer concentration) vs. time plot (first order) for 1 mg $mL^{-1}$ BSA incubated at 70 $^{o}$C. The $R^2$ value is 0.94.

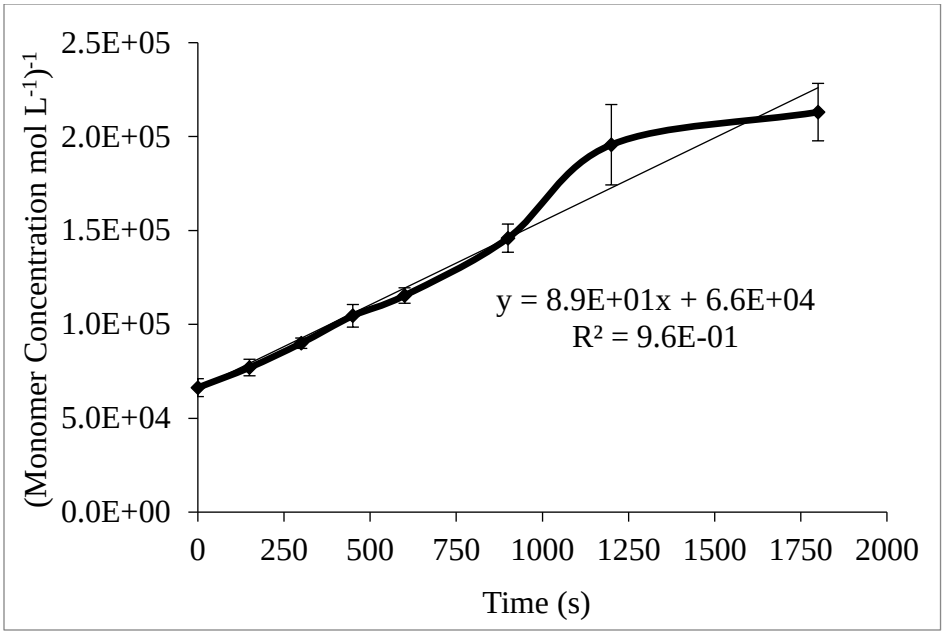


**Figure 2.8:** The (monomer concentration)$^{-1}$ vs. time plot (second order) for 1 mg mL$^{-1}$ BSA incubated at 70 ºC. The $R^2$ value is 0.96.

**Table 2.4:** $R^2$ values for zero, first and second order fits to all experiments. A few cases showed very similar first and second order fits, but overall BSA showed second order aggregation and α-chymo showed first order.

| Experimental Condition | Differential Mobility Analysis | | | Asymmetrical Flow Field Flow Fractionation | | |
|---|---|---|---|---|---|---|
| - | Zero Order | First Order | Second Order | Zero Order | First Order | Second Order |
| 1 mg mL$^{-1}$ BSA, 75 ºC | 0.80 | 0.96 | 0.99 | 0.66 | 0.85 | 0.97 |
| 1 mg mL$^{-1}$ BSA, 70 ºC Day 1 | 0.82 | 0.95 | 1.0 | 0.83 | 0.94 | 0.99 |
| 1 mg mL$^{-1}$ BSA, 70 ºC Day 2 | 0.87 | 0.94 | 0.97 | 0.80 | 0.92 | 0.98 |
| 1 mg mL$^{-1}$ BSA, 70 ºC Day 3 | 0.82 | 0.94 | 0.99 | 0.85 | 0.95 | 0.99 |
| 1mg mL$^{-1}$ BSA, 65 ºC | 0.75 | 0.86 | 0.91 | 0.80 | 0.89 | 0.95 |
| 1mg mL$^{-1}$ BSA, 60 ºC | 0.94 | 0.96 | 0.95 | 0.92 | 0.96 | 0.98 |
| 5 mg mL$^{-1}$ BSA, 70 ºC | 0.66 | 0.87 | 0.99 | 0.76 | 0.91 | 0.99 |
| 1.5 mg mL$^{-1}$ BSA, 70 ºC | 0.80 | 0.92 | 0.98 | 0.83 | 0.99 | 0.98 |
| 1 mg mL$^{-1}$ α-chymo, 62.5 ºC | 0.86 | 1.0 | 0.89 | 0.85 | 0.99 | 0.91 |
| 1 mg mL$^{-1}$ α-chymo, 60 ºC | 0.96 | 0.98 | 0.89 | 0.93 | 1.0 | 0.93 |
| 1 mg mL$^{-1}$ α-chymo, 57.5 ºC | 0.78 | 0.99 | 0.87 | 0.78 | 0.98 | 0.93 |
| 1 mg mL$^{-1}$ α-chymo, 55 ºC | 0.90 | 0.98 | 0.98 | 0.97 | 0.99 | 0.94 |
| 2 mg mL$^{-1}$ α-chymo, 60 ºC | 0.84 | 0.98 | 0.93 | 0.83 | 0.99 | 0.87 |
| 1.5 mg mL$^{-1}$ α-chymo, 60 ºC | 0.84 | 0.99 | 0.87 | 0.83 | 0.99 | 0.90 |

# Chapter 3: Calibrated Mass Distribution Measurements of Bimetallic Nanoparticles

## *3.1 Introduction*

Supported metallic nanoparticles are of broad interest due to their tunable optical[65], antimicrobial[66], and catalytic properties.[67] Because of their promise in various applications, many demonstrations for their use have been reported, where modifying particle size, interfacial properties, composition ratios, and surface structure has led to tuning variables for controlled optical and electronic properties.[68] Specifically for spatial and geometrical control over supported nanoparticles through ligand chemistry, higher sensitivity surface-enhanced Raman scattering, improved and selective antimicrobial behavior, and improved catalytic performance have been demonstrated. The catalytic performance has been an accelerant in the research and development for elucidating structure-function properties for improved design rules.[69] Because the enhanced reactivity is due to active sites on the supported metal structure within the hybrid material, approaches such as deposition and direct growth onto larger supports are used to preserve the size, and thus catalytic properties, of the material. However, variation in performance is significant and reproducibility of particle synthesis, assembly, and activation of their properties has been a persistent challenge for more than two decades.

Identifying specific material structure-property relationships for better design, higher performance, and limit in batch-to-batch variability for commercial and industrial applications will require improved methods for characterizing a more complete particle population, instead of trying to find “the-needle-in-haystack” subpopulation that could be responsible for a majority of the observed enhanced property of interest. Physical characterization has proven difficult and primarily consists of microtomic and microscopic analyses, such as high-angle annular dark-field

scanning-transmission electron microscopy and tomography[70,71,72] , and bright-field transmission electron microscopy[73,74] (TEM). The spatial atomic distribution is often measured by energy dispersive X-ray spectroscopy and further chemical characterization has also included additional spectroscopy methods (e.g., using electron energy loss spectroscopy). All these techniques are limited by the small sample size, which often consists of single particles per image, and statistically significant sampling of the populations can be intractable. Alternative approaches that can acquire similar information, provide a more statistical representation of the property of interest, and be higher throughput are necessary for both research and manufacturing applications. One ensemble measurement is small-angle X-ray scattering, which was previously used to differentiate homogeneous and heterogenous spatial loading of small copper catalyst particles in mesoporous silica supports.[75] Another option is the differential mobility analyzer combined with inductively coupled plasma mass spectrometry (DMA-ICP-MS). This developing technique consists of the differential mobility analyzer (DMA), an aerosol electrical mobility measurement that separates particles by size, and inductively coupled plasma mass spectrometry (ICP-MS), an elemental analysis technique that gives elemental mass information. The combined technique can give the mass concentration of multiple elements across the particle size distribution. Some examples include measurements of trace semiconductor gas[76], laser ablation products[77], protein particles[33], lead nitrate particles[32], and platinum loading and release from gold nanoparticles[78]. The ICP-MS can also be run in single particle mode (sp-ICP-MS) in which individual particles are quantified in dilute samples via a rapid analysis mode. DMA-ICP-MS run in single particle mode (sp-DMA-ICP-MS) has been used to distinguish aggregates from primary particles[79] and to determine the geometry of nanorods[80].

While DMA-ICP-MS has been used for various applications, the calibration of measurements has been limited. sp-DMA-ICP-MS measurements are calibrated by standard methods used for sp-ICP-MS measurements: a particle of known mean diameter is measured and the sphere equivalent mass is assigned to the mean ICP-MS response.[81] Validation of the rotating disk diluter scanning mobility particle sizer ICP-MS consisted of comparisons between mass distributions derived from number distributions from the condensation particle counter (CPC) detector, and mass distributions from the ICP-MS.[82] Another approach calibrated the total mass from the DMA-ICP-MS distribution by relating the response to the total number measured by the DMA-CPC for a standard of well-known total mass, density, and average particle size.[36] Alternatively, it was suggested to use the known total mass of gold nanoparticle (AuNP) reference materials. A simple calibration method for DMA-ICP-MS is lacking, specifically for elements that do not have a relevant nanoparticle reference material. A direct comparison to an ionic standard should in principle be sufficient to calibrate the measurement. I used this approach to test the calibration of synthesized Au@$TiO_2$ particles following a procedure reported to prepare catalysts.[69] I developed a calibration technique for quantifying gold and titanium and compared the total mass measured across the size distribution with certified values of ionic standards, acid digestion measurements of particulate gold, and gravimetric measurements of titanium. I also measured several control particles: gold nanorods (AuNR), gold nanocubes (AuNC), gold nanoparticles (AuNPs), and platinum coated gold nanoparticles (Pt@AuNPs). DMA-ICP-MS presents a promising technique for further understanding of bimetallic nanoparticles by measuring calibrated mass distributions of multiple elements concurrently.

## *3.2 Materials and Method*

### *3.2.1 Chemicals*

Sodium citrate dihydrate (≥ 99%), oleylamine (70%), tetralin (97%), gold (III) chloride hydrate (99.999%), hexane (≥ 97.0%), and t-butylamine-borane complex (97%) were purchased from Sigma Aldrich (St. Louis, MO, USA). Optima grade nitric acid, optima grade hydrochloric acid, and methanol (99.9%) were purchased from Thermo Fisher (Waltham, MA, USA). 2-propanol (100%) was purchased from J.T. Baker (Phillipsburg, NJ, USA). Sodium 1-hexadecanesulfonate was purchased from TCI (Portland, OR, USA). Thiourea (99%) was purchased from Alfa Aesar (Haverhill, MA, USA). Aluminum oxide particles (Cat. # 90-187015) were purchased from Allied High Tech Products (Compton, CA, USA). Cerium oxide particles (Cat. # 0300) were purchased from Nanophase (Burr Ridge, Il, USA). Nominally 10 nm gold nanoparticles were purchased from Ted Pella (Redding, CA, USA). Nominally 30 nm gold nanoparticles LGCQC5050 were purchased from LGC (Teddington, UK). National Institute of Standards and Technology (NIST) SRM 1898 titanium dioxide particles (also known as P25) were used. Samples were prepared using 18.2 MΩ·cm deionized water (Model 2121AL, Aqua Solutions, Jasper, GA, USA).

### *3.2.2 Standards*

#### 3.2.2.1 Gold ionic standard

VWR BDH Aristar (Radnor, PA, USA) 999 μg $mL^{-1}$ ± 5 μg $mL^{-1}$ gold in 2% $HNO_3$ was used as a stock standard for dilutions to 100 μg $L^{-1}$ – 1 000 μg $L^{-1}$ in 378 mg $L^{-1}$ citrate or 378 mg $L^{-1}$ citrate and 0.1% thiourea in Lo-bind microcentrifuge tubes.

3.2.2.2 Titanium ionic standard

NIST SRM 3162a Titanium standard solution was used as a stock standard for dilutions to 100 μg $L^{-1}$ – 5 000 μg $L^{-1}$ in 378 mg $L^{-1}$ citrate in lo-bind microcentrifuge tubes. The certified concentration is 9.879 mg $g^{-1}$ ± 0.019 mg $g^{-1}$.

3.2.2.3 Quality control gold nanoparticles

QC1 is citrate stabilized, nominally 30 nm AuNPs obtained from Ted Pella. Total mass of dilutions was determined gravimetrically based on sp-ICP-MS measurements of the nanoparticle stock mass concentration: 47.4 μg $g^{-1}$ ± 5.6 μg $g^{-1}$.

QC2 is citrate stabilized, nominally 60 nm AuNPs obtained from Ted Pella. Total mass of dilutions was determined gravimetrically based on sp-ICP-MS measurements of the nanoparticle stock mass concentration: 52.5 μg $g^{-1}$ ± 5.7 μg $g^{-1}$.

*3.2.3 Nanomaterials*

3.2.3.1 Gold nanorods (AuNR)

Citrate stabilized AuNR of three different geometries (peak absorbance 660 nm: 20 nm width and 55 nm length. Peak absorbance 800 nm: 10 nm width and 50 nm length. Peak absorbance 980 nm: 10 nm width and 60 nm length) were purchased from nanoComposix (San Diego, CA, USA).

3.2.3.2 Gold nanocubes (AuNC)

Citrate stabilized AuNC with 60 nm edge length were purchased from Nanopartz (Loveland, CO, USA).

3.2.3.3 Platinum coated gold nanoparticles (Pt@AuNPs)

Ionic platinum was loaded onto 30 nm AuNPs (Pt@AuNPs) from Ted Pella by applying cisplatin solution to suspensions of polyethylene glycol-containing-dendron stabilized AuNPs.

*3.2.4 Titania particles coated with small gold particles (Au@$TiO_2$)*

Gold nanoparticles (4 nm) were synthesized and adsorbed to larger titania particles.[83] The Au@$TiO_2$ particle solution was then dried and heated before sonication to redisperse the particles in water.

3.2.4.1 Gold nanoparticle (AuNP, 4 nm) synthesis

Tetralin (10 mL), oleylamine (10 mL), and $HAuCl_4$-$3H_2O$ (50 mg) were mixed in a 100 mL round bottom flask heated at 40 $^oC$ while stirring. The solution turned orange. t-butylamine-borane complex (45 mg), tetralin (1 mL), and oleylamine (1 mL) were mixed in a small vial and bath sonicated. The reducing agent mixture was injected into the 100 mL round bottom flask solution and left for 1 h. The contents of the round bottom flask were transferred slowly to 200 mL isopropanol while stirring. Stirring was stopped after 10 min and the particles were left for 12 h. 200 mL supernatant was removed, and the remaining dispersion was transferred to centrifuge tubes. The AuNPs were redispersed by bath sonication and then centrifuged at 6 000 rcf for 5 min. The supernatant was removed, replaced with isopropanol, and repeated for three total cleaning cycles. After the final centrifugation, the supernatant was removed, and the final product was dispersed in 10 mL hexane (final concentration was approximately 2.5 mg $mL^{-1}$).

3.2.4.2 AuNP Adsorption to $TiO_2$

Sodium 1-hexadecanesulfonate (NaHDS, 5 mg) was bath sonicated in methanol (1 mL). Calcined P25 (50 mg) was bath sonicated in hexane (12 mL) and NaHDS (625 μL). 4 nm AuNPs

1 μL – 1 000 μL was added and the dispersion was shaken vigorously. The dispersion was then centrifuged at 6 000 rcf for 5 min. The supernatant was removed (AuNP concentration in supernatant was tested with UV-Vis), hexane was replaced, and the process repeated for three total cleaning cycles. After the final centrifugation the supernatant was removed, and the dispersion was air dried.

3.2.4.3 UV-Vis

UV-Vis absorbance measurements were made from 200 nm – 800 nm to test the concentration of AuNPs left in the supernatant after adsorption relative to the stock concentration of AuNPs (Model Lambda 750, Perkin Elmer, Waltham, MA, USA). A slight peak was detectable around 530 nm. The AuNPs in solution were undetectable for samples with gold loading equal to or below 5E-3 mg AuNPs per 1 mg P25.

3.2.4.4 Heat treatment

Dried Au@$TiO_2$ powder was smoothed with wax paper and transferred to a crucible for heating. The powder was heated at 500 $^oC$ for 1 min to remove adsorbed oleylamine.[84]

3.2.4.5 Storage

After heating, any powder not used immediately was transferred to a parafilm sealed container and stored in a desiccator. Initial experiments found significant changes in AuNP size over 6 months when not stored properly.

3.2.4.6 Sonication:

After sufficient heating, the Au@$TiO_2$ powder was dispersible in water. Au@$TiO_2$ (10 mg) powder was dispersed in 10 mL 378 mg $L^{-1}$ citrate in water and probe sonicated with the standard tip at 3 amp for 15 min (0.8 on/off) in an ice bath. Laser scattering measurements (Model: LA-

950V2, Horiba, Kyoto, Japan) indicate that most of the particle volume distribution reduced to the sub 200 nm size range.[85]

3.2.4.7 Au acid digestion

Sample powder (2 mg) was added to 7% aqua regia (10 g) and left for 48 h. The digestion sample was then diluted to approximately 10 μg $L^{-1}$ gold in 1% aqua regia with 0.1% thiourea. The gold concentration was then determined by traditional ICP-MS measurements with comparison to an ionic standard calibration curve from 1 μg $L^{-1}$ – 50 μg $L^{-1}$.

*3.2.5 DMA-ICP-MS instrumentation*

The customized nano electrospray-DMA system used in this study (Figure 1.8) has been described previously.[86] Briefly, the nano electrospray (nES, Model 3480, TSI, Shoreview, MN, USA) used an aerosol flow rate of 1 L $min^{-1}$ air. The nES voltage was set to 3 kV with a resulting current of 200 nA – 400 nA. The pressurized sample chamber was set to 26 kPa (3.7 psi). The samples were sprayed through a 40 μm inner diameter fused silica capillary. The aerosol was charged to a bipolar distribution by a Po-210 alpha-emitter (Model P-2042, TSI). The DMA (Model 3081, TSI) selected positively charged particles with a narrow mobility distribution. A custom LabVIEW (National Instruments, Austin, TX, USA) program was used to control the high voltage power supply (Model 205B-10R, Spellman, Hauppauge, NY, USA). The sheath flow was set to 10 L $min^{-1}$ argon. The particles selected by the DMA then passed through a custom gas exchange device (GED) described previously (Figure 1.6).[36] The size selected aerosol travels through a region surrounded by a porous $Al_2O_3$•$SiO_2$ membrane contained in a glass tube. Argon and air traverse the membrane by diffusion with minimal loss of particles. A 3 L $min^{-1}$ argon flow

outside the membrane travels in the opposite direction compared to the aerosol for improved exchange.

The glass capillary of the nES can be a severe limitation to consistent measurements. Both nanoparticles and ions tend to adsorb to the capillary to some extent, but more importantly, nanoparticle adsorption leads to reductions in capillary flow rate and eventually clogs the capillary. For this reason, I cleaned the capillary with ethanol and buffer between nanoparticle measurements and used different capillaries for nanoparticles and ionic solutions.

An Agilent (Santa Clara, CA, USA) 7900 ICP-MS was used as a detector. Time resolved analysis measurements of $^{197}$Au and $^{47}$Ti were made with a 1 s integration time. The most abundant Ti isotope, $^{48}$Ti, was not used, as the purpose of this study was to simultaneously detect low concentration gold and high concentration titanium without saturating the detector. The ICP-MS was calibrated and tuned in batch mode before hyphenation with DMA occurred. The instrument was tuned daily to optimize the $^{197}$Au intensity. Because of the presence of known polyatomic and isobaric interferences for the most abundant titanium isotopes, the responses for $^{47}$Ti, $^{48}$Ti, and $^{49}$Ti were examined by comparing the linearity of the calibration curve for each isotope. The design for introduction of argon through the electrospray at the appropriate rates for ICP-MS is referenced above. Additional ports to control make up and dilution argon flows at the ICP-MS inlet were examined to evaluate $^{197}$Au intensity repeatability for both ionic standards and particles. The repeatability of signal intensities for calibration standards were checked daily to ensure data comparability for all measurements.

Measurements were made of titanium and gold mass distributions for various particles. The ICP-MS operated continuously while the DMA stepped through a series of voltages corresponding to specific mobility diameters. The DMA remained at each voltage for 30 s, allowing for multiple

measurements by the ICP-MS per selected mobility diameter. The average ICP-MS response was determined for each diameter and the data were converted from a time distribution to a diameter distribution. The data were corrected for background noise, and the mass distribution post-DMA was related to the mass distribution pre-DMA by the DMA transfer function, and the charging probability at each diameter (because only charged particles can transverse the DMA). Finally, the peak area of the mass distribution was integrated and plotted against the known total mass concentration from the certified values of ionic standards, acid digestion measurements of particulate gold, and gravimetric measurements of titanium.

*3.2.6 Calculations*

The peak mobility ($Z_p$) of a charged particle exiting the DMA is obtained using the following equation:

$$Z_p = \frac{q_{sh} ln(r_2/r_1)}{2\pi LV} \quad (3.1)$$

$q_{sh}$ is the sheath flow, $r_2$, and $r_1$ are the outer and inner electrode radii respectively, $L$ is the length, and $V$ is the electrical potential.

A key advantage of the DMA is that it has a quantified transfer function. This is essential for determining the size distribution of the aerosol entering the DMA from measurements of the aerosol exiting the DMA. Another advantage is that one can obtain high resolution mobility measurements by using a low aerosol flow and a high sheath flow ($\Delta Z_p/Z_p = 0.05$ for a flow ratio of 20).

The sphere equivalent mobility diameter distribution is of interest rather than the mobility distribution. For singly charged particles, the diameter is related to the mobility via the following implicit equation:

$$\frac{D_p}{C_c(D_p)} = \frac{ne}{3\pi\mu Z_p} \tag{3.2}$$

$n$ is the particle charge, $e$is the elementary charge, $\mu$ the viscosity, and $C_c$ the Cunningham slip correction.

$$C_c = 1 + K_n\left(\alpha + \beta(\exp(-\gamma/K_n))\right) \tag{3.3}$$

$K_n$ is the Knudsen number, $2\lambda/D_p$, where $\lambda$ is the mean free path, and $\alpha$, $\beta$, and $\gamma$ are empirical constants. In this case I use the values $\alpha$ = 1.165, $\beta$ = 0.483, and $\gamma$ = 0.997.[87] The slip correction applies to both solid and liquid particles.[88]

Knutson and Whitby derived an equation relating the particle concentration at the DMA exit to an integral involving the DMA transfer function and the number size distribution.[11] For the common condition that the aerosol distribution is broad compared to the transfer function, the following relationship is obtained:

$$\frac{dN(D_p)}{dD_p} = \frac{N_{CPC}(D_p)B(D_p)}{\delta P(D_p)} \tag{3.4}$$

Where d$N$($D_p$) is the number concentration of particles with diameters between $D_p$ and $D_p$ + $dD_p$. The proportionality constants are the singly charged fraction, $P(D_p)$[27], which accounts for the difference between the bipolar charge distribution at the inlet and the singly charged particles at the outlet, the aerosol to sheath flow ratio, $\delta$, which relates to the DMA sizing resolution, and

the function $B(D_p)$, which arises from the transformation from a mobility distribution to a diameter distribution.[56]

The mass distribution is the quantity of interest, which is related to the number distribution via the following formula for spherical particles:

$$\frac{dM(D_p)}{dD_p} = \frac{1}{6}\pi D_p^3 \rho \frac{dN(D_p)}{dD_p} \tag{3.5}$$

Where $\rho$ is the particle density. Multiplying both sides of Equation 3.4 by $\frac{1}{6}\pi D_p^3 \rho$, one obtains:

$$\frac{dM(D_p)}{dD_p} = \frac{M_{det}(D_p)B(D_p)}{\delta P(D_p)} \tag{3.6}$$

Where $M_{\text{det}}$ is the mass concentration of the outlet aerosol measured by a mass detector such as a filter/gravimetric weighing, a tapered element microbalance, or ICP-MS. ICP-MS, the method of interest here, has the advantage of having a much higher sensitivity to small masses compared to other methods. One of the major interests is in computing the total mass concentration. This was obtained by summing the size bins:

$$M_T = \sum_{i=1}^{n} \frac{\Delta M_i}{\Delta D_i} \Delta D_i = \sum_{i=1}^{n} \Delta M_i \tag{3.7}$$

One case of interest is a bimetallic catalyst particle such as a titanium particle with small gold nanoparticles adsorbed on the surface. In this case I am interested in the mass distribution of gold, $dM_{Au}/dD_p$, where the detector response is only for the gold. In this case the gold mass is only a small fraction of the total mass of the particle. The corresponding equation for the relationship between the mass distribution and the ICP-MS measurements for gold is:

$$\frac{dM_{Au}(D_p)}{dD_p} = \frac{[M_{det,Au}(D_p) - M_{background,Au}]B(D_p)}{\delta P(D_p)} \quad (3.8)$$

The ICP-MS signal intensity in counts per second (cps) is averaged for each period corresponding to different mobility diameters. The ICP-MS signal intensity at no applied voltage is subtracted from each point to correct for the background signal.

### *3.3 Results*

Determination of gold concentration on $TiO_2$ provides the baseline for observed responses for supported metal systems in reactivity, optical response, and other applied performance metrics. To determine the relationship between metal loading of uniform particles and performance, accurate quantification of metal amounts or elemental ratios of metal and scaffold (i.e., gold and titanium) is necessary. Here, the elemental response for different metal states, primary particles, ions, and supported metal particles are examined with hyphenated nES-DMA-GED-ICP-MS to develop improved methods for characterizing multi-component metal nanoparticles. Although previous work has suggested accurate quantification was straightforward for all metal matter forms, no in-depth study has investigated possible sources of error that could be present for accurate metallic ratios or absolute quantification.

Calibration curves for gold and titanium are shown in Figures 3.1 and 3.2, respectively. The curves plot the mass concentration (from the certified concentration of the ionic standard, acid digestion measurements for AuNP samples, or gravimetric analysis for $TiO_2$ samples) compared to the integrated peak area of the nES-DMA-GED-ICP-MS response. Figure 3.1 indicates two response regimes: one for the gold ionic standard and monodisperse AuNPs, and a second for polydisperse Au@$TiO_2$ particles. Figure 3.2 indicates the difference between the titanium ionic

standard and the pristine $TiO_2$ particles (no gold). The nES-DMA-GED-ICP-MS response is significantly higher for Au@$TiO_2$ particles than the ionic standards or monodisperse nanomaterials (beyond the error bars: one standard deviation of measurements from three replicate measurements from different days). This difference is consistent for gold and titanium. Figure 3.1 demonstrates the agreement between the nES-DMA-GED-ICP-MS calculated $M_T$ and the mass concentration for the gold ionic standard and AuNPs QC1 and QC2, which indicates that the ionic and AuNP behavior through the nES is consistent. The agreement demonstrates the method is applicable to metallic nanoparticles of different sizes and over a broad concentration range. The data indicate that accurate measurements of Au@$TiO_2$ are more difficult than ionic samples or monodisperse particles.

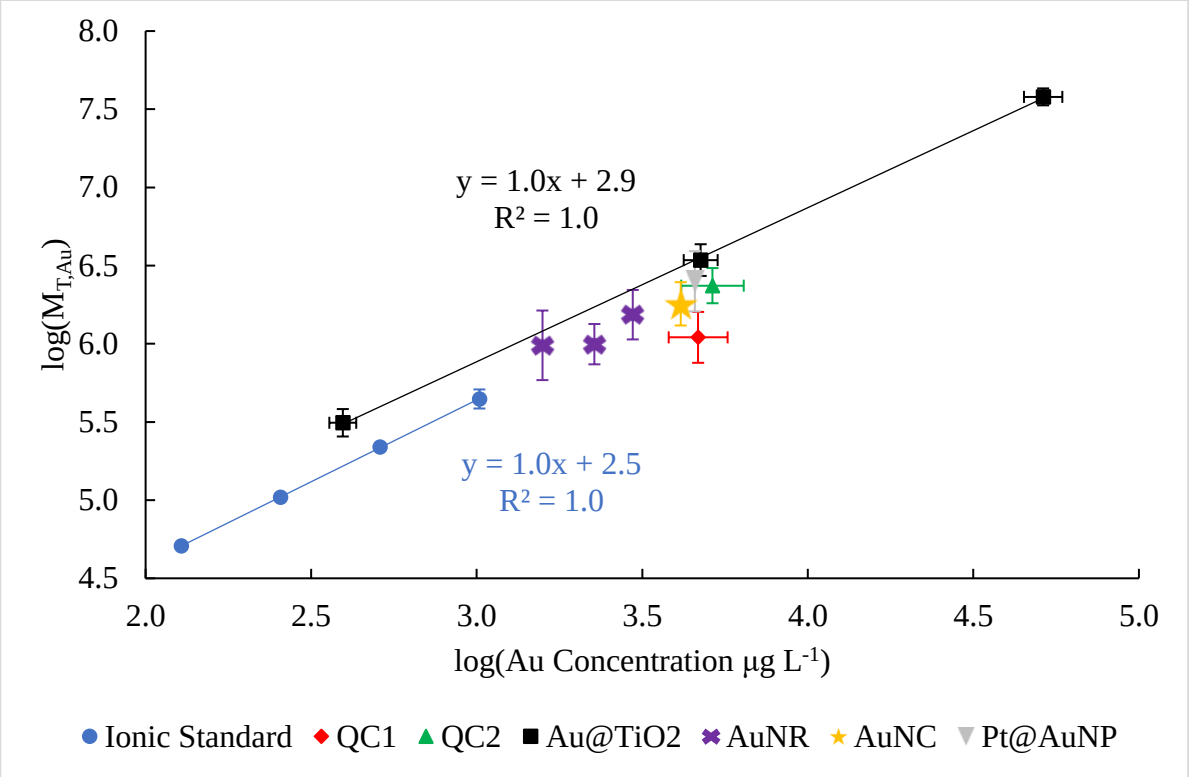


**Figure 3.1**: Gold calibration curve plotting known mass concentration against the summed nES-DMA-GED-ICP-MS response. The axes are scaled logarithmically due to the wide range of concentrations measured. The blue circles are the gold ionic standard, black squares are Au@$TiO_2$, red diamonds are QC1, green triangles are QC2, purple X are AuNR, yellow stars are AuNC, and gray inverted triangles are Pt@AuNP. Y-axis error bars represent one standard deviation of measurements from several days (number of measurements n = 3). The x-axis error bars indicate one standard deviation and propagated uncertainty of the concentration of the ionic standard stock.

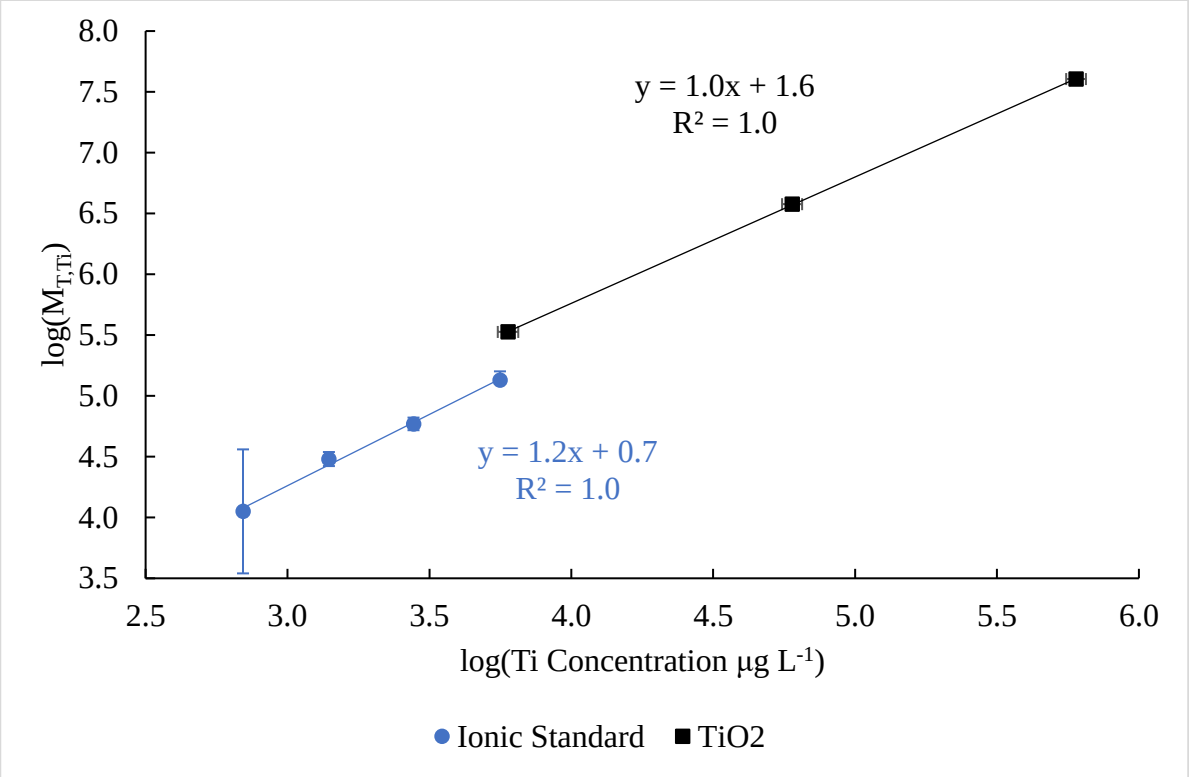


**Figure 3.2**: Titanium calibration curve plotting known mass concentration against the summed nES-DMA-GED-ICP-MS response. The axes are scaled logarithmically due to the wide range of concentrations measured. The blue circles are the titanium ionic standard, and the black squares are particulate $TiO_2$ samples (no gold). Y-axis error bars represent one standard deviation of measurements from several days (number of measurements n = 3). The x-axis error bars indicate one standard deviation and propagated uncertainty of the concentration.

The difference between the gold ionic standard and Au@$TiO_2$ particles when the DMA is not used (the nES is connected directly to the GED and then the ICP-MS) is shown in Figure 3.3. The data show a higher $^{197}$Au response for the Au@$TiO_2$ sample (black square) compared to ionic Au (blue circle). The comparison of Figures 3.1 and 3.3 suggests a significant portion of this bias does not derive from the DMA. This difference was not detected when the same measurements were made with a nebulizer instead of the nES and GED, as shown in Figure 3.4. The ideal behavior, if the nebulizer works as intended, is that the ionic standard and the Au@$TiO_2$ will fall on a single line. In Figure 3.4, the observed behavior is closer to this expectation than previous

figures. There is a minor difference, with higher response for the ionic standard relative to the Au@$TiO_2$, consistent with nanoparticle loss prior to measurement (plastic tubing used for pneumatic pump). This contrast between Figures 3.3 and 3.4 suggests the nES and/or the GED are contributing to the higher response for Au@$TiO_2$ particles. Some investigations of the nES are included in the supplemental information. Figure 3.14 (supplemental information) indicates some relationship between particle size and nES transport efficiency, but other undetermined variables also play a significant role and further research is required. In the remainder of this chapter, I focus on other factors related to the DMA.

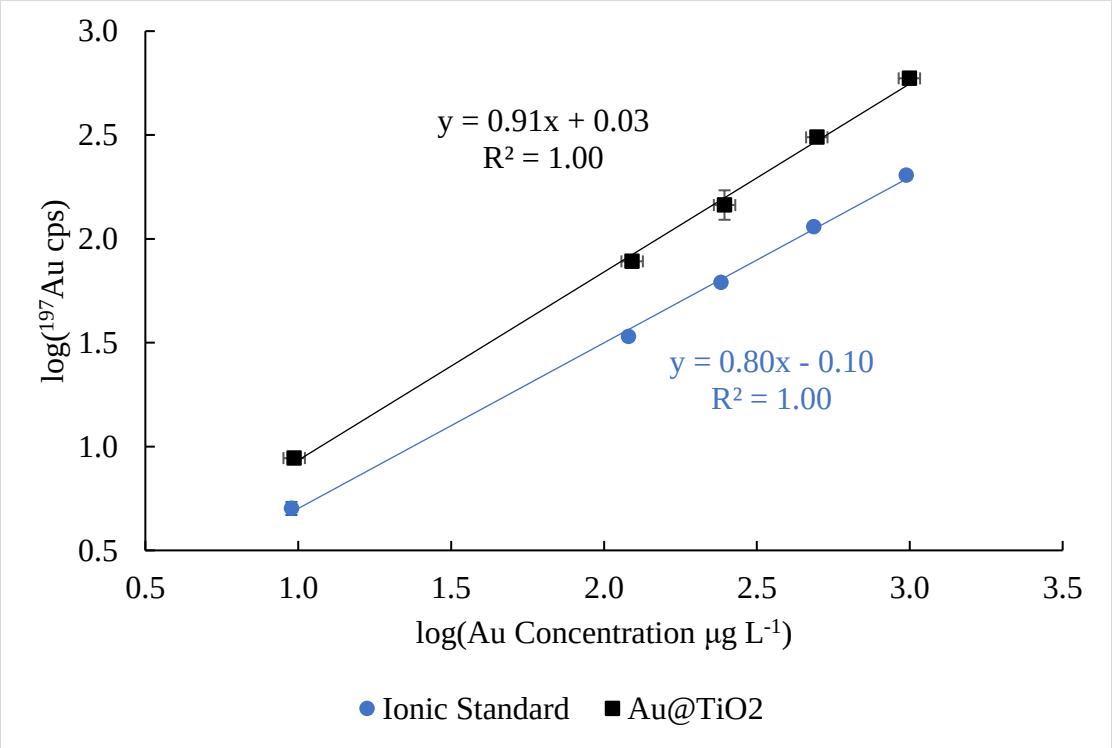


**Figure 3.3**: nES-GED-ICP-MS (no DMA) measurements of gold ionic standards diluted in citrate thiourea buffer (blue circles) and Au@$TiO_2$ samples (black squares). The axes are scaled logarithmically for convenient comparison to other figures. Y-axis error bars represent one standard deviation of triplicate measurements. The x-axis error bars indicate one standard deviation and propagated uncertainty of the concentration.

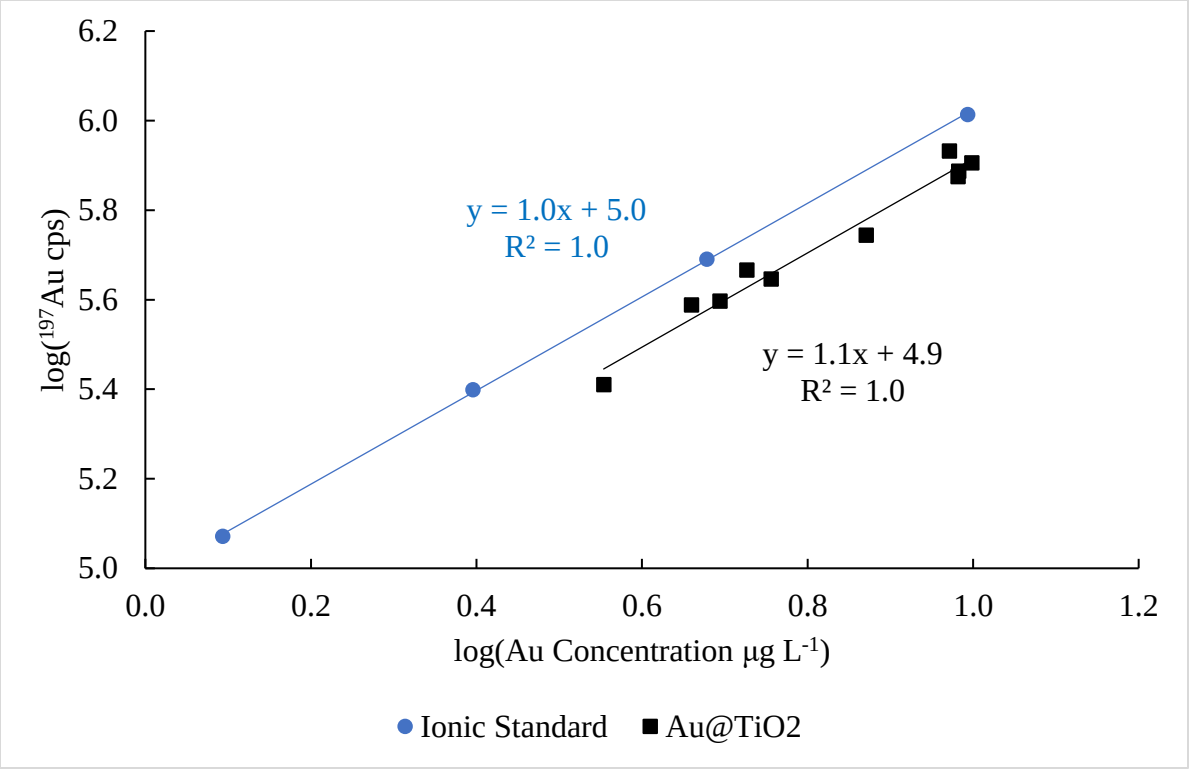


**Figure 3.4**: Nebulizer-ICP-MS (no GED or DMA) measurements of gold ionic standard diluted in 1% aqua regia, 0.1% thiourea (blue circles) and Au@$TiO_2$ samples diluted in 378 mg $L^{-1}$ citrate buffer (black squares). The axes are scaled logarithmically for convenient comparison to other figures.

The relationship between nES-DMA-GED-ICP-MS measurements of total gold mass of QC1 and QC2 and independent acid digestion measurements (data not shown) agreed with the relationship between nES-DMA-GED-ICP-MS measurements of the ionic standard and the certified mass concentration of the ionic standard (linear fit to blue, green, and red points in Figure 3.1). As a result, the nES-DMA-GED-ICP-MS measurement was able to determine representative mass distributions of QC1 and QC2 in Figure 3.5. nES-DMA-GED-ICP-MS measurements of QC1 and QC2 were acquired at a ten-fold dilution, but the values of $M_T$ were scaled proportional to the dilution such that the figure represents the original stock concentration.

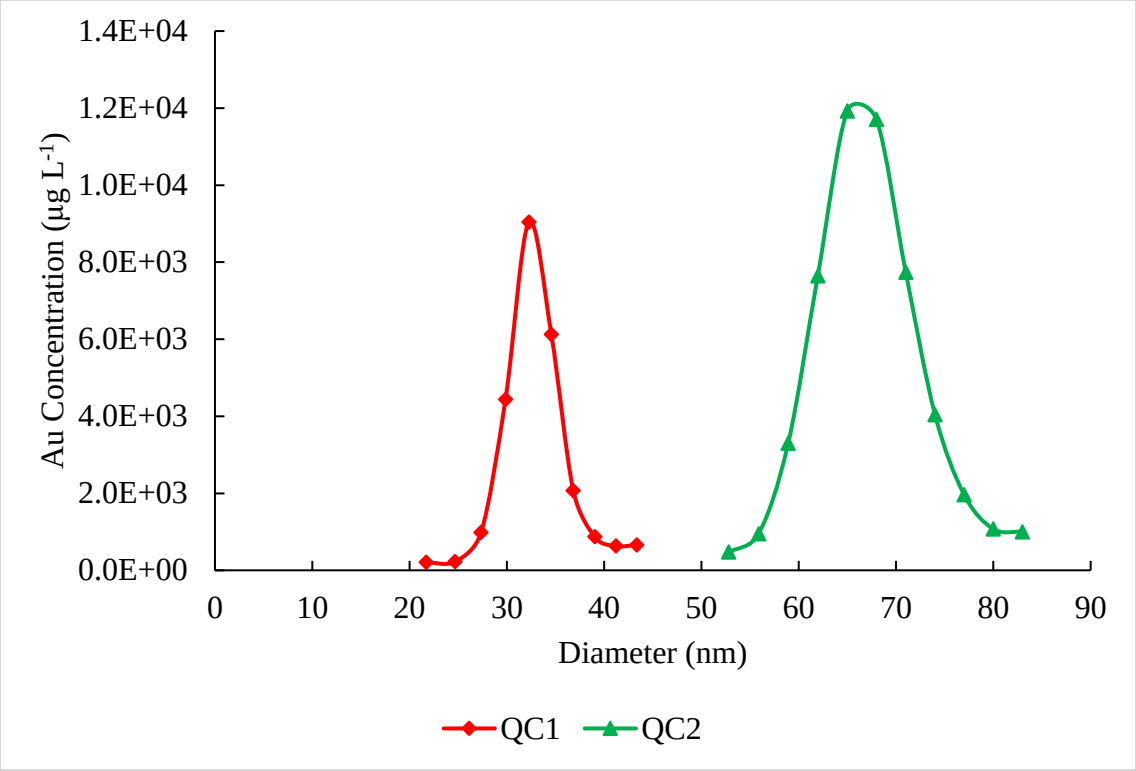


**Figure 3.5**: Average calibrated mass distribution of QC1 (red diamonds: 32 nm mode) and QC2 (green triangles: 66 nm mode).

Possible sources of the differences between the ionic standard and Au@$TiO_2$ particles derived from the DMA were investigated, such as the effect of particle shape and multiple charging. In Figure 3.1, monodisperse gold particles of various shapes (rods and cubes) were compared to the results for the ionic standard and the Au@$TiO_2$ particles. The rods and cubes tended to agree with the ionic standard better than the Au@$TiO_2$ particles, suggesting the particle shape is not the source of the error.

My analysis of the DMA above assumed that there are only singly charged particles. However, it is possible that there are doubly and triply charged particles. This can impact accurate quantification, because a triply charged 310 nm particle has roughly the same mobility as a 190 nm doubly charged particle and a 150 nm singly charged particle. I have considered the effect of

multiple charging for the largest possible size range, 10 nm – 230 nm, for the current instrument setup was measured. Results for the measured size distribution for Au@$TiO_2$ particles is given in Figure 3.6. To estimate the size distribution for larger particles, I made a linear fit of the data from 160 nm – 230 nm. Then I extended the line to the x-axis, resulting in an intercept near 310 nm, which was used as the largest particle size (all singly charged) for the charge correction calculation. I followed the approach of ISO 15900 for the charge correction and give the key steps of the analysis in the supplemental information (Equations 3.11 and 3.16).[89]

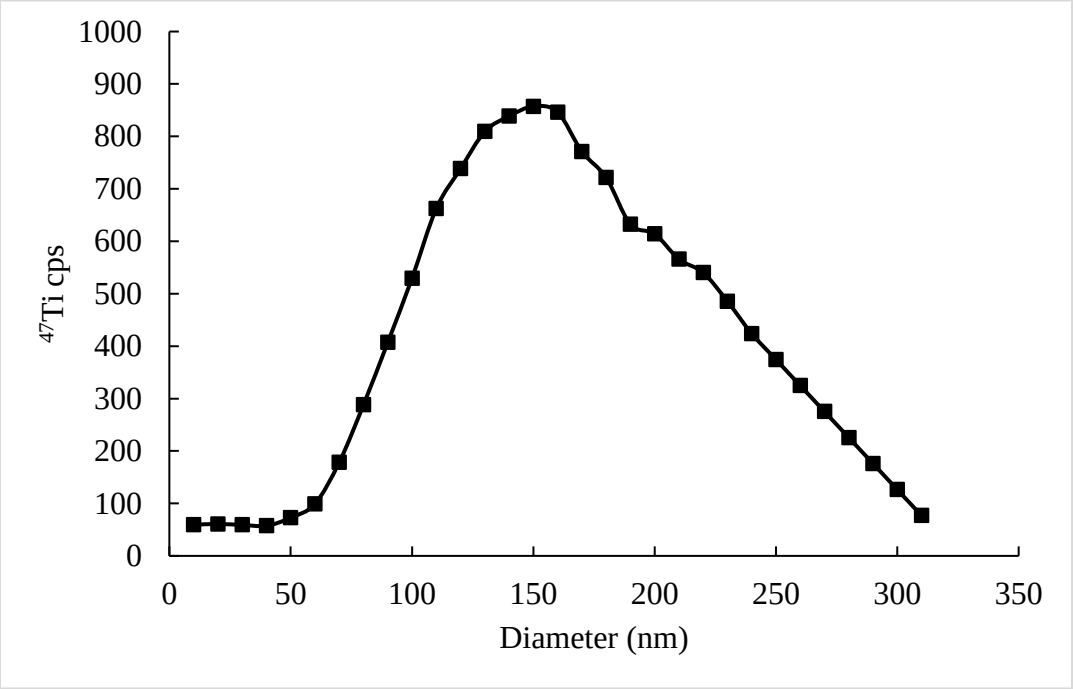


**Figure 3.6**: A modified nES-DMA-GED-ICP-MS full scan of $^{47}$Ti for an Au@$TiO_2$ solution. The measurement was made from 10 nm – 230 nm and a linear fit from 160 nm – 230 nm was extended to 240 nm – 310 nm.

Figure 3.7 illustrates the decrease in calculated mass from 50 nm – 190 nm due to the multiple charge correction. The total mass from 10 nm – 150 nm was reduced by 34% with the

correction for doubly charged particles and was reduced by 37% with the correction for doubly and triply charged particles.

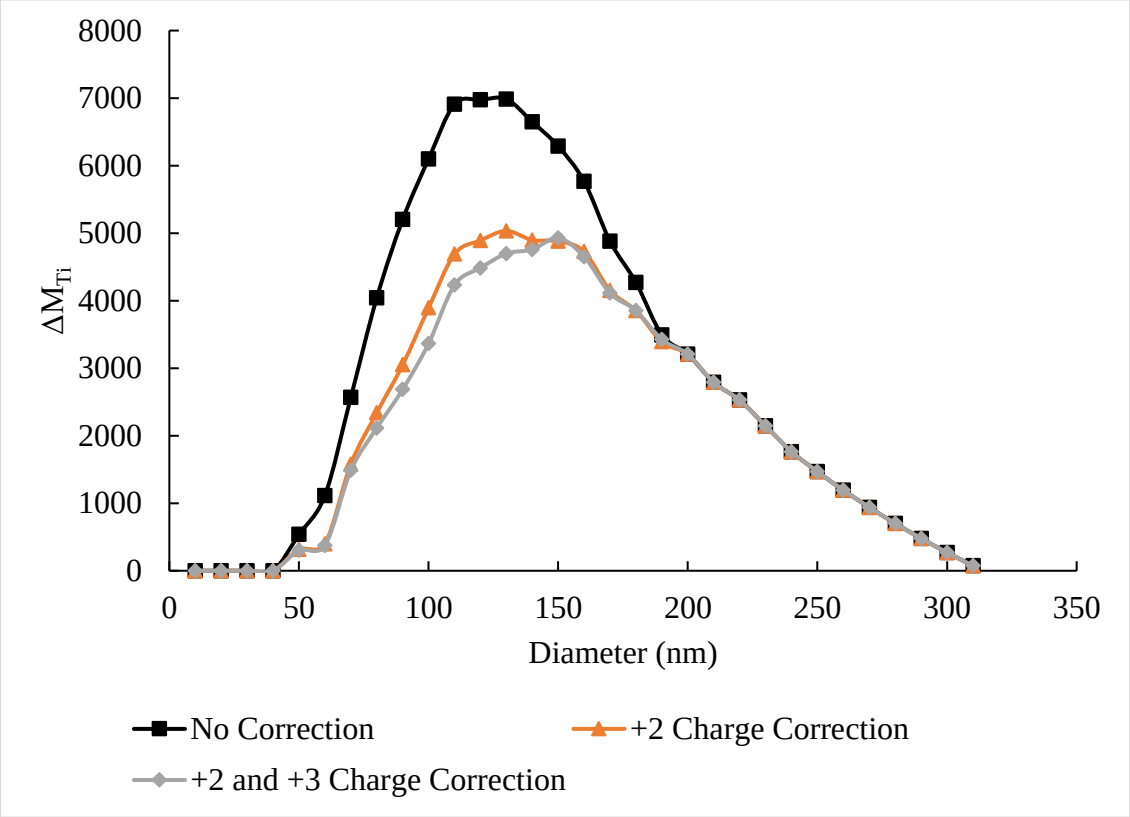


**Figure 3.7**: Titanium uncalibrated mass distribution of Au@$TiO_2$ assuming all particles are singly charged (black squares), correcting for doubly charged particles (orange triangles), and correcting for doubly and triply charged particles (gray diamonds).

The same correction was applied to calculate the calibrated mass distributions of gold and titanium for Au@$TiO_2$ in Figure 3.8. This is a sample with low gold loading, near the limit of detection for the nES-DMA-GED-ICP-MS measurement, at 4.2E-4 mass fraction.

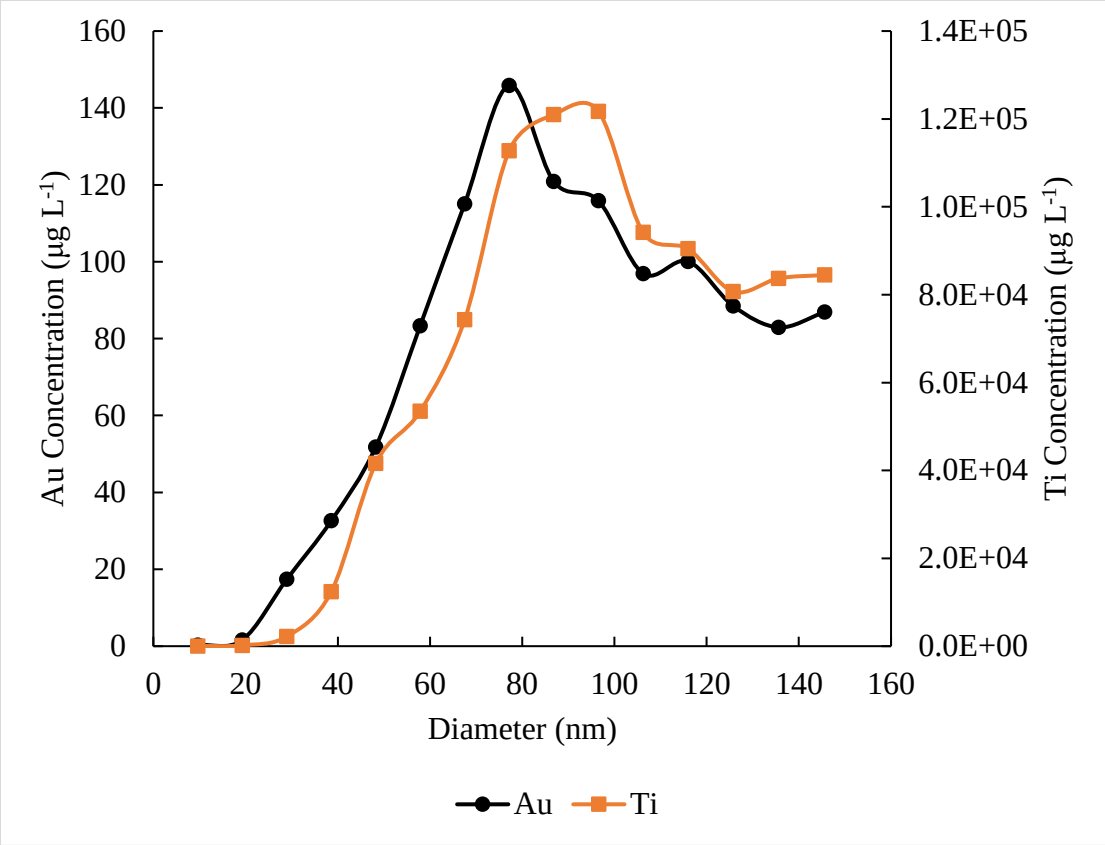


**Figure 3.8**: Calibrated mass distribution of an Au@$TiO_2$ sample with Au mass fraction 4.2E-4 corrected for +2 and +3 charges. The black circles indicate the gold concentration, and the orange squares indicate the titanium concentration.

The percent error for the agreement with the ionic standard calibration curve is presented in Table 3.1. The charge correction reduces the error for the polydisperse Au@$TiO_2$ particles while minimally impacting the monodisperse AuNPs.

**Table 3.1**: Gold and titanium nES-DMA-GED-ICP-MS total mass values from 10 nm – 150 nm with and without the correction for multiple charges. The percent error indicates the difference between the expected $M_T$ from the ionic standard calibration linear fit and the measured $M_T$.

| Sample | Measurement | No Correction | +2 Charge Correction | +2 and +3 Charge Correction |
|---|---|---|---|---|
| $Au@TiO_2$ 5.2E-2 Au Mass Fraction | Gold $M_T$ | 3.8E7 | 2.8E7 | 2.7E7 |
| | Gold % Error | 67 | 25 | 21 |
| | Titanium $M_T$ | 5.9E7 | 4.3E7 | 4.1E7 |
| | Titanium % Error | 139 | 64 | 57 |
| $Au@TiO_2$ 5.1E-3 Au Mass Fraction | Gold $M_T$ | 3.4E6 | 2.7E6 | 2.6E6 |
| | Gold % Error | 64 | 30 | 26 |
| | Titanium $M_T$ | 6.7E7 | 5.0E7 | 4.9E7 |
| | Titanium % Error | 153 | 91 | 85 |
| $Au@TiO_2$ 4.2E-4 Au Mass Fraction | Gold $M_T$ | 3.1E5 | 2.3E5 | 2.3E5 |
| | Gold % Error | 83 | 39 | 34 |
| | Titanium $M_T$ | 6.0E7 | 4.4E7 | 4.3E7 |
| | Titanium % Error | 129 | 69 | 63 |
| QC1 | Gold $M_T$ | 1.1E7 | 1.1E7 | 1.1E7 |
| | Gold % Error | -47 | -47 | -47 |
| QC2 | Gold $M_T$ | 2.3E7 | 2.3E7 | 2.3E7 |
| | Gold % Error | -1 | -2 | -2 |

### *3.4 Discussion*

nES-DMA-GED-ICP-MS is a sensitive technique for the determination of particle size and mass concentration for aerosolized particles. To aerosolize particles, generally nES or nebulization are used. In this case I chose to use nES due to the low sample volume requirements and the monodisperse droplet distribution. Hybrid nanoparticle catalysts are currently produced in small quantities and the catalytically active metal mass fraction tends to be very low. Additionally, the calibration with an ionic standard is easier with monodisperse droplets. The droplet sizes produced by the spray source determine the resulting particle size of dried ionic standard. Spraying ionic standard with monodisperse droplets concentrates most of the mass within a narrow size range that

can be measured rapidly and allows for easy identification of spray issues. However, a limitation of nES is that the solution must be conductive. If a non-volatile salt is used, the mobility diameter of nanoparticles can increase during drying of the droplets (Figure 1.3). Measurement accuracy also requires a stable Taylor cone to produce uniform droplets that contain ideally single particles. The nES requirements are why the measured concentration range of the ionic standard and Au@$TiO_2$ particles was different (x-axes of Figures 3.1 and 3.2). Increasing the concentration of gold or titanium ions increases the conductivity above the range that can be stabilized by this model nES.

After aerosolization, particles are charged and pass through the DMA. The primary parameters for the DMA are the aerosol-to-sheath flow ratio and the voltage. I found a large reduction in signal when the sheath flow was reduced below 10 L $min^{-1}$ likely due to insufficient argon to the plasma. This is also why the response is lower for the ionic standard in Figure 3.3 than Figure 3.1. Without the DMA, less air is exchanged for argon and the ionization efficiency of the plasma is reduced. The voltage range for the DMA is limited by the sheath gas, in this case argon, due to electrical breakdown around 4 kV. This corresponds to a measurable size range from 10 nm – 150 nm. The particles selected by the DMA then pass through the GED which is which is necessary to keep a stable plasma in the ICP-MS. Finally, the particles reach the plasma, are atomized and ionized, and are differentiated by their mass-to-charge, *m/z*, ratio. The detector voltage corresponds to individual ions of a *m/z* and is therefore proportional to the mass concentration from solution. This is a primary advantage of the coupled instrumentation. In general use, the DMA is primarily used with a CPC detector that counts all particles regardless of elemental composition. This means that the DMA-CPC is prone to artifacts from salt particles produced from non-volatile salts in solution. nES-DMA-GED-ICP-MS only quantifies the element of interest,

which broadens the range of salts available to stabilize the nanoparticle solution of interest. Additionally, this saves time on sample cleaning and method development to distinguish peaks of interest from salt artifacts. Conversely, nES-DMA-GED-ICP-MS can be limited by interferences for lighter elements in MS. Optical emission detectors for ICP have less interferences for metals of interest, but the linear concentration ranges are orders of magnitude higher than MS detectors; thus, for applications of bimetallic particles, ICP-MS is the instrument of choice for quantification.

The agreement between the nES-DMA-GED-ICP-MS calculated $M_T$ and the mass concentration for the ionic and nanoparticle standards serve as the primary validation of the method. Ions converted into nanoparticles by the nES behave the same as sprayed nanoparticle solutions. This is the primary evidence I use to suggest the measurement issue is with the Au@$TiO_2$ particles rather than the ionic standard. The low yield for QC1 is likely due to the dimer population, while the current measurement only included the monomer. Efforts were made to determine the cause of the observed discrepancy in response between the Au@$TiO_2$ particles and the ionic standard. One hypothesis was the presence of large Au@$TiO_2$ aggregates that would be undetected by the DMA due to the voltage limitations with argon. Larger particles have a higher probability to have multiple charges than smaller particles, and multiply charged large particles will exit the DMA at the same voltage as singly charged smaller particles. The excess mass may be due to the assumption that I am only detecting singly charged smaller particles. To test this hypothesis, samples were run with and without an impactor that removes aggregates above 250 nm, however no significant difference was detected (data not shown). Next, I noted the agreement between the ionic standard and the AuNPs. Both species traverse the DMA in the form of monodisperse, semi-spherical particles. The Au@$TiO_2$ particles, in contrast, are polydisperse and fractal. It is possible that charging properties are influenced by the particle shape. To test this, I made measurements of

various shaped particles as shown in Figure 3.1. With some variability, the AuNR, AuNC, and Pt@AuNP tended to agree with the ionic standard, so the particle shape does not seem to be the significant variable. The measurements of the ionic standard were generally done in a narrow size range due to the monodisperse droplet generation of the nES. This decision was based on experience with conventional DMA-CPC number concentration measurements. Though no detectable secondary population exists in the number distribution, the same may not be true for the mass distribution measured by nES-DMA-GED-ICP-MS. It is possible that a small number of large diameter particles contain a measurable portion of the total mass of the ionic standard. To test this, I measured the ionic standard over the entire measurable size range (Figure 3.10, supplemental information), from 10 nm – 150 nm, but detected no significant difference from the narrower measurements 16 nm – 40 nm. This suggests the measurement of the peak is sufficient and any larger particles do not represent a significant portion of the total mass. As Figure 3.2 demonstrates, the issue remains when comparing ionic titanium and particle titanium (no gold). This suggests that a feature of $TiO_2$ is the source of the discrepancy. To test whether this is an issue specific to $TiO_2$, measurements of Au were made using $CeO_2$ and $Al_2O_3$ as alternative scaffolds. The Au@$CeO_2$ and Au@$Al_2O_3$ also showed higher nES-DMA-GED-ICP-MS response than the ionic standard (Figure 3.11, supplemental information), indicating that the effect derives from a general characteristic of metal oxide particles. All the metal oxides had broad distributions, but the modes differed, as shown in Figure 3.12 (supplemental information). Another way to test that the issue does not derive from the gold particles was to load larger gold nanoparticles onto titania. Changing the size of the gold did not change the discrepancy between the ionic standard and the Au@$TiO_2$ particles as shown in Figure 3.13 (supplemental information). Finally, instead of focusing on the y-axis of Figure 3.1, it is possible the issue is with the x-axis. If the acid digestion

of Au for the Au@$TiO_2$ particles was incomplete, then the total Au mass (x-axis) would be underestimated, and the black points would shift left from the true value. To test the efficacy of the acid digestion, measurements were repeated at different acid concentrations, for different digestion periods, and the method was validated with QC1 and QC2. The acid concentration and digestion time had no effect on the measurement and the results agreed with in-house characterization by sp-ICP-MS. Despite all these efforts, the nES-DMA-GED-ICP-MS response for the hybrid particles remained several times larger than that measured by the ionic standards and monodisperse nanoparticles.

Some obvious distinctions between the Au@$TiO_2$ and ionic standard are the particle shapes and the size distributions. Both the dried ionic standard particles and the AuNPs are nearly spherical and have a narrow distribution with a half width at half max on the order of 5 nm. The metal oxides used as scaffolds have an agglomerate morphology with primary spherules on the order of 20 nm – 40 nm and have a broad range of mobility sizes with a half width at half max on the order of 60 nm for a 150 nm mass mode diameter. A possible explanation is that the charging efficiency of the metal oxides is higher than the corresponding efficiency for the pure metal but no evidence of this has been previously reported.

The most likely DMA related source of the overcounting of metal oxide particles is multiple charging, as broad distributions have a lot of overlap between various charge states, while monodisperse solutions have more defined separations between charge states. Equation 3.2 demonstrates the inverse relationship between mobility ($Z_p$) and diameter ($D_p$) that is complicated by different charge states ($n$). A large diameter particle with a +2 charge can have the same mobility as a smaller diameter particle with a +1 charge. To investigate this effect, I measured the widest size range possible with the current configuration: 10 nm – 230 nm and used the data to

extrapolate a full nES-DMA-GED-ICP-MS measurement from baseline to baseline (Figure 3.6). This distribution is assumed to be representative of other measurements made at different flow ratios that allow for more sensitive detection by the ICP-MS. The charge correction assumes the largest particles are 310 nm, meaning the mass detected at 310 nm corresponds only to singly charged 310 nm particles. From this starting point, the proportion of doubly and triply charged particles are calculated for each step and are corrected at the smaller diameter that corresponds to a singly charged particle with the same mobility. The correction shown in Figure 3.7 was applied to all other Au@$TiO_2$ measurements. Figure 3.8 shows the mass distribution of an Au@$TiO_2$ sample with this correction, which can be used to determine the relative mass concentration of gold and titanium across the size distribution. The charge correction improved the agreement between the ionic standard and the Au@$TiO_2$ particles but did not completely bridge the difference. Table 3.1 demonstrates the improved agreement between the ionic standards and the Au@$TiO_2$ particles when multiple charging is accounted for. However, the method is still overcounting these particles, as the results in Table 3.1 only include the mass between 10 nm – 150 nm and a significant portion of the total mass is expected at larger sizes. As a result, a percent error of approximately -60% is expected for proper agreement between the ionic standard and Au@$TiO_2$. The measurement is still overcounting by about a factor of 3 – 5, as the measured percent errors range from 21% – 34% for gold and 57% – 85% for titanium.

Solving this analytical challenge provides a tool for more accurate determination of the active nanoparticle distribution across the entire population. This method can detect preferential gold adsorption at different titania sizes, which could be caused by different preparation methods. In Figure 3.8, the mass ratio of gold to titanium is constant across the distribution with small variations likely due to the low concentration of gold. The method still has issues with

overcounting polydisperse metal oxide distributions, but with this known caveat that requires further research, I have developed a universal method for the calibration of nES-DMA-GED-ICP-MS mass distribution measurements. Calibrated mass distributions of monodisperse bimetallic particles between 10 nm – 150 nm can be determined with ionic standards, rather than limiting the method to elements with nanoparticle standards. These measurements may help to explain differences of key particle features, such as catalytic activity, between batches that were intended to be nominally equivalent. Further development can be made on similar systems with experimental designs that incorporate different DMA geometries or a more efficient GED such that the DMA sheath flow could use air instead of argon to sample agglomerates larger than 150 nm. The current development of appropriate calibration procedures allows immediate implementation for examining a broad class of metal supported nanoparticles being used in optical, catalytic, and other applications.

### *3.5 Conclusions*

I developed a simple, universal calibration method for nES-DMA-GED-ICP-MS measurements. The calibration only requires an ionic standard of the element of interest. Linear calibration curves of gold and titanium were determined over a concentration range of an order of magnitude. The measurement can detect multiple elements simultaneously which is advantageous for hybrid particles like those used for catalyst applications. The method had issues with overcounting for specific particles. Several negative results suggest the issue is derived from the DMA and nES and only occurred for metal oxide particles. Multiple charging was hypothesized as one likely source of the overcounting, and the correction for +2 and +3 charged particles improved the agreement between the ionic standard and metal oxide particles. The total mass of

$TiO_2$ was reduced by 34% with the +2 charge correction and 37% with the +2 and +3 charge correction. Replacing the nES with a nebulizer may further improve the agreement, though the additional droplet aggregation from the nebulizer will alter the measured mass distribution. Monodisperse AuNPs agreed with the ionic standard calibration curve and a calibrated mass distribution was determined. Calibrated mass distributions can be a powerful tool for the development of bimetallic nanoparticles. Identifying differences between mass distributions of different particle batches could explain differences in primary characteristics, such as catalytic activity for hybrid catalyst particles. The adsorption method employed here showed a constant gold to titanium ratio, indicating no preferential gold binding by particle size. Alternative methodologies primarily consist of microscopy and are inherently limited in terms of sampling. nES-DMA-GED-ICP-MS is a powerful tool that can rapidly average thousands of particles.

## *3.6 Supplemental Information*

### *3.6.1 The DMA Multiple Charge Correction*

The nES-DMA-GED-ICP-MS data can be corrected for overlapping charge states if a full size distribution is measured and a largest particle is detected.[90] This largest size can be considered all singly charged particles and the charge correction can work iteratively down to smaller sizes. The subscript format $D_{p,i,j,k}$ refers to the mobility diameter of a particle selected by the DMA with mobility $i$, charge $j$, and iteration $k$. For a smaller diameter, the data from the ICP-MS correspond to singly and doubly charged particles exiting the DMA.

$$M_{ICPMS}(Z_{p,1}) = \delta P(D_{p,1,1,1})B^{-1}(D_{p,1,1,1})H(D_{p,1,1,1}) + \delta P\left(D_{p,1,2,1}\right)B^{-1}\left(D_{p,1,2,1}\right)H\left(D_{p,1,2,1}\right) \quad (3.9)$$

Where $H(D_{p,i,j,k}) = \frac{dM(D_{p,i,j,k})}{dD_{p,i,j,k}}$. For the largest diameter, I assume that all of the ICP-MS response corresponds to singly charged particles exiting the DMA.

$$M_{ICPMS}(Z_{p,2}) = \delta P(D_{p,2,1,1}) B^{-1}(D_{p,2,1,1}) H(D_{p,2,1,1}) \quad (3.10)$$

The two mobilities are selected such that $2Z_{p,2} = Z_{p,1}$ and therefore $D_{p,2,1,1} = D_{p,1,2,1}$: a doubly charged particle at the smaller mobility has the same diameter as a singly charged particle at the larger mobility, and $B\left(D_{p,1,2,1}\right) = B\left(D_{p,2,1,1}\right)$. Equation 3.10 can be solved for $H(D_{p,2,1,1})$ which can be substituted into Equation 3.9, because $H\left(D_{p,2,1,1}\right) = H(D_{p,1,2,1})$. The resulting solution is:

$$H(D_{p,1,1}) = \left[M_{cpc}\left(Z_{p,1}\right) - M_{cpc}\left(Z_{p,2}\right) P\left(D_{p,1,2,1}\right) / P\left(D_{p,2,1,1}\right)\right]\left[B\left(D_{p,1,1,1}\right) / \delta P\left(D_{p,1,1,1}\right)\right] \quad (3.11)$$

An additional step is required after the first iteration if $D_{p,1,2,2}$ reaches a size that has been corrected as $D_{p,1,1,1}$ in a previous iteration. For example, if iteration one consists of $D_{p,1,1,1}$ = 150 nm and $D_{p,1,2,1}$ = 240 nm and iteration two consists of $D_{p,1,1,2}$ = 100 nm and $D_{p,1,2,2}$ = 150 nm, a correction will need to be made for $M_{ICPMS}(Z_{p,2})$. Equation 3.9 remains nominally the same, though now it is iteration 2 ($k$ = 2). Equation 3.10 is incorrect for iteration 2 because the ICP-MS response for the larger diameter consists of singly and doubly charged particles.

$$M_{ICPMS}(Z_{p,2,new}) = \delta P(D_{p,2,1,2}) B^{-1}(D_{p,2,1,2}) H(D_{p,2,1,2}) + \delta P(D_{p,1,2,1}) B^{-1}(D_{p,1,2,1}) H(D_{p,1,2,1}) \quad (3.12)$$

Where $\delta P(D_{p,1,2,1}) B^{-1}(D_{p,1,2,1}) H(D_{p,1,2,1})$ has been indirectly solved in a previous iteration.

$$M_{ICPMS}(Z_{p,2,fix}) = M_{ICPMS}(Z_{p,2,new}) - \delta P(D_{p,1,2,1}) B^{-1}(D_{p,1,2,1}) H(D_{p,1,2,1}) \quad (3.13)$$

Which can be solved using Equation 3.9.

$$M_{cpc}(Z_{p,2,new}) - \delta P\left(D_{p,1,2,1}\right) B^{-1}\left(D_{p,1,2,1}\right) H(D_{p,1,2,1}) =$$

$$\delta P\left(D_{p,1,1,1}\right) B^{-1}\left(D_{p,1,1,1}\right) H(D_{p,1,1,1}) \quad (3.14)$$

This leaves an equation analogous to Equation 3.10:

$$M_{cpc}\left(Z_{p,2,fix}\right) = \delta P(D_{p,2,1,2}) B^{-1}(D_{p,2,1,2}) H(D_{p,2,1,2}) \quad (3.15)$$

And Equations 3.9 (iteration 2) and 3.15 can be used to solve for $H(D_{p,1,1,2})$:

$$H(D_{p,1,1,2}) = \left[M_{cpc}\left(Z_{p,1}\right) -\right.$$

$$\left. M_{cpc}\left(Z_{p,2,fix}\right) P\left(D_{p,1,2,2}\right) / P\left(D_{p,2,1,2}\right)\right]\left[B\left(D_{p,1,1,2}\right) / \delta P\left(D_{p,1,1,2}\right)\right] \quad (3.16)$$

*3.6.2 Matrix effects on ionic standards*

nES-DMA-GED-ICP-MS measurements of gold ionic standards were used to calibrate the mass distributions of various particles. The ionic standard was demonstrated to have higher response when dispersed in 378 mg $L^{-1}$ citrate and 0.1% thiourea rather than 378 mg $L^{-1}$ citrate alone (Figure 3.9). This is likely due to ion stabilization with the addition of the chelating agent. Care should be taken to choose a suitable matrix for a given element of interest.

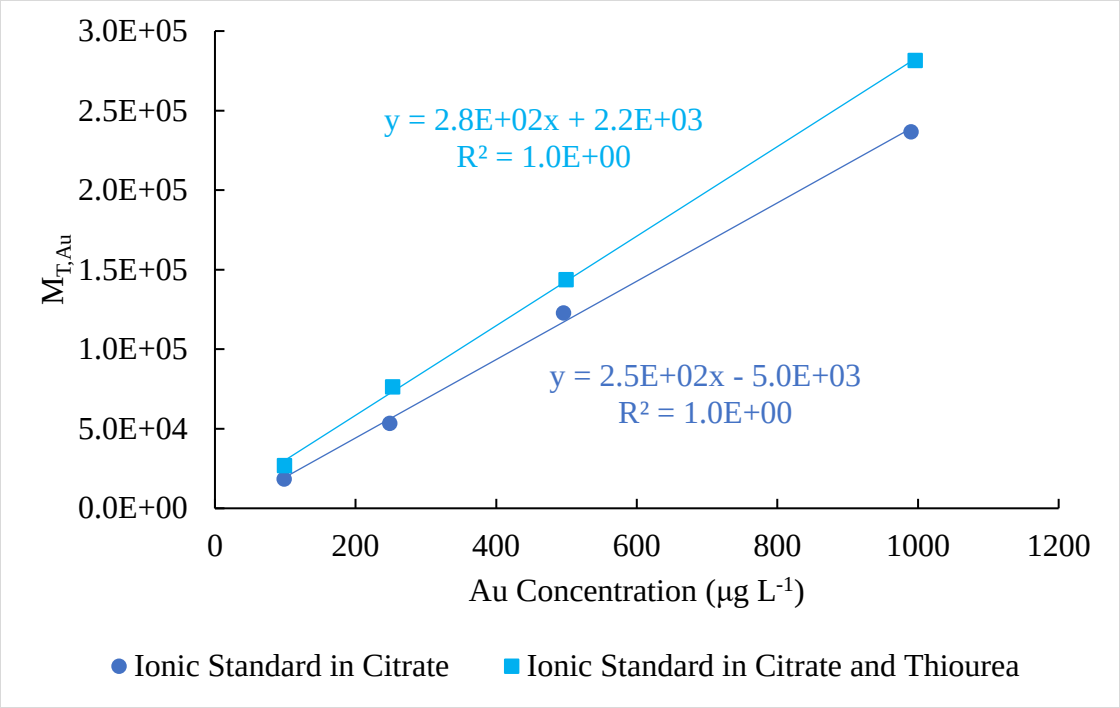


**Figure 3.9**: nES-DMA-GED-ICP-MS measurements of gold ionic standard in 378 mg $L^{-1}$ citrate (dark blue circles) and 378 mg $L^{-1}$ citrate and 0.1% thiourea (light blue squares).

*3.6.3 Ionic standard measurement range*

The measurements of the ionic standards were made of narrow size ranges, generally from 16 nm – 40 nm. This is because the distribution of the ionic standard is determined by the droplet distribution of the spray source, and the droplets that exit the nES spray chamber are monodisperse. It is possible that a few larger droplets contain a significant portion of the total mass, however, and that not counting these larger sizes results in an undercount of the ionic standard. As a result, test measurements were made for the ionic standard from 10 nm – 150 nm. Figure 3.10 shows that no larger diameter mass peak was detected. This suggests that the narrow size measurement is sufficient to quantify the majority of the ionic standard total mass.

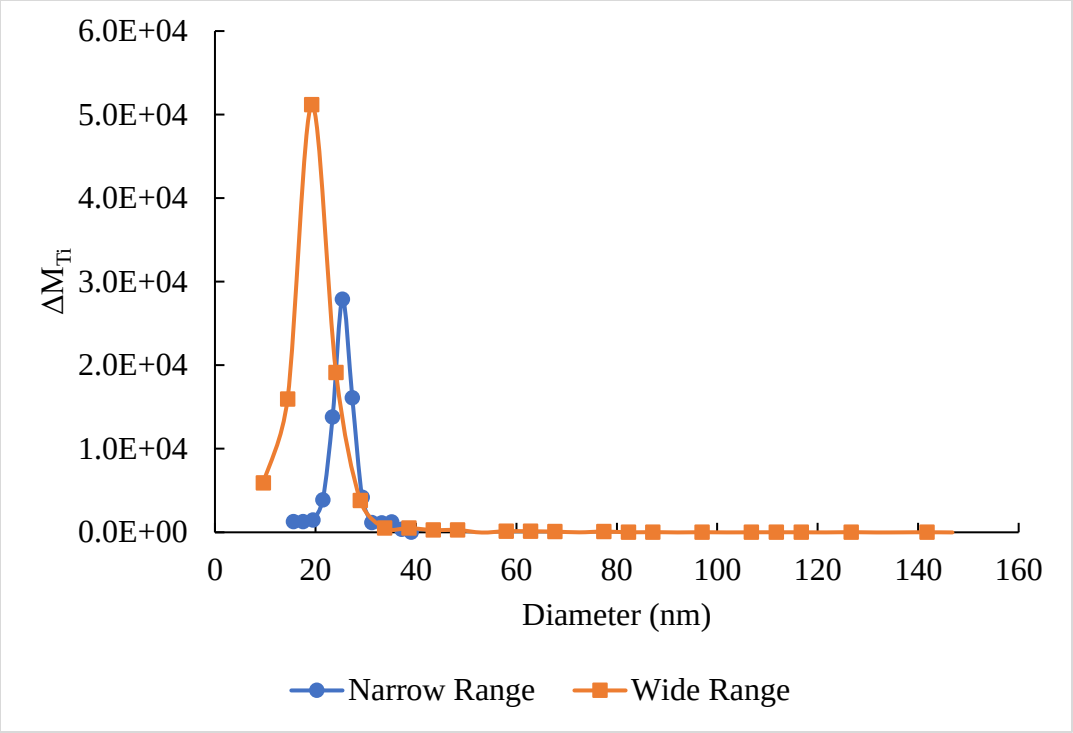


**Figure 3.10**: nES-DMA-GED-ICP-MS measurements of the nominally 1 000 µg $L^{-1}$ titanium ionic standard only at the peak are blue circles, and the full measurable size range are orange squares.

*3.6.4 Metal oxide scaffolds*

To investigate whether the overcounting phenomena is specific to $TiO_2$, the same sample preparation method for Au@$TiO_2$ was used to prepare Au@$CeO_2$ and Au@$Al_2O_3$ samples. Figure 3.11 demonstrates that the overcounting was independent of the specific metal oxide used as a scaffold for the gold. Also, the metal oxides had different mass mode diameters and distributions widths as shown in Figure 3.12.

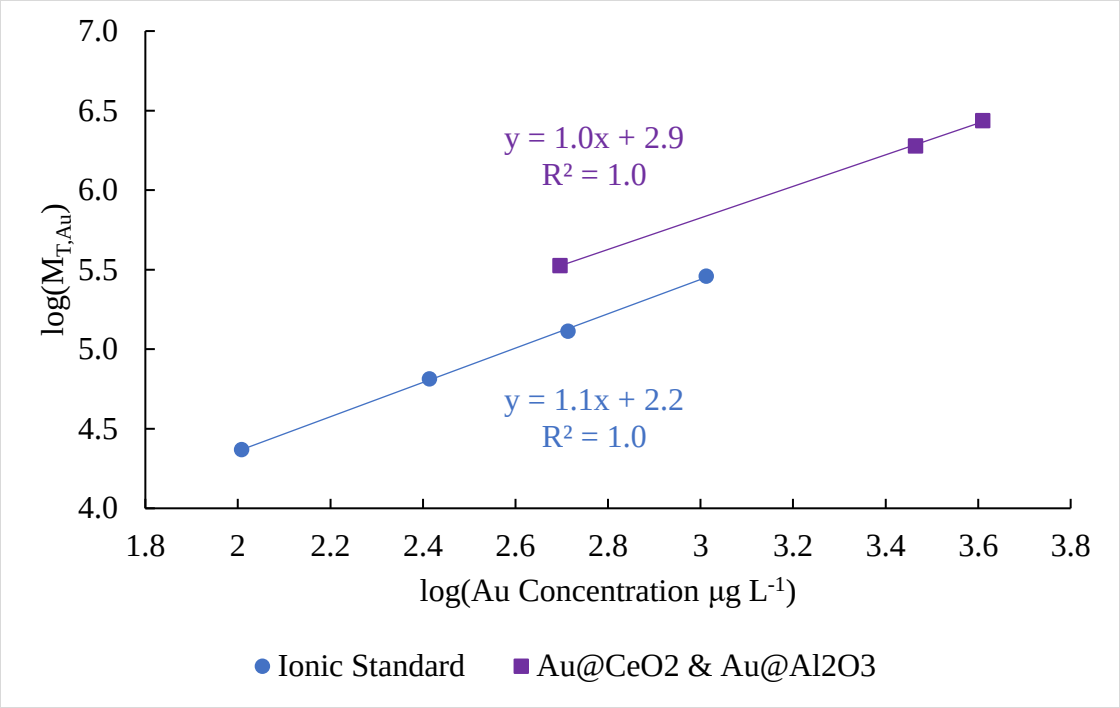


**Figure 3.11**: Gold calibration curve plotting known mass concentration against the summed nES-DMA-GED-ICP-MS response. The axes are scaled logarithmically for convenient comparison to Figure 3.1. The blue circles are the gold ionic standard, and purple squares are Au@$CeO_2$ and Au@$Al_2O_3$.

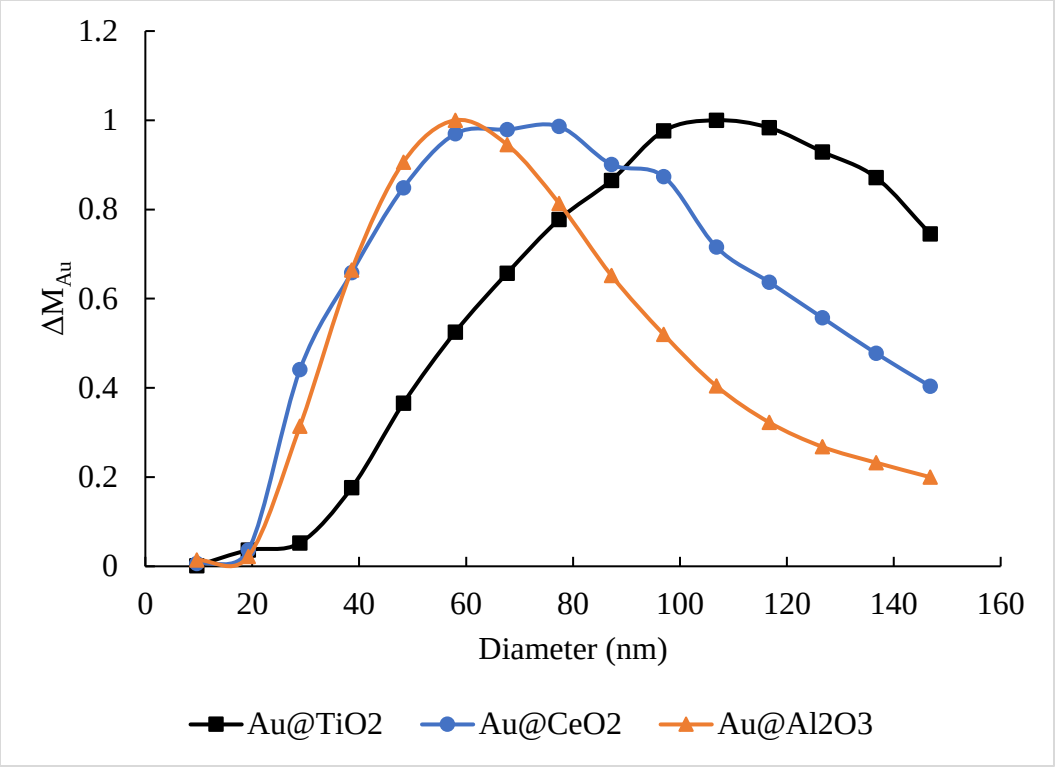


**Figure 3.12**: nES-DMA-GED-ICP-MS measurements of the gold distributions of Au@$TiO_2$ (black squares), Au@$CeO_2$ (blue circles), and Au@$Al_2O_3$ (orange triangles).

*3.6.5 Adsorbed gold nanoparticle size*

The generic method presented in this chapter involves adsorbing 4 nm gold nanoparticles onto the surface of $TiO_2$ particles. To test whether the gold particles were a major contribution to the overcounting problem, measurements were made of Au@$TiO_2$ particles with larger gold particles adsorbed to the $TiO_2$ surface. The overcounting of Au@$TiO_2$ was not corrected by this change (Figure 3.13).

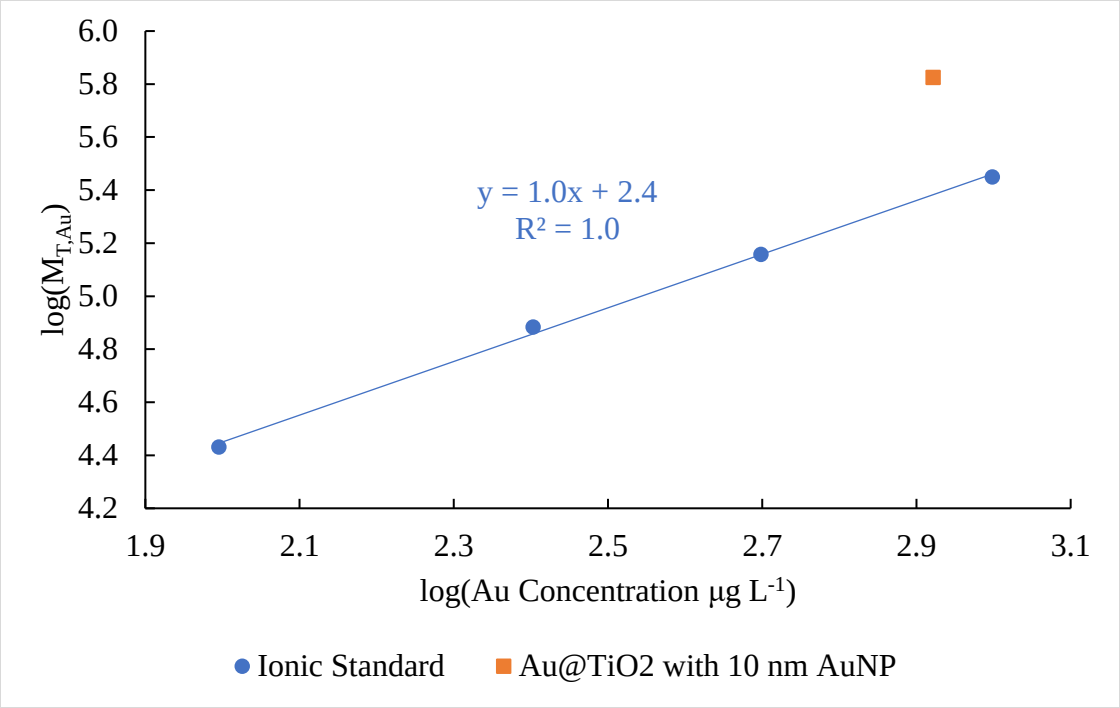


**Figure 3.13**: Gold calibration curve plotting known mass concentration against the summed nES-DMA-GED-ICP-MS response. The axes are scaled logarithmically for convenient comparison to Figure 3.1. The blue circles are the gold ionic standard, and the orange square is Au@$TiO_2$ with 10 nm AuNPs adsorbed.

*3.6.6 Electrospray efficiency*

nES-GED-ICP-MS measurements (no DMA) showed a similar trend to nES-DMA-GED-ICP-MS measurements, with higher ICP-MS response for Au@$TiO_2$ than ionic Au at the same mass concentration. The same was not observed for traditional nebulizer-ICP-MS measurements, which suggests the difference in behavior is derived from the nES or GED. Prior characterization of the GED showed minimal particle loss at 30 nm though some loss is expected for smaller particles.[36] The nES is a likely source of the discrepancy, as other work has shown size dependent transport efficiency associated with nES.[19, 91] nES-GED-ICP-MS measurements were made of gold particles with various mobility diameters at the same mass concentration. Some correlation was observed, where increased diameter was related to increased response from the ICP-MS,

though there were several outliers (AuNC, LGCQC5050, AuNR 20 nm width and 55 nm length). The measurements were made at a flow rate of 0.5 L $min^{-1}$ at a nominal gold concentration of 1 000 µg $L^{-1}$.

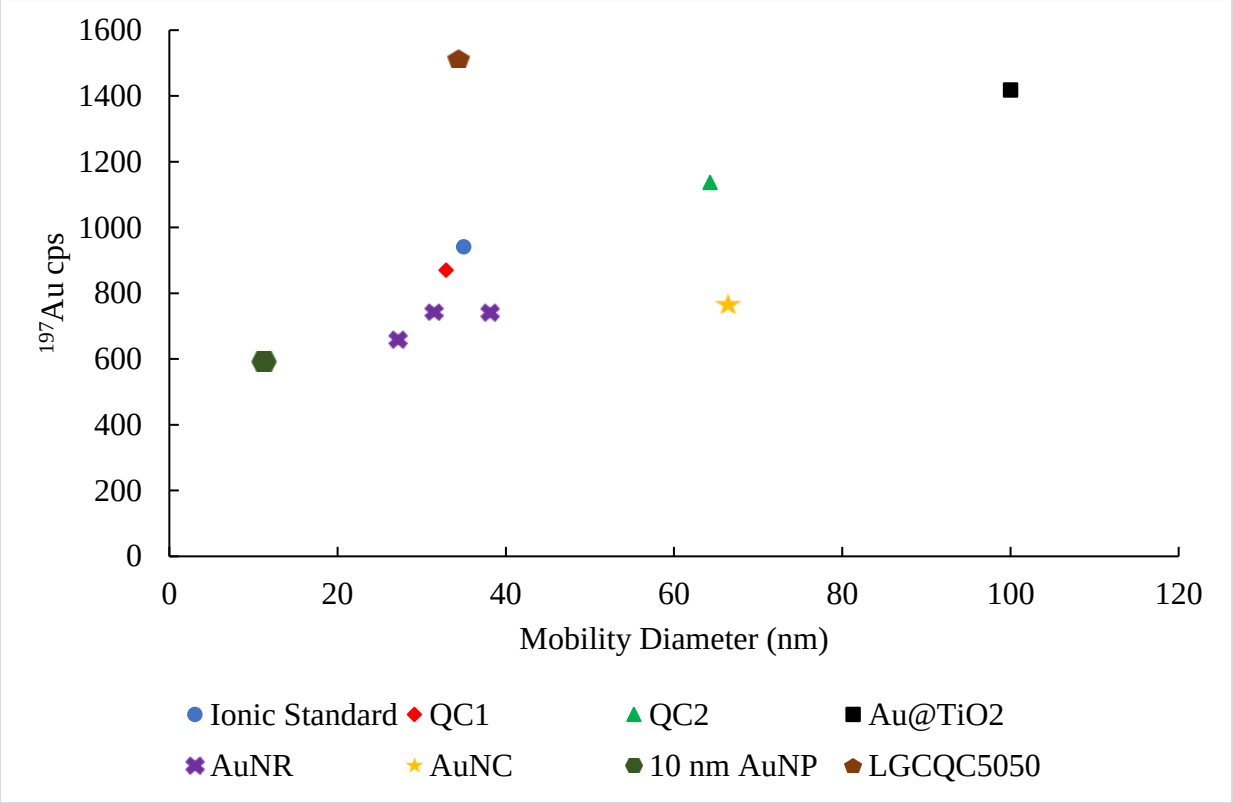


**Figure 3.14**: nES-GED-ICP-MS response for various gold nanoparticles at 1 000 ug $L^{-1}$. The blue circle is the ionic standard, the red diamond is QC1, the light green triangle is QC2, the black square is Au@$TiO_2$, the purple X are AuNR, the yellow star is AuNC, the dark green hexagon is 10 nm AuNPs, and the brown pentagon is LGCQC5050. The flow rate to the ICP-MS was 0.5 L $min^{-1}$.

# Chapter 4: Accurate Nanoparticle Size Determination using Mobility Measurements in the Step and Scan Voltage Modes

## *4.1 Introduction*

Nanoparticle size is an important characteristic that determines optical properties and transport properties, such as mobility, diffusion, friction, coagulation, and charging. It is important to be able to accurately measure the size of particles, which is why nanoparticle size standards are relied on heavily in industry and research. Many instruments are available for certification of new nanoparticle size standards, but the most common tend to be microscopy-based due to the intuitive, visual representation of the data. Generally, the easiest calibration procedure is to compare a size standard with a particle of unknown size on a single grid. This approach assumes that the uncertainty of the standard and the unknown are same and sometimes ignores key measurement uncertainties associated with the instrument. Often a few measurements of a primary standard serve as calibration and then the mean and standard deviation of the unknown serve as the certified value and uncertainty. Well-characterized methods, such as light scattering[92], the National Institute of Standards and Technology (NIST) calibrated Atomic Force Microscope[93], and Electro-Gravitational Aerosol Balance[94], where the key uncertainty terms have been calculated, can be used for primary certification. It is also ideal for a method to be traceable, where a direct connection is made to an SI unit: in this case the meter.

Several nanoparticle size standards are available for use. There are monodisperse polystyrene spheres traceable to SI units for nominal sizes of 60 nm and 100 nm. Within the size range from 10 nm to 100 nm, there are nanoparticle calibration particles available from vendors made of materials including polystyrene, silica, gold, and silver. Gold nanoparticles (AuNPs) are of special interest because of their use in biomedical applications due to their biocompatibility and

optical properties.[95] Reference (citrate stabilized) AuNPs calibrants with nominal sizes of 10 nm (RM 8011), 30 nm (RM 8012), and 60 nm (RM 8013) and with coefficients of variance (CV, one standard deviation divided by the mean) of 3% – 4% were issued by NIST in 2007. The mean particle diameter was determined by differential mobility analysis (DMAS), scanning electron microscopy (SEM), transmission electron microscopy (TEM), atomic force microscopy (AFM), dynamic light scattering (DLS), and small angle X-ray scattering (SAXS), and the values obtained by each method were reported on the certificate. These values were not traceable to SI units, nor was a quantitative uncertainty statement included. Even with these limitations, the 30 nm and 60 nm particles were in high demand and the supply was exhausted. New candidate reference materials produced by citrate reduction of a gold chloride solution are being characterized by a variety of measurements including DMAS. In this chapter, I examine mobility measurements conducted on these candidate reference material particles in step voltage mode, the calibration of DMAS via 60 nm SRM 1964, and a quantitative uncertainty analysis.

DMAS is an aerosol sizing technique that has been used extensively for particle measurements related to combustion[96], climate[97], and particle engineering. DMAS has also been employed in particle size standards measurements. It has been used to certify NIST standard reference material (SRM) 1963[98], NIST SRM 1963a, and NIST SRM 1964.[56] DMAS is not generally used as a primary calibration technique because of the uncertainty in the flow dynamics where the aerosol inlet flow meets the sheath flow. Additionally, there may be minor fringe effects on the electric field used for separation. DMAS is more commonly used as a secondary calibration technique, where the known size of a primary standard is used for calibration and an unknown particle is measured traceable to the primary standard. DMAS is suited for these measurements because of the following characteristics: it is very reproducible, it measures a number distribution,

it measures the size of many particles rapidly, the size resolution is easily controllable, and it has a well-defined transfer function.

The differential mobility analyzer (DMA) is often run in one of two modes: step voltage or scan voltage mode. The step voltage mode steps through the voltage range, spending a specified amount of time at each voltage. Each voltage corresponds to a specific mobility (which is related to the particle diameter) and the particles exiting the DMA are counted by a condensation particle counter (CPC). Historically the DMA has been used in the step voltage mode because it is straightforward to determine the particle diameter from measurements of number concentration vs. voltage. This is the method that has been used in the previous certification of NIST SRMs for particle size. However, the step voltage mode is not suited to all aerosols. Some aerosol size distributions change rapidly, on the order of the amount of time needed to make a step mode measurement. Due to this limitation, the scan voltage mode was developed to allow for rapid measurements.[17] The scan voltage mode of the instrumentation is generally referred to as the scanning mobility particle sizer (SMPS) and continuously changes the voltage during a measurement. The SMPS takes advantage of the inherent dead time in DMAS: the time it takes the aerosol to travel from the entrance of the DMA to the detector is wasted for each step of a step voltage mode measurement. Instead, if this dead time is well known, the voltage can be changed before the first aerosol cluster reaches the detector. This is the basis of the SMPS. For the SMPS model used here, the voltage is varied with an exponential ramp from an initial, non-zero voltage to a final voltage (the voltage scan rate increases with time), a well-known time-constant defines the transport from the entrance of the DMA to the detector, and each detector signal is thereby related to a particular diameter. This significantly reduces the measurement time for broad size distributions, such as the full range of the long DMA: 10 nm – 1 000 nm. Using the step voltage

mode, a measurement would generally take 30 min – 45 min, while with the SMPS it can be completed in 30 s. Over time the SMPS became ubiquitous due to its commercial availability and ease of use. However, the step voltage mode is still the operational mode of choice for size certification measurements.

The accuracy of the SMPS mobility diameter measurements is of interest. Initial investigations with the SMPS indicated that the size distributions of 23.2 nm dried ammonium sulfate aerosol with a CV of 1% measured with an 80 s scan time were nominally the same as the measurement in step voltage mode, but no data have been presented for measurements of size standards.[17] Here I investigate a simple application of the SMPS: the measurement of the number average diameter of a narrow size distribution. In this case, the effects of multiple charging and size dependent losses are minor. I compare the mean diameter obtained by both methods when I use 60 nm SRM 1964 to calibrate both configurations. Additionally, I independently calibrated the SMPS measurements using a direct measurement of the sheath flow. I investigate the effects of scan time and the delay time on the SMPS measurement. I compare the step mode and SMPS using uncalibrated measurements with identical hardware, making alternate measurements within a single day. One objective is to assess whether the SMPS can be used for future certifications. Additionally, I can assess the accuracy of using DMAS as a primary size measurement.

## *4.2 Materials and Method*

### *4.2.1 Chemicals*

Nominally 30 nm AuNPs NIST candidate reference material QC1, nominally 60 nm AuNPs NIST candidate QC2, nominally 100 nm polystyrene latex (PSL) NIST SRM 1963a,

nominally 60 nm PSL NIST SRM 1964, and 18.2 MΩ·cm deionized water (Model 2121AL, Aqua Solutions, Jasper, GA, USA) were used. Ammonium acetate (>99.99%) was purchased from Sigma-Aldrich (St. Louis, MO, USA), and nominally 60 nm AuNPs were purchased from Ted Pella (Redding, CA, USA).

Both AuNP candidate reference materials (QC1 and QC2) are currently in production at NIST, and therefore any value assignments provided in this work are to be considered preliminary in nature. The source materials were prepared to NIST specifications by BBI Solutions (Crumlin, UK).

*4.2.2 Sample Preparation*

AuNP solutions were prepared by centrifuging the stock (1 mL) in a lo-bind microcentrifuge tube (Eppendorf, Hamburg, Germany) at 3 900 rcf for 12 min. The supernatant (950 μL) was removed and 300 μL of 0.15 g $L^{-1}$ ammonium acetate was added. PSL solutions were prepared by adding the stock (100 μL) to $H_2O$ (1 mL) after bath sonication for 5 min and filtering the diluted sample (0.2 μm, Whatman, Maidstone, UK). The filtered solution (50 μL) was added to 450 μL of 0.15 g $L^{-1}$ ammonium acetate.

*4.2.3 Step Voltage*

The system used here has been described previously (Figure 1.7).[86] Briefly, DMAS consists of a spray source, a DMA, and a particle counter. In this case a nano electrospray source (nES, Model 3480, TSI, Shoreview, MN, USA) was used. The long DMA (Model 3081, TSI) was used for measurements of QC1, QC2, and SRM 1964. The nano DMA (Model 3085, TSI) was used for

measurements of salt particles produced by the nES. The electrospray was set to 2.5 kV – 3.5 kV with a resulting current of 150 nA – 250 nA. The pressurized sample cell was set to 26 kPa (3.7 psi). Particles were sprayed through a 40 μm inner diameter fused silica capillary. The aerosol flow rate was 1 L $min^{-1}$ air and charged with a Po-210 alpha-emitter (model P-2042, TSI). The voltage for the DMA was set by a Bertan power supply (Model 205B-10R, Spellman, Hauppauge, NY, USA) controlled by a custom LabVIEW code (National Instruments, Austin, TX, USA). The 20 L $min^{-1}$ sheath flow was set by an independent mass flow controller (not the SMPS mass flow controller). The temperature and pressure were measured by a TSI flow meter (Model 4043, TSI) in-line with the excess flow. The particles were detected by a condensation particle counter (Model 3776, TSI).

*4.2.4 Differential Mobility Analysis*

The mobility, $Z_p$, is determined by the balance of the drag force and the electrostatic force.

$$Z_p = \frac{neC_c(D_p)}{3\pi\mu D_p} \tag{4.1}$$

$n$ is the number of charges, $e$ is the elementary charge, $C_c$ is the Cunningham slip correction (described below), $\mu$ is the viscosity of the gas, and $D_p$ is the mobility diameter. The expression for the peak mobility of a particle exiting the DMA used here has been determined previously.[11]

$$Z_p = \frac{q_{sh}\ln(r_2/r_1)}{2\pi LV} \tag{4.2}$$

$q_{sh}$ is the sheath flow rate, $r_2$ is the outer radius, $r_1$ is the inner radius, $L$ is the length of the DMA from entrance slit to exit slit, and $V$ is the voltage of the inner electrode. Equations 4.1 and 4.2 are combined to determine the mobility diameter from DMAS measurements.

$$\frac{D_p}{C_c(D_p)} = \frac{2neLV}{3\mu q_{sh} ln\,(r_2/r_1)} \tag{4.3}$$

DMAS measures the number concentration of an aerosol at the detector (CPC) post transport through the DMA. In the step mode, this measurement, $N_{cpc}$, is a convolution of the size distribution of the aerosol before the DMA, $F(Z_p)$, and the transfer function through the DMA, $\Omega(Z_p)$.

$$N_{cpc}(V) = \int \Omega(Z_p, V) F(Z_p) dZ_p \tag{4.4}$$

Where $F(Z_p) = \frac{dN}{dZp}$ and d$N$ is the number concentration of singly charged with particles with diameters between $Z_p$ and $Z_p$ + d$Z_p$. Expressing Equation 4.4 in terms of the size distribution for all the particles entering the DMA, $G(D_p) = {}^{dN}/_{dD_p}$, one obtains the following equation including a term for particle charging, $P(D_p)$.

$$N_{cpc} = \int \Omega(Z_p V) G(D_p(Z_p)) P(D_p(Z_p)) \left|\frac{dD_p}{dZ_p}\right| dZ_p \tag{4.5}$$

Making a standard approximation that all the quantities except the transfer function change slowly with diameter one obtains the following expression for the diameter size distribution.

$$G(D_p) = \left[N_{CPC}(V) \left|\frac{C_c'(D_p)}{C_c(D_p)} - \frac{1}{D_p}\right|\right] / \left[(\delta)\left(p(D_p)\right)\right] \tag{4.6}$$

$\frac{C_c'(D_p)}{C_c(D_p)} - \frac{1}{D_p}$ is proportional to the term $\left|\frac{dD_p}{dZ_p}\right|$ and δ is equal to the aerosol flow divided by the sheath flow. $C_c$ is the Cunningham slip correction.

$$C_c = 1 + K_n(\alpha + \beta(\exp(-\gamma/K_n))) \tag{4.7}$$

$\alpha$, $\beta$, and $\gamma$ are empirical constants for the slip correction. I used the values 1.165, 0.483, and 0.997[87], but the SMPS software uses 1.142, 0.558, and 0.999. $K_n$ is the Knudsen number, $2\lambda/D_p$, and λ is the mean free path of the gas.

An alternative form for the size distribution is in terms of the logarithmic derivative $G1\left(D_p(Z_p)\right)$:

$$G1(D_p) = \frac{dN(D_p)}{dlogD_p} = \frac{dN(D_p)}{dD_p}(D_p)(\ln(10)) \tag{4.8}$$

The number average diameter was calculated using the following equation:

$$\overline{D}_p = \frac{\sum i\left[(D_{p,i})\left(\frac{dN_i}{dlogD_{p,i}}\right)(dlog_{Dp,i})\right]}{\sum i\left[\left(\frac{dN_i}{dlogD_{p,i}}\right)(dlogD_{p,i})\right]} \tag{4.9}$$

Nonvolatile salts needed for colloidal stability will coat the analyte nanoparticles during droplet evaporation post electrospray (Figure 1.3). This increase in size was corrected to determine the size of the analyte particles in solution by measuring the size of salt particles produced by droplets that do not contain gold nanoparticles.

$$\overline{D}_{p,c} = \sqrt[3]{\overline{D}_p^3 - \overline{D}_{salt}^3} \tag{4.10}$$

$\overline{D}_{salt}$ was 11.94 nm for QC1 and 12.44 nm for QC2 based on these dilution conditions.

### *4.2.5 Particle Standard Calibration*

The mode of the number distribution of SRM 1964, PSL particles with a certified diameter of 60.39 nm and a combined standard uncertainty of 0.31 nm, was used to calibrate the DMA for

step mode and SMPS. The calibration was based on the direct proportionality between mobility and flow as given in Equation 4.2:

$$q_{cal} = q_{sh} \frac{Z_{p,theoretical}}{Z_{p,experimental}} \tag{4.11}$$

$q_{cal}$ is the calibrated sheath flow, $q_{sh}$ is the experimental sheath flow, $Z_{p,theoretical}$ is the expected mobility of the calibrant, and $Z_{p,experimental}$ is the measured mobility of the calibrant. The quantity $q_{cal}$ is the value of the sheath flow that gives the correct mobility. Measurements of the mobility distribution (voltage vs. number concentration) were sufficient to determine the mode and calibrate the sheath flow in previous studies with alternative size standards (for example, SRM 1964 and SRM 1963a certified by SRM 1963). However, in this case it was found that the mode of the mobility distribution of SRM 1964 corresponded to a size about 0.2 nm smaller than the certified mode in the diameter distribution. As a result, a correction was applied to shift the mode of the diameter distribution to the certified value. Two values of $q_{cal}$ were used to calculate two mode diameters $D_{p,1}$ and $D_{p,2}$, and then the correct sheath flow, $q_{cal,correct}$ was calculated using Equation 4.12.

$$q_{cal,correct} = q_{cal,1} + \left(\frac{q_{cal,2} - q_{cal,1}}{D_{p,2} - D_{p,1}}\right)(60.39 - D_{p,1}) \tag{4.12}$$

*4.2.6 Experimental Design*

The approach was to measure the full size distribution of four samples from a combined source on a single day. Calibration measurements (SRM 1964) were made on four samples to allow the determination of the peak voltage. This did not require a full size distribution

measurement. The measurement sequence is shown in Table 4.1. The repeat calibrant measurements were made to correct for drift over the 15 min measurement time. The same measurement sequence was repeated on two other days to assess the effect of day-to-day variability on the average particle size. This process was used for both QC1 (nominal 30 nm AuNPs) and QC2 (nominal 60 nm). This method was followed for step measurements and independently for SMPS measurements on a difference series of three days.

**Table 4.1**: The experimental design of the step voltage and SMPS measurements of the AuNPs (Samples A – L).

| Test Day | Test ID | Calibrant Used |
|---|---|---|
| Day 1 | SRM 1964 1 | - |
| | Sample A | SRM 1964 1 |
| | Sample B | SRM 1964 2 |
| | SRM 1964 2 | - |
| | SRM 1964 3 | - |
| | Sample C | SRM 1964 3 |
| | Sample D | SRM 1964 4 |
| | SRM 1964 4 | - |
| Day 2 | SRM 1964 5 | - |
| | Sample E | SRM 1964 5 |
| | Sample F | SRM 1964 6 |
| | SRM 1964 6 | - |
| | SRM 1964 7 | - |
| | Sample G | SRM 1964 7 |
| | Sample H | SRM 1964 8 |
| | SRM 1964 8 | - |
| Day 3 | SRM 1964 9 | - |
| | Sample I | SRM 1964 9 |
| | Sample J | SRM 1964 10 |
| | SRM 1964 10 | - |
| | SRM 1964 11 | - |
| | Sample K | SRM 1964 11 |
| | Sample L | SRM 1964 12 |
| | SRM 1964 12 | - |

*4.2.7 Uncertainty Analysis*

An uncertainty analysis includes a component that can be calculated by statistical means such as one standard deviation of a set of measurements and a second component that is calculated by other means such as uncertainties assigned to reference data. The first is considered type A and the second type B. Only the type A uncertainty is presented for the SMPS measurements as a quantitative uncertainty analysis has not been determined.

The type A uncertainty was determined by analyzing the means and standard errors of three days' replicate measurements using the DerSimonian-Laird approach.[99] This is a random effects model that expresses each measured value $D_{p,j}$ as an additive superposition of three elements:

$$D_{p,j} = \psi + \theta_j + \varepsilon_j \tag{4.13}$$

where $\psi$ is the measurand (true value of $D_p$), $\varepsilon_j$, refers to the measurement error and $\theta_j$ to the day-to-day error. The variance of the day-to-day effect is $\tau^2$. The quantity $\varepsilon_j$ is assumed to be an independent random variable with variance $\sigma_j^2$, which is estimated as the variance of the four diameter measurements on day $j$, $u_j^2$. The estimated value of the mean diameter, $\widehat{D}_{p,avg}$, is given by the following expression:

$$\widehat{D}_{p,avg} = \sum_{j=1}^{3} w_j \overline{D}_{p,j} / \sum_{j=1}^{3} w_j \tag{4.14}$$

$\overline{D}_{p,j}$ is the average of the four diameter measurements on the j$^{th}$ day and with weights given by:

$$w_j = 1/(\tau^2 + \sigma_j^2) \tag{4.15}$$

Since the value of $\tau$ is not known, it is replaced with a method of moments estimate provided Equation 4.16 gives a non-negative result:

$$\hat{\tau}^2 = \frac{(Q-n+1)}{\sum_{j=1}^{3} u_j^{-2} - \sum_{j=1}^{3} u_j^{-4} / \sum_{j=1}^{3} u_j^{-2}} \tag{4.16}$$

$$Q = \sum_{j=1}^{3} u_j^{-2} \left(\overline{D}_{p,j} - \widehat{D}_{p,avg}\right)^2 \tag{4.17}$$

If this results in a negative value of $\hat{\tau}^2$, one sets $\hat{\tau}^2 = 0$. The initial estimate of $\widehat{D}_{p,avg}$ was taken to be the average of all twelve diameter measurements. Successive iterations of this calculation were made if the value of $\widehat{D}_{p,avg}$ computed via Equation 4.14 differed from the initial estimate. The standard uncertainty in the value of $\widehat{D}_{p,avg}$ is given by:[100]

$$u_{\widehat{D}_{p,avg}} = \sqrt{1/\sum_{j=1}^{3} w_j} \tag{4.18}$$

The number of degrees of freedom is 2. The results are summarized in Table 4.2.

**Table 4.2:** The type A uncertainties for the step voltage mode and SMPS measurements.

| | | $D_{p,avg}$, nm | $u_{D_{p,avg}}$, nm | $u_r$, % |
|---|---|---|---|---|
| Step Voltage Particle Calibration | QC1 | 33.42 | 0.105 | 0.314 |
| | QC2 | 64.40 | 0.102 | 0.159 |
| SMPS Particle Calibration | QC1 | 33.70 | 0.050 | 0.149 |
| | QC2 | 64.48 | 0.234 | 0.363 |
| SMPS DryCal Calibration | QC1 | 33.03 | 0.155 | 0.470 |
| | QC2 | 63.68 | 0.402 | 0.632 |

Type B uncertainties are generally systematic and are characterized by analyzing components of the measurement system. The major contributors to the type B uncertainty are given

in Table 4.3. The type B uncertainty for the particle standard calibration method is derived from Equation 4.19.[56]

$$D_p = \frac{C_c}{C_{c,s}} \frac{V}{V_s} D_{p,s} \tag{4.19}$$

$D_p$ is the particle diameter, $C_c$ is the slip correction, $V$ is the voltage, and the additional "$s$" subscript refers to the size standard, SRM 1964. The final form of the uncertainty expression is given in Equation 4.20. This expression is derived by first computing the differential d$D_p$ as a function of the differentials of the variables $D_{p,s}$, d$C$, d$C_s$ $V$, and $V_s$,. Then the slip correction is expressed as a function of $T$, $P$, $D_p$, and the slip correction factor $A$.[56] The variance of the sum of the differentials is the sum of the individual variances except for the terms $A$ and $A_s$, which are correlated. For example, if the calibration diameter and the unknown diameter are the same, then the measurement of the unknown would have no error. I estimate the effect of the entire Cunningham slip correction, $C_c = 1 + K_n(A)$ by computing an unknown diameter based on a fixed calibration diameter (a fixed voltage ratio) but with two different choices of the slip correction.

$$u_r^2(D_p) = \left(\frac{f_1(C_{c,s})}{f_1(C_c)} u_r(D_{p,s})\right)^2 + \left(\frac{1}{f_1(C_c)} u_r(V)\right)^2 + \left(\frac{1}{f_1(C_c)} u_r(V_s)\right)^2 +$$

$$\left(u_r(A, As)\right)^2 + \left(\frac{f_2(C_c) - f_2(C_{c,s})}{f_1(C_c)} \left(2 - \frac{T}{T + 110.4\ K}\right) u_r(T)\right)^2 + \left(\frac{f_2(C_c) - f_2(C_{c,s})}{f_1(C_c)} u_r(P)\right)^2 \tag{4.20}$$

$u_r$ refers to the relative standard uncertainty (percent) of the various terms, $f_1(C_c) = \frac{2C_c - 1}{C_c}$, $f_2(C_c) = \frac{C_c - 1}{C_c}$, $T$ is the temperature in Kelvin, and $A$ is a portion of the slip correction as defined in Equation 4.21.

$$A = \alpha + \beta \exp\left(\frac{-\gamma d_p}{2\lambda}\right) \quad (4.21)$$

$\alpha$, $\beta$, and $\gamma$ are empirical constants for the slip correction and $\lambda$ is the mean free path of the gas. The two sets of coefficients for $\alpha$, $\beta$, and $\gamma$ listed above were used to calibrate and solve for the mean diameter of a data set. The difference between the two means was used to approximate $u_r(A)$. Then the type A and type B uncertainty were combined in quadrature and a coverage factor of 2.2 was applied to obtain the 95% confidence interval as seen in Table 4.5. This is the final uncertainty for the aerosol particle.

The uncertainty for the particle in solution included the additional terms for the salt particles.

$$\frac{u_r(D_{p,c})}{D_{p,c}} = \left[\left(\frac{D_p^2}{D_{p,c}^2}\right)^2 \left(\frac{u_r(D_p)}{D_{p,c}^2}\right)^2 + \left(\frac{D_{salt}^2}{D_{p,c}^2}\right)^2 \left(\frac{u_r(D_{salt})}{D_{p,c}}\right)^2\right]^{1/2} \quad (4.22)$$

4.2.7.1 Voltage

Two power supplies were used to apply the voltage to the DMA inner rod, one for the step voltage measurements and one for the SMPS. The power supplies were independently calibrated by connecting the power supply to a Spellman HUD-100-1 precision resistor ladder and an Agilent 34401A 6.5 digit digital multimeter. The calibration of the step voltage power supply corrected the voltage to within 0.14%, combining in quadrature the uncertainty of the multimeter, the resistor ladder, and the calibration. The calibration of the SMPS power supply was conducted using Firmware commands within the AIM software and corrected the voltage to within 0.05%.

4.2.7.2 Pressure

The barometric pressure was measured using a TSI Model 4043 mass flow meter. The stated pressure uncertainty was 1 kPa with traceability to NIST. Additional calibration measurements were made at NIST in the Ultrasonic Interferometer Manometer Lab by comparing the mass flow meter pressure reading to a calibrated Ruska model 6200 pressure gauge at ambient pressure. The accuracy of the pressure gauge is better than 0.05% of the reading or 0.05 kPa at atmospheric pressure. The flow meter read between 100.2 kPa – 100.3 kPa while the pressure gauge read 100.33 kPa. I estimate that TSI flow meter measures within ± 0.2 kPa of the true pressure. During the step voltage experiments, the pressure was measured in the excess aerosol tube after the DMA. The pressure within the characterization region of the DMA was determined to be 1.8 ± 0.1 kPa higher than the TSI meter reading due to internal pressure drops. This pressure was added to the pressure measured during the experiment. The pressure has a relative combined standard uncertainty of 0.22% near ambient pressure. The measurements were made before and after a size distribution measurement was made, and the average of the two values was used in later calculations. For the SMPS measurements, a single measurement of the pressure is made at the start of the size distribution scan.

4.2.7.3 Temperature

The temperature was measured with TSI Model 4043 mass flow meter. The stated temperature uncertainty was 1 °C with traceability to NIST. Additional calibration measurements were made at the NIST Primary Flow Calibration Facility. The temperature was measured to a standard uncertainty of ± 0.02 K both before the flow meter and after. The temperature increased from 297.1 K – 298.0 K as the 160 $cm^3$ $s^{-1}$ flow passed through the flow meter, which recorded a

reading of 297.4 K. I estimate that the true value of the gas temperature is within ± 1.0 K of the value measured with the TSI instrument. Assuming a uniform rectangular distribution for the probability distribution of the temperature, I obtained a standard uncertainty in *T* equal to $1/\sqrt{3} = 0.58$ K or a relative standard uncertainty of 0.20% based on a gas temperature of 296.15 K. The drift in temperature during a voltage scan, less than 0.1 K, was small compared to the uncertainty from the calibration and was neglected. For step voltage measurements, the temperature was measured at the excess flow outlet of the DMA. The measurements were made before and after a size distribution measurement was made, and the average of the two values was used in later calculations. For the SMPS measurements, a single measurement of the temperature is made at the start of the size distribution scan.

**Table 4.3:** Percent uncertainty values for significant contributions to particle diameter type B uncertainty for step mode measurements.

| Quantity | Value | Percent Uncertainty |
|---|---|---|
| Voltage | | |
| SRM 1964 | 1400 V | 0.04 |
| 60 nm AuNPs | 1500 V | 0.03 |
| 30 nm AuNPs | 450 V | 0.11 |
| Salt particles | 250 V | 0.08 |
| Slip correction | | |
| SRM 1964 | | 0 |
| 60 nm AuNPs | | 0.06 |
| 30 nm AuNPs | | 0.20 |
| 60 nm AuNP salt | | 0.69 |
| 30 nm AuNP salt | | 0.75 |
| Pressure | 101.33 kPa | 0.20 |
| Temperature | 296.15 K | 0.20 |
| SRM 1964 diameter | 60.39 nm | 0.51 |

**Table 4.4:** The uncertainty propagation of the gold nanoparticle diameter determination. The terms refer to the quantities within parenthesis in Equation 4.20.

| $D_p$, nm | $C_c$ | Term 1 $D_p$ for SRM | Term 2, $V$ | Term 3, $V$ for SRM | Term 4, $A$ | Term 5, $T$ | Term 6, $P$ | $u_r(D_p)$, % |
|---|---|---|---|---|---|---|---|---|
| 33.44 | 7.207 | 0.487 | 0.075 | 0.075 | 0.093 | 0.013 | 0.011 | 0.508 |
| 64.46 | 4.058 | 0.517 | 0.080 | 0.080 | 0.064 | 1.9E-3 | 1.6E-3 | 0.533 |

4.2.7.4 Combined Uncertainty

The type A and type B uncertainties calculated above were combined by adding the standard uncertainties in quadrature as shown in Equation 4.23.

$$u_{r,combined} = \sqrt{u_{r,Type\ A}^2 + u_{r,Type\ B}^2} \tag{4.23}$$

I express the final uncertainty results in terms of the expanded relative uncertainty (95% confidence interval), $U_r$, which is computed from a coverage factor, $k$, times the combined standard uncertainty. In the limit of an infinite number of degrees of freedom, $k = 2$. In our case, $k = 2.2$.

**Table 4.5:** The combined standard and expanded uncertainty values for the step voltage measurements.

| Particle | $D_{p,c}$, nm | Type B $u_r(D_{p,c})$, % | Type A $u_r(D_p)$, % | Combined $u_r(D_{p,c})$, % | Coverage Factor | Combined Expanded Uncertainty $U_r(D_p)$, % |
|---|---|---|---|---|---|---|
| QC1 | 32.92 | 0.508 | 0.314 | 0.615 | 2.2 | 1.35 |
| QC2 | 64.31 | 0.533 | 0.159 | 0.559 | 2.2 | 1.23 |

*4.2.8 SMPS*

The same system of nES, DMA, and CPC was used for the SMPS measurements (Figure 1.9). The same TSI flow meter was used to measure the temperature and pressure. AIM software version 9.0.0.0 was used. The primary differences were the recirculated sheath flow controlled by the SMPS (Model 3080, TSI) and the resulting "underpressure mode" measurement in which the

CPC pulls air through the DMA with a valve between the nES and DMA. The CPC was set to 0.3 L $min^{-1}$ low flow mode and the sheath flow was set to 6 L $min^{-1}$ resulting in the same flow ratio as the step voltage mode. A 0.0508 cm nozzle size impactor was installed in-line between the nES and DMA. The measurement time was set to 300 s scan up and 30 s scan down. The delay time ($t_d$) is the time required for the aerosol to flow through the DMA and the tubing connecting to the CPC, and was set to the default value for the given measurement conditions: 3.43 s. The software presents the data as diameter vs. $dN/dlogD_p$, where $dN/dlogD_p$ is the number size distribution which is related to the CPC number concentration by Equation 4.6. In order to calibrate the voltage and the sheath flow, I reverse this process to derive the raw data in terms of voltage (Equation 4.3) vs. number concentration (Equation 4.6) that is comparable to the step voltage measurements. QC1 was measured from 24.1 nm – 46.1 nm with 19 measurement points. QC2 was measured from 51.4 nm – 85.1 nm with 15 measurement points. The mode of SRM 1964 was measured from 47.8 nm – 71 nm with 12 measurement points.

### *4.3 Results*

Forty-eight total measurements were made of QC1 and QC2. Of these, twelve of QC1 were made in the step voltage mode, twelve of QC1 were made with the SMPS, twelve of QC2 were made in the step voltage mode, and twelve of QC2 were made with the SMPS. Each set of twelve measurements was made over three days, i.e., four per day. The SMPS data ware calibrated by two methods: using the known size of a certified size standard to calibrate the sheath flow or using the DryCal to calibrate the sheath flow. Each method additionally required accurate knowledge of the voltage, temperature, and pressure.

Test measurements were made using an alternative batch of 60 nm AuNPs. The results in Table 4.6 demonstrate the well documented scan speed issue, though in this case increasing the scan speed resulted in a decrease in the mean diameter.[101] Minimal change was observed above 150 s scan up time at the given measurement conditions (6 L $min^{-1}$ sheath flow, 50 nm – 85 nm scan, 16 data points). This effect was reduced by the particle calibration method, as both the size standard and the unknown particle changed size in the same direction. This effect is a shift in voltage (mobility); therefore, the correction works best for a size standard and unknown particle that are nominally the same size.

**Table 4.6:** The effect of scan time on mean particle size of 60 nm AuNPs by SMPS.

| | | Mean diameter (nm) and one standard deviation (STD) at given scan time | | |
|---|---|---|---|---|
| | | 30 s | 150 s | 300 s |
| Particle calibration | Mean | 63.78 | 63.82 | 63.87 |
| | STD | 0.28 | 0.05 | 0.05 |
| DryCal calibration | Mean | 62.37 | 63.56 | 63.67 |
| | STD | 0.24 | 0.06 | 0.04 |

Additionally, the delay time ($t_d$) was studied for the same test particles with results presented in Table 4.7. Even large changes in the delay time show minimal effect on the measured mean diameter for the given measurement settings (6 L $min^{-1}$ sheath flow, 50 nm – 85 nm scan, 16 data points, 300 s scan up, 30 s scan down). Minimizing the scan range reduced the error associated with an incorrect delay time.

**Table 4.7:** The effect of delay time ($t_d$) on mean particle size of 60 nm AuNPs by SMPS.

| Delay time (s) | Mean diameter (nm) |
|---|---|
| 3.33 | 64.06 |
| 3.43 | 64.11 |
| 3.53 | 64.01 |
| 4.00 | 63.97 |
| 6.00 | 63.90 |

The average size distributions for QC1 and QC2 by each calibration technique are presented in Figures 4.1 and 4.2, and the compiled mean diameter measurements are shown in Figures 4.3 and 4.4. The distributions measured by the SMPS and step voltage overlapped well for QC1 (Figure 4.1) with slight differences in the mean. However, some minor differences were seen for the measurements of QC2 (Figure 4.2). For the step voltage method, the background is slightly higher, and a minor secondary peak was reproducibly detected at 72 nm.

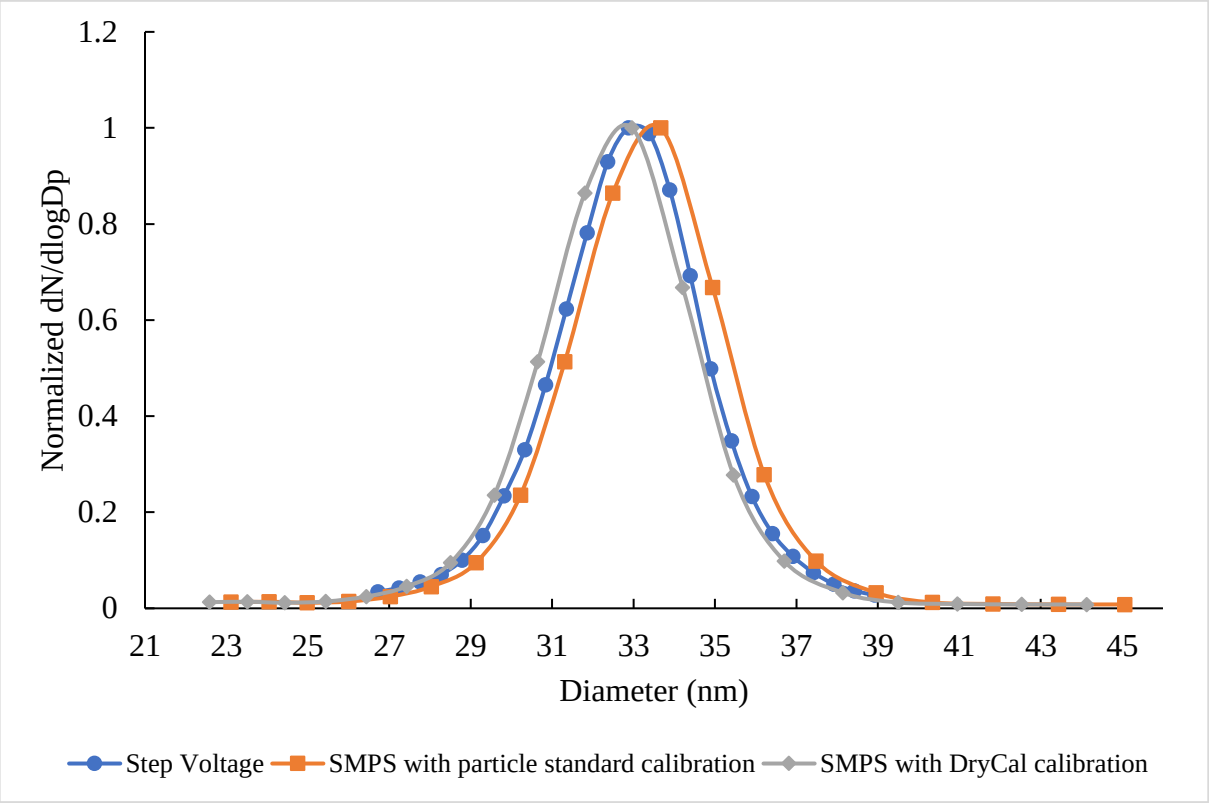


**Figure 4.1**: Average normalized size distributions of QC1. The blue circles are step voltage measurements, the orange squares are SMPS measurements with size standard calibration, and the gray diamonds are SMPS measurements with DryCal calibration.

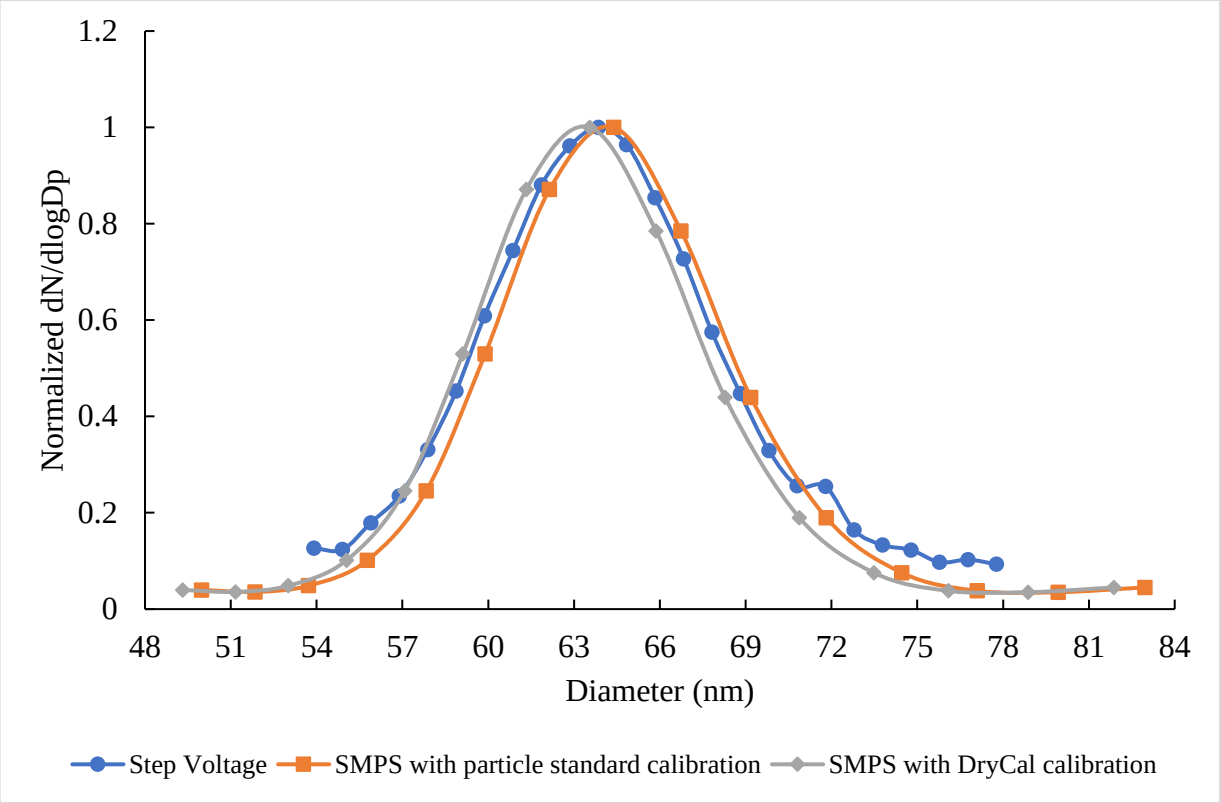


**Figure 4.2**: Average normalized size distributions of QC2. The blue circles are step voltage measurements, the orange squares are SMPS measurements with size standard calibration, and the gray diamonds are SMPS measurements with DryCal calibration. The orange and gray lines use the same raw data with different calibrations.

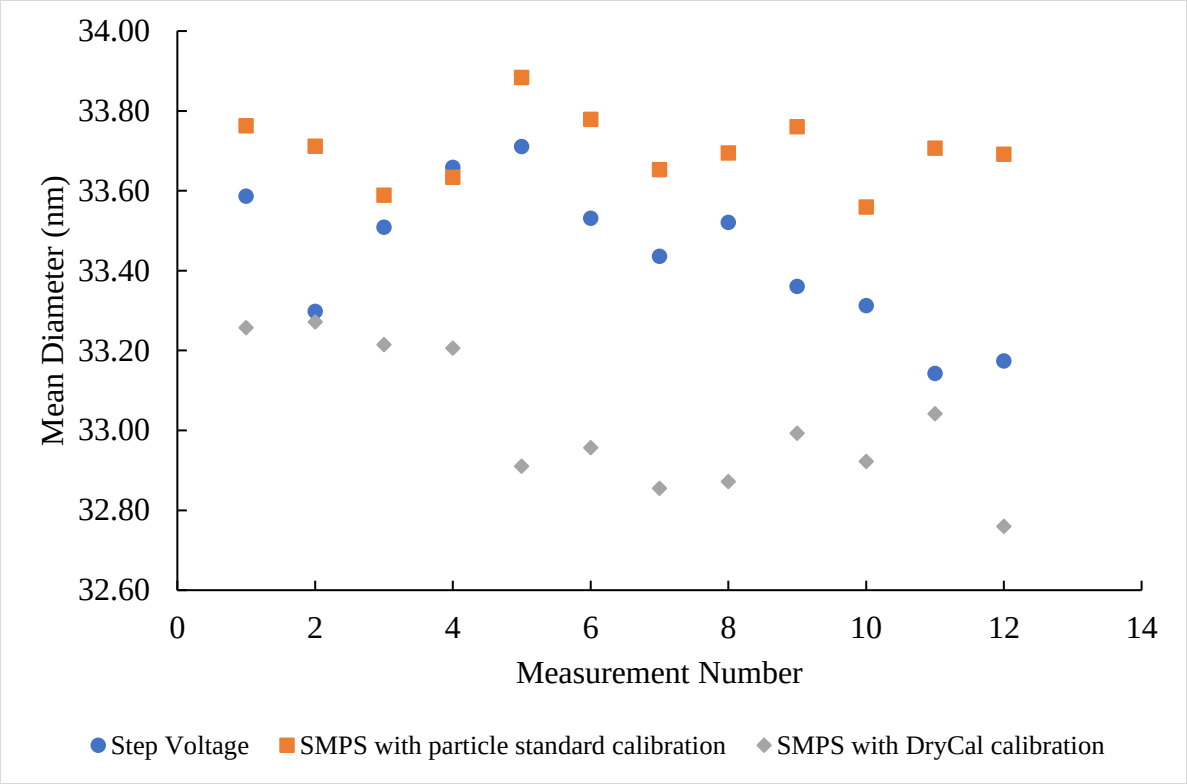


**Figure 4.3**: Repeat measurements of QC1 over six days. The blue circles are step voltage measurements, the orange squares are SMPS measurements with size standard calibration, and the gray diamonds are SMPS measurements with DryCal calibration. The orange and gray points use the same raw data with different calibrations. The size was corrected for the aerosol salt coating.

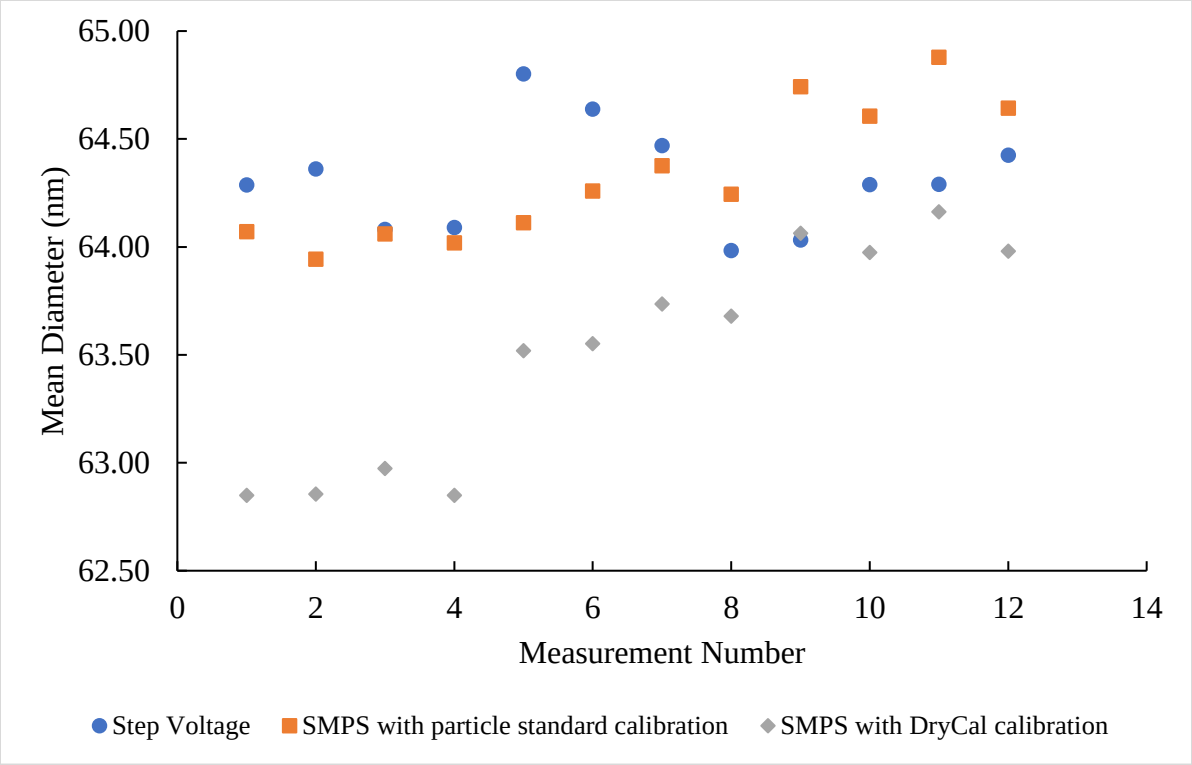


**Figure 4.4**: Repeat measurements of QC2 over six days. The blue circles indicate step voltage measurements, the orange squares indicate SMPS measurements with size standard calibration, and the gray diamonds indicate SMPS measurements with DryCal calibration. The orange and gray points use the same raw data with different calibrations. The size was corrected for the aerosol salt coating.

The mean of means for step voltage and SMPS measurements calibrated by SRM 1964 in Table 4.8 agree within the expanded uncertainty of the step voltage measurement. The size determined by the DryCal calibration of the SMPS is smaller than the other two measurements, but it also agrees within the expanded uncertainty of the step voltage measurement. The trend in terms of decreasing diameter is particle calibration of SMPS, step voltage, and DryCal calibration of SMPS. The data are presented with and without the salt correction ("aerosol" indicates the size of the aerosolized particle with a salt coating). The salt correction is the same for the three measurement approaches to limit variables. The measurement of the salt is simpler when using the

SMPS as a rapid test measurement can be made over the entire size distribution to identify the salt region and particle of interest region.

**Table 4.8:** The mean diameter of QC1 and QC2 for various measurement and calibration techniques with and without salt correction for aerosolized particles. The uncertainty for the step voltage particle calibration data is the combined type A and type B uncertainty with a coverage factor of 2.2. The uncertainty for the SMPS particle calibration and SMPS DryCal calibration is only the type A uncertainty.

| | | Mean diameter (nm) | |
|---|---|---|---|
| | | QC1 | QC2 |
| Step Voltage Particle Calibration | Aerosol | 33.44 ± 0.44 | 64.46 ± 0.79 |
| | Solution | 32.92 ± 0.45 | 64.31 ± 0.79 |
| SMPS Particle Calibration | Aerosol | 33.70 ± 0.05 | 64.49 ± 0.23 |
| | Solution | 33.19 ± 0.05 | 64.33 ± 0.23 |
| SMPS DryCal Calibration | Aerosol | 33.02 ± 0.16 | 63.68 ± 0.40 |
| | Solution | 32.48 ± 0.16 | 63.52 ± 0.40 |

One limitation of the SMPS is that the x-axis spacing is preset in the software, meaning that extra data points cannot be added over a given size range if the particle distribution is very narrow. This issue is illustrated in Figure 4.5, where the x-axis spacing is set much narrower in the step voltage mode which allows for improved peak definition (specifically for determining the mode) of the narrow size distribution of nominal 100 nm SRM 1963a.

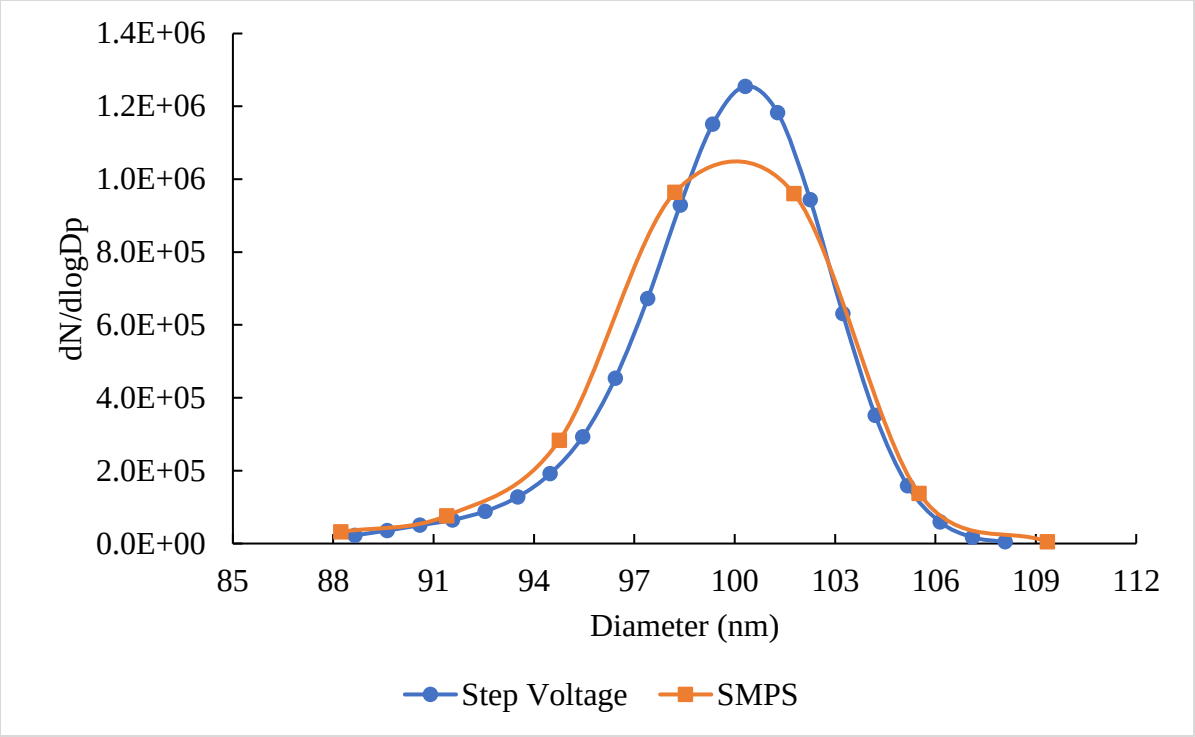


**Figure 4.5**: Size distribution of SRM 1963a measured by step voltage mode (blue circles) and SMPS with DryCal calibration (orange squares).

Table 4.9 illustrates differences between size measurements with all variables kept constant except for the method used to change the voltage. These measurements were made within a single day, alternating between step voltage and SMPS, thus day-to-day variability was eliminated and any change with time should affect both measurements. I found a ~0.5 nm bias between the step voltage and SMPS measurements of the mean diameters of QC1 and QC2, and a ~0.3 nm bias for the mode diameter of SRM 1964.

**Table 4.9**: The mean diameter of QC1 and QC2 by uncalibrated measurements using the same sheath flow alternating between scan voltage and step voltage mode. The uncertainty is one standard deviation of 8 (QC2) or 9 measurements (QC1).

| Measurement Method | | Mean diameter (nm) | | Mode diameter (nm) |
|---|---|---|---|---|
| | | QC1 | QC2 | SRM 1964 |
| Step Voltage | Aerosol | 34.55 ± 0.09 | 65.80 ± 0.20 | 63.09 ± 0.24 |
| SMPS | Aerosol | 34.13 ± 0.14 | 65.20 ± 0.27 | 62.83 ± 0.35 |

### *4.4 Discussion*

No significant difference was detected between the three measurement approaches: step voltage mode, SMPS calibrated by SRM 1964, and SMPS calibrated by the DryCal. The two SMPS calibration modes agreed within the error bars (the expanded combined uncertainty) of the step voltage measurement. The step voltage mode has been used most often for previous nanoparticle size standard certifications but there are a variety of advantages to using the SMPS for future measurements if a few lingering uncertainty terms are assessed. The recirculated sheath flow allows for running the system in "underpressure mode" where the CPC sets the aerosol flow rate. Under the conditions set for the step voltage measurements made here with an external mass flow controller, I found the pressure within the DMA to be 1.8 kPa higher than what was measured for the excess flow that has exited the DMA. In contrast, the data in Table 4.8 includes step voltage and scan voltage data using the recirculated sheath flow with no pressure build-up in the DMA. Even when this variable was accounted for, reproducible differences were detected between the step voltage mode and the SMPS. Another important difference is the sample run time. A complete step voltage measurement was made in 500 s while a SMPS measurement took 330 s. This was a conservative approach for the SMPS which can likely be dropped to 210 s without significant change to the measured mean diameter. Additionally, calibration with the DryCal can save a significant amount of time compared to the particle calibration method. Electrospray issues due to

incompatibility between the gold particles and SRM 1964 necessitated the use of unique capillaries for different particles. With the time saved from not changing and cleaning the capillaries as often, it would be possible to collect roughly twice as many measurements per day. Additionally, the shortened measurement time by SMPS reduces the effect of long-term sample source variability (drift on the order of minutes). Conversely, the step voltage measurements can average data over a longer period per data point to reduce short-term sample source variability (drift on the order of seconds). The long-term sample source variability tends to be the more relevant concern, particularly for distribution that are changing with time or particles that are colloidally unstable.

However, the SMPS is not applicable to all distributions. Specifically, when it is desirable to determine the mode of the distribution, generally five or more points are required where the y-axis signal is greater than or equal to half of the maximum y-axis signal ($N_i \geq 0.5\ N_{max}$). This criterion was narrowly missed for QC1 and QC2 with a CV of 5.1% and 6.8%, respectively. The distributions had enough points for the calculation of a mean, but a mode would be less well defined. In the case of SRM 1963a, with a coefficient of variation of 2.6%, the distribution is poorly defined for both a mean and a mode. I recommend a minimum coefficient of variation of 4% to determine a mean and 8% to determine a mode by SMPS.

I also recommend a direct comparison between step voltage mode and SMPS for the particles of interest. As demonstrated in Table 4.9, the SMPS measured a smaller size for the three particles studied here, but the size difference was not a constant mobility bias. In this case, calibration was able to correct most of the difference; however, that may not be true for all combinations of particles. For example, the difference for the mode of SRM 1964 was smaller than the bias for the mean of QC2 though the particles are nearly the same size.

An advantage to the particle calibration method is that it can simultaneously correct for the sheath flow, the dimensions of the DMA, and any non-ideal conditions regarding the particle transport. Also, the uncertainty in the slip correction term is reduced because the diameter of the standard is known. For example, if the unknown particle had the same mobility as the standard, the uncertainty in the slip correction would be zero. DMAS is not generally used as a primary standard, as persistent issues have been identified regarding the flow profiles at the entrance and exit slits, and non-ideal electric field behavior.[102,103,104] In this case, the SMPS measurements calibrated with the DryCal were just within the error bars of the step mode measurements, though the difference from the SMPS measurements calibrated by a size standard was larger.

An additional step was required for the calibration with a particle size standard. Generally, using the mode of the mobility distribution has been sufficient for calibration as it corresponds closely with the mode of the diameter distribution. However, in this case the mode of the mobility (voltage) distribution of SRM 1964 corresponded to a mode of the diameter distribution about 0.2 nm smaller than the certified diameter. This is likely due to the width of the distribution for SRM 1964. The diameter distribution corrects for the charging probability at different diameters. Due to the low charging probability for small particles, this correction increased the number of smaller particles more than that of larger particles and resulted in a slightly different mode. A correction was applied to set the sheath flow calibration based on the mode of the diameter distribution rather than the mobility distribution.

The mean diameter was determined using the lognormal distribution as this is the way the data are presented in the SMPS software. However, the same calculation can be made using $\frac{dN}{dD_p}$ instead of $\frac{dN}{dlogD_p}$ and the mode for $\frac{dN}{dD_p}$ was found to be consistently 0.1 nm larger than the $\frac{dN}{dlogD_p}$.

This can be important for the calibration procedure described here. It is important to verify how the calibration standard used was certified. In this case, SRM 1964 has a certified mode diameter that was determined using $\frac{dN}{dD_p}$.

### *4.5 Conclusions*

Comparison measurements of 30 nm and 60 nm AuNPs were presented for DMAS run in step voltage mode and scan voltage mode (SMPS). The step mode measurements were calibrated with a nanoparticle size standard, and the SMPS measurements were calibrated by two methods: a nanoparticle size standard and the DryCal direct measurement of the volumetric sheath flow rate. No significant difference was determined between the three different measurements: the step mode data (32.92 nm ± 0.45 nm and 64.31 nm ± 0.79 nm) were smaller than the sizes determined by the SMPS calibrated by a particle standard (33.19 nm and 64.33 nm). The SMPS measurements calibrated by the DryCal (32.48 nm and 63.52 nm) were smaller than the measurements calibrated by a particle standard, though they still agreed within the error bars of the step voltage measurements. Some important variables that influence the SMPS measurements are the measurement time, delay time, and measurement range. The effect of the scan rate was minimized by calibration with a nanoparticle size standard. Additionally, limitations to the SMPS measurements of monodisperse particles due to the predetermined diameter step spacing were characterized and minimum distribution widths were recommended for mean and modal measurements: 4% and 8% respectively. Finally, uncalibrated measurements made alternatively between step mode and SMPS on the same day for the same particles indicated a 0.5 nm smaller size measured by SMPS, though most of this bias was accounted for with a nanoparticle size

standard calibration (the calibration particle demonstrated a similar, though smaller, difference). Future work could investigate the source of this discrepancy, as it does not appear to be a bias in mobility as would be expected. Following a few guidelines included here and further investigation of the uncertainty analysis, future size certification measurements made with DMAS can be completed with the SMPS. This should result in more total measurements and therefore less concern about the statistical significance of the body of data.

# Chapter 5: Comparison of Traceable Nanoparticle Size Measurements

## *5.1 Introduction*

Nanoparticle size standards are an important tool for instrument calibration and validation. The use of the same standards can help promote coherence between difference techniques and increase reproducibility of experimental results.[105,106,107] Accurate standards are critical to fundamental studies in aerosol science where the particle diameter is present. These include the measurement of the Cunningham slip correction, diffusion coefficient, coagulation rate, and optical properties. An important aspect of standard certification is traceability, where the parameter of interest is linked to the relevant SI unit. For a nanoparticle size standard this involves relating the measured size to the meter. It is also critical that the measurement uncertainty be small. The smaller the combined uncertainty (random and systematic uncertainties), the more accurate the measurement.

A common approach for establishing traceability for nanoparticles has been the connection of a size measurement to the wavelength of light of various laser sources, as the wavelength of light is well known, and the uncertainty is very small. Ideally, the specific traceability pathway should not matter and various measurement techniques using a variety of traceability sources should result in the same solution. Good agreement has been demonstrated between nanoscale traceability methods based on the wavelength of light and crystal lattice length.[108] I further investigate this idea by comparing measurements of the same nanoparticles by four instruments with two difference traceability approaches.

Differential mobility analysis (DMAS), atomic force microscopy (AFM), and scanning electron microscopy (SEM) were all used to measure the size of the nominally 100 nm polystyrene latex (PSL) particles: JSR SC-010-S. These are nearly spherical particles with a monodisperse,

symmetrical size distribution. The measurements listed above were compared to reported measurements by electro-gravitational aerosol balance (EAB) of the same particles.[94] The DMAS measurements were calibrated with a size standard traceable to the wavelength of light through previous light scattering measurements. The AFM and SEM measurements were calibrated with size artifacts traceable to the wavelength of light through interferometry. The EAB is considered a primary measurement technique with a quantitative uncertainty budget, but it does not include traceability. The low uncertainty is a result of the direct connection between particle size and accurately known fundamental constants, material properties, and electrode spacing. The uncertainty for each technique is described, and possible reasons for the difference between results are discussed. For each measurement there are multiple factors affecting the uncertainty. For example, the SEM measurement has an uncertainty term associated with the repeatability of the measurements and a second term related to the determination of the particle boundary. These component uncertainties are combined into a combined uncertainty, $u_c$, by the law of propagation of uncertainty, often referred to as the "root-sum-of-squares" (RSS).[109] Ultimately the results are presented as the expanded uncertainty, which is an interval over which there is a 95% probability that the measurand (size) is in the interval. This uncertainty is computed with a coverage factor, $k$, multiplied by the combined uncertainty.

### *5.2 Materials*

Nominally 100 nm PSL particles JSR SC-010-S, nominally 100 nm PSL particles National Institute of Standards and Technology (NIST) SRM 1963a, and 18.2 MΩ·cm deionized water (Model 2121AL, Aqua Solutions, Jasper, GA, USA) were used. Ammonium acetate (>99.99%) was purchased from Sigma Aldrich (St. Louis, MO, USA).

## *5.3 Methods and Results*

### *5.3.1 Differential mobility analysis*

The DMAS measurements were made using a nano electrospray (nES) - differential mobility analyzer (DMA) - condensation particle counter (CPC) system (Figure 1.7). The long DMA (Model 3081, TSI, Shoreview, MN, USA) was used with a sheath flow of 20 L $min^{-1}$ and an aerosol flow rate of 1 L $min^{-1}$ air. Prior to measurement by DMAS, the particles were bath sonicated for five minutes, diluted by a factor of 10 using 18.2 MΩ·cm deionized water, passed through a 0.2 μm filter (Whatman, Maidstone, UK), and diluted again by a factor of 10 in 154 mg $L^{-1}$ ammonium acetate pH 8 (Sigma Aldrich, St. Louis, MO, USA). Particles were electrosprayed and then counted by a butanol CPC (Model 3776, TSI) operating at 1.5 L $min^{-1}$. The DMA was used in step voltage mode with a LabVIEW code (0.5 nm step and 30 s dwell time). The temperature and pressure of the sheath flow were measured immediately after exiting the DMA by a flow meter (Model 4043, TSI) with an accuracy of 1.0 K and 0.2 kPa. The power supply was calibrated with a voltage divider (Model HUD-100-1, Spellman, Hauppauge, NY, USA) and an accurate voltage meter (Model 34401A, Agilent Technologies, Santa Clara, CA, USA), within 0.03%. The slip correction values used are $\alpha$ = 1.165, $\beta$ = 0.483, and $\lambda$ = 0.997.[87]

The primary uncertainties are the diameter of the calibration standard (standard uncertainty ($u$) = 0.54 nm), repeatability of measurements ($u$ = 0.20 nm), mode voltage of the unknown particle ($u$ = 0.04 nm), mode voltage of the calibration particle ($u$ = 0.03 nm), and negligible contributions from the slip correction, temperature, and pressure. The combined standard uncertainty computed via RSS is 0.58 nm and the expanded uncertainty with a coverage factor of 2 is 1.2 nm.

Three measurements were made of nominally 100 nm PSL SRM 1963a and three were made of JSR SC-010-S. The six total distributions are shown in Figure 5.1, and each measured mean diameter of JSR SC-010-S is included in Table 5.1. The measurements of SRM 1963a were used as calibrations for the measurements of JSR SC-010-S. The mode of each SRM 1963a measurement was assigned to the certified value: 101.8 nm ± 1.1 nm. The sheath flow was adjusted so that the mobility diameter was equal to the certified value. This flow rate was then used in the subsequent measurement of JSR SC-010-S. Therefore, the DMAS measurement of JSR-SC-010-S is traceable to SRM 1963a. The number average diameter determined for JSR SC-010-S by this method was 100.1 nm ± 1.2 nm.

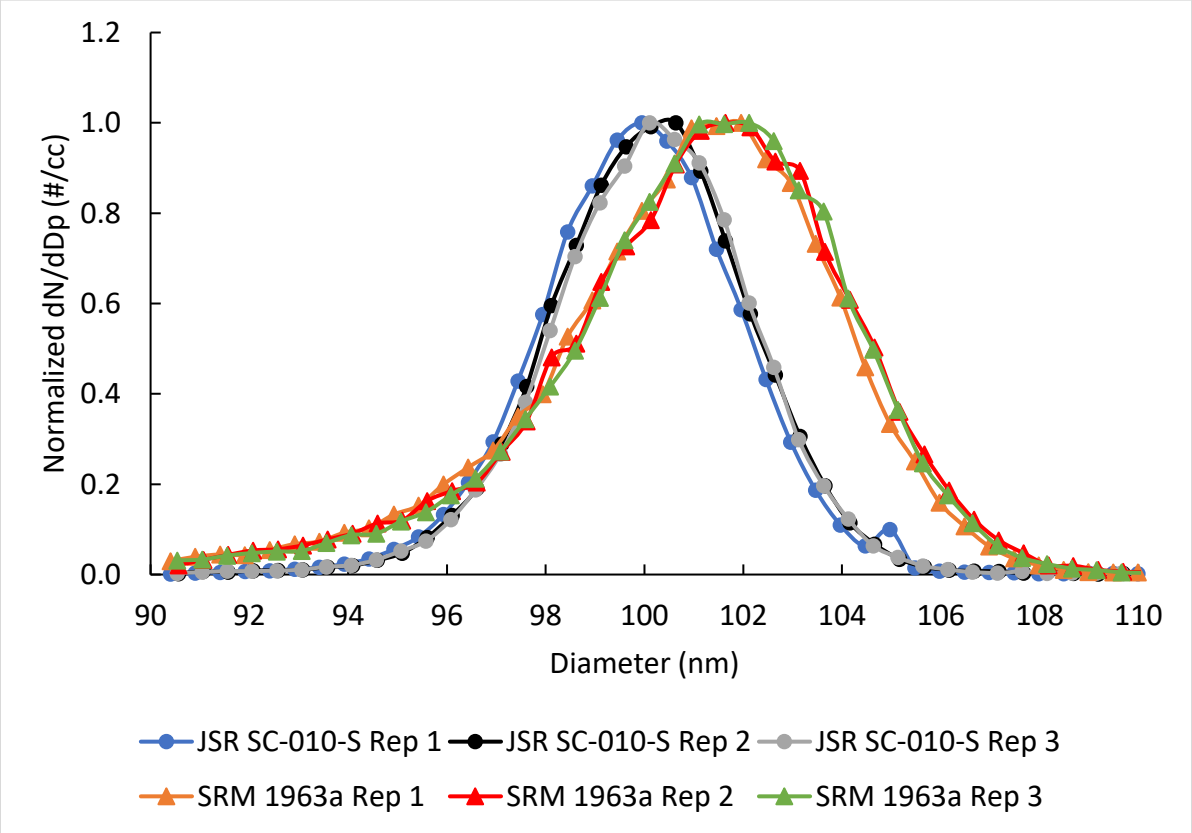


**Figure 5.1:** Comparison of DMAS size distribution measurements of JSR SC-010-S (circles) and calibrant SRM 1963a (triangles).

**Table 5.1:** Repeat DMAS measurements of JSR SC-010-S with the average and one standard deviation.

| Measurement | JSR SC-010-S number average diameter (nm) |
|---|---|
| 1 | 99.9 |
| 2 | 100.1 |
| 3 | 100.1 |
| Average | 100.1 ±0.1 |

*5.3.2 Atomic force microscopy*

Well-dispersed individual JSR SC-010-S nanoparticles were attached to a poly-L-lysine-coated mica substrate by leaving a 50-µL droplet of the sample on the substrate for several minutes. To remove unattached particles, the substrate was immersed in water followed by drying with air. AFM images of the samples were acquired under ambient conditions with a Veeco MultiMode AFM and Nanoscope IV controller. Nanoscope version 6 software was used for data acquisition. Imaging was performed in a tapping mode using Veeco OTESP cantilevers. Particle size by AFM is reported as height. The AFM was calibrated using a set of step height standards, which had been previously calibrated with the NIST Calibrated Atomic Force Microscope.[93] Their height values and uncertainties ($k$ = 2) are 6.6 nm ± 0.1 nm, 20.1 nm ± 0.3 nm, 67.7 nm ± 0.4 nm, 290.4 nm ± 0.9 nm, and 779.7 nm ± 2.7 nm.

The major components contributing to the measurement uncertainty of the particle height arise from repeatability of replicate measurements ($u$ = 0.7 nm), particle-substrate deformation ($u$ = 0.7 nm), background flatness ($u$ = 0.3 nm), and calibration ($u$ = 0.3 nm). The combined standard uncertainty is estimated via RSS. The expanded uncertainty calculated at the 95% confidence interval ($k$ = 2) for the AFM modal height measurements of JSR SC-010-S is 2.3 nm.

The height distribution obtained from individual particle measurements by AFM is shown in Figure 5.2 along with the modal value, coefficient of variation (one standard deviation of height

divided by mean value of height), and a representative AFM topography image. The AFM height data are corrected for calibration and for the estimated 3.2 nm particle-substrate deformation.[9] The number average height of JSR SC-010-S by AFM is 99.0 nm ± 2.3 nm.

The distributional quality of the JSR SC-010-S particles was also qualitatively assessed by AFM raft measurements. A 5-µL, dilute droplet of the sample was allowed to dry on a freshly-cleaved mica substrate. The particles raft well, forming close-packed arrays as shown in Figure 5.3 and exhibit high distributional uniformity, i.e. only a small percent of the particles are significantly smaller or larger than the mean.

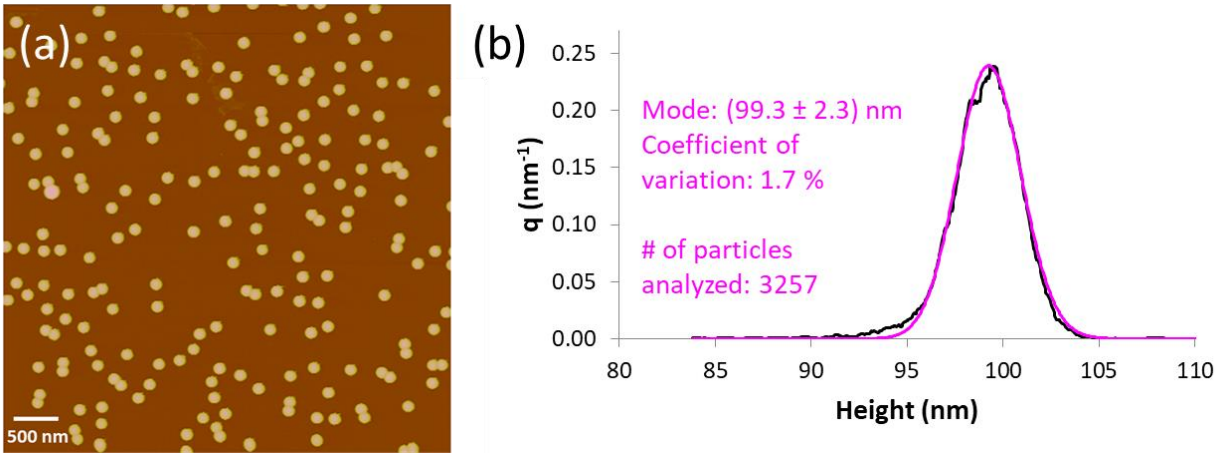


**Figure 5.2:** (a) Representative AFM topography image and (b) height distribution of JSR SC-010-S. The AFM height data are corrected for particle-substrate deformation. The mode and coefficient of variation is obtained from the lognormal fit (pink line) to the distribution.

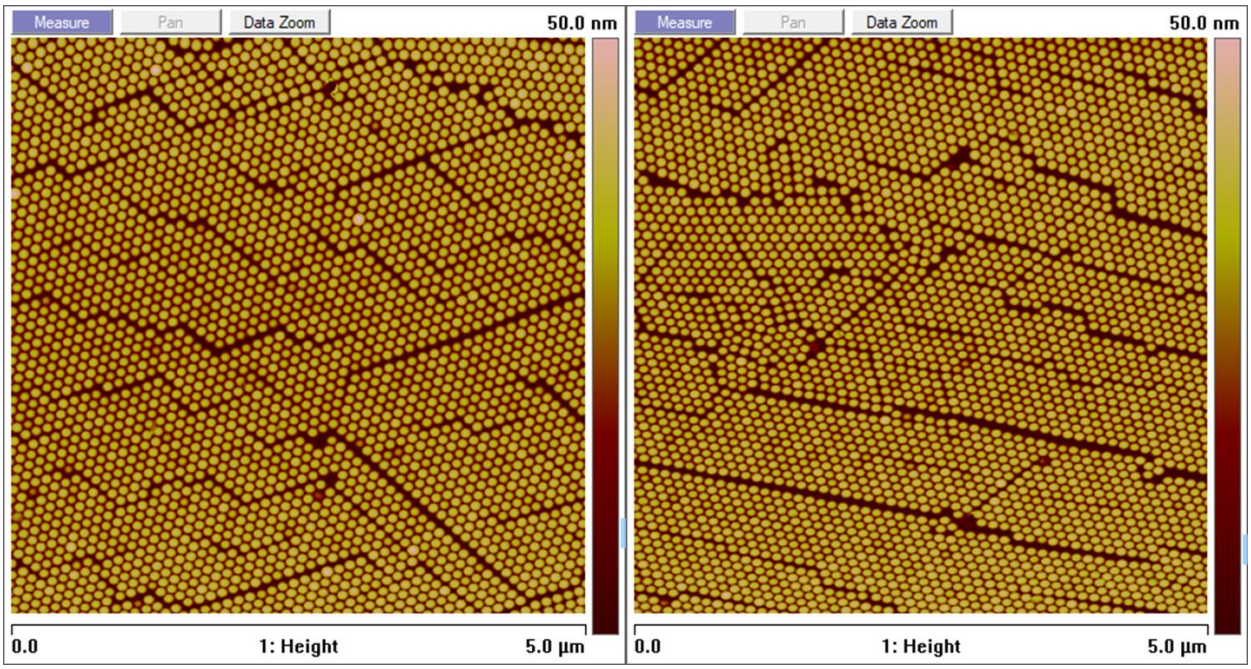


**Figure 5.3:** *AFM raft images of JSR SC-010-S.*

*5.3.3 Scanning electron microscopy*

Well-dispersed individual nanoparticles were attached to a poly-L-lysine-coated silicon substrate in the same manner as the samples prepared for AFM. The images were collected with an FEI Helios Dual-Beam SEM as deposited, without a conductive coating. Image analysis was conducted with ImageJ software. Particle size by SEM is reported as the area-equivalent diameter. The magnification of the SEM was calibrated using a 100 nm VLSI grating pitch standard, which had been previously calibrated with the NIST Calibrated Atomic Force Microscope. Its pitch value is 99.94 nm with an uncertainty of 0.06 nm ($k$ = 2).

The major components contributing to the measurement uncertainty of the mean area-equivalent diameter arise from the repeatability of replicate measurements ($u$ = 0.5 nm), determination of the particle boundary by thresholding ($u$ = 0.5 nm), non-uniformity of the background ($u$ = 0.5 nm), digitization of the particle projection area ($u$ = 0.4 nm), signal intensity

($u$ = 0.3 nm), beam alignment ($u$ = 0.3 nm), and instrument stage instabilities ($u$ = 0.3 nm). The combined standard uncertainty is estimated via RSS. The expanded uncertainty calculated at the 95% confidence interval ($k$ = 2) for the SEM mean size measurements of JSR SC-010-S is 2.2 nm.

The area-equivalent diameter distribution obtained from individual particle measurements by SEM is shown in Figure 5.4 along with the modal value, coefficient of variation, and a representative SEM image. The number average area-equivalent diameter of JSR SC-010-S by SEM is 98.8 nm ± 2.2 nm.

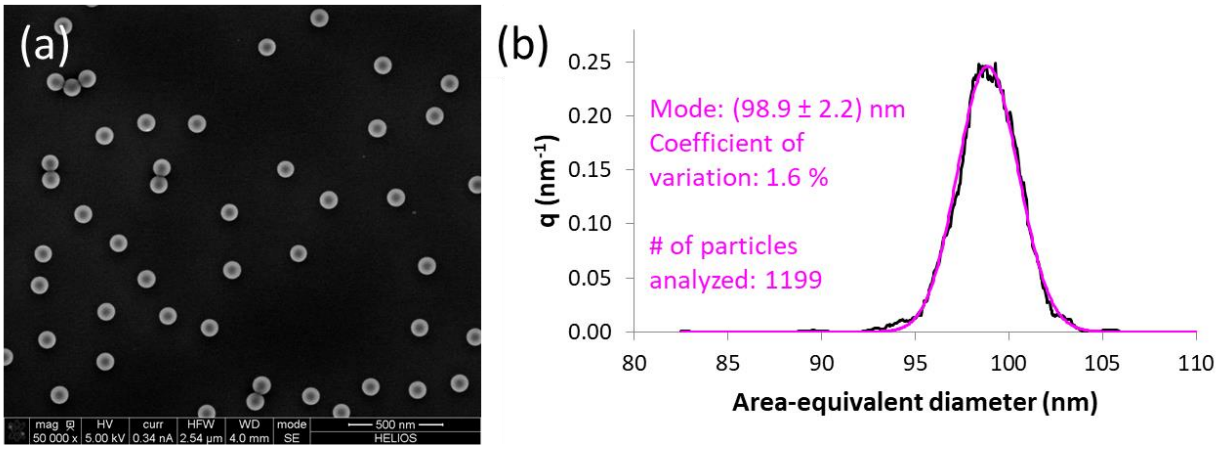


**Figure 5.4:** (a) Representative SEM image and (b) area-equivalent diameter distribution of JSR SC-010-S. The mode and coefficient of variation is obtained from the lognormal fit (pink line) to the distribution.

*5.3.4 Electro-Gravitational Aerosol Balance*

The EAB is a unique, large scale Millikan-cell type instrument that measures the loss of particles between parallel electrodes with various applied voltages to determine the mass of aerosolized particles.[110] With a known density and nearly spherical shape, this can be used to determine a number average diameter. A thorough uncertainty analysis investigated a variety of influences, such as thermophoresis, density measurements, space charge, thermal expansion of particles, and surface coating during drying, which were all found to be negligible. During the initial instrument validation, where measurements by EAB were compared to certified values for

seven PSL standards, the primary uncertainty terms were the voltage, distance between electrodes, gravity, and the least squares fitting of the survival function (derived from the loss of particles for a given holding time measured at several voltages).[111] Further analysis found that the work function of the electrodes contributed significantly to the measurement of 100 nm PSL particles. Measurements were made with a starting concentration between 760 particle $cm^{-3}$ – 950 particles $cm^{-3}$. Four combinations of electrode orientation (top vs. bottom) and polarity were used. A holding time of 7 h and a voltage range of 25 mV – 750 mV was used. 1.0632 g $cm^{-3}$ was used for the density of the PSL particles. Based on this recent analysis including the work function correction, a size of 101.71 nm ± 0.39 nm was determined for JSR SC-010-S.[94] The uncertainty is the combined uncertainty with a coverage factor of 2.

*5.3.5 Comparisons*

Figure 5.5 compares the AFM, SEM, and DMAS measurements of the JSR SC-010-S. The agreement between AFM and SEM is good with respect to the shape as well as the mean of the distributions. The distribution obtained by DMAS is slightly broader and shifted by about a nanometer to larger sizes. Table 5.2 and Figure 5.6 illustrate the different mean diameters determined by the four techniques with their associated uncertainties. An advantage of measuring JSR SC-010-S is that the measurands from the different techniques are expected to be nearly identical. DMAS measures mobility, AFM measures height, SEM measures area, and EAB measures mass, but all of the diameters derived from these different properties are expected to be nearly the same, as the particles are monodisperse and very spherical.

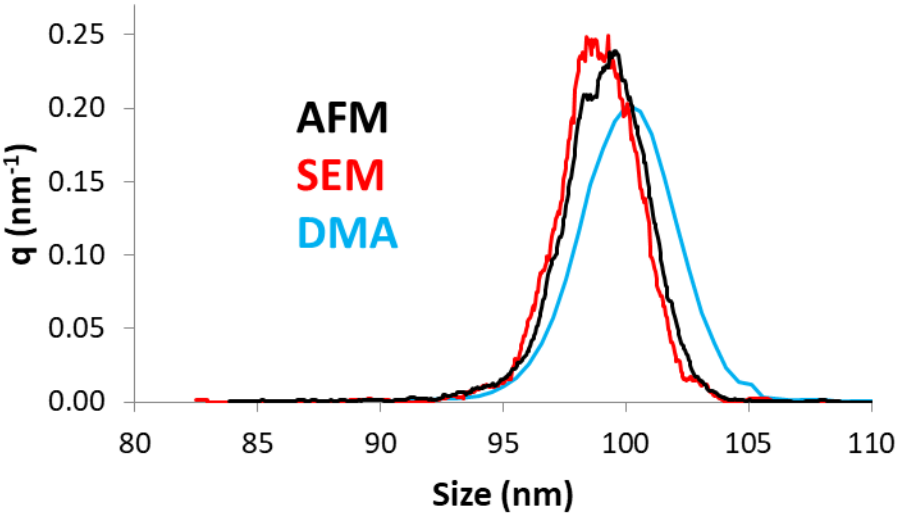


**Figure 5.5:** Comparison of the AFM, SEM, and DMAS distributions.

**Table 5.2:** Number average diameters of SRM 1963a and JSR SC-010-S determined by DMAS, AFM, SEM, and EAB.

| Instrument | Number average diameter (nm) | | Expanded uncertainty (k = 2) (nm) |
|---|---|---|---|
| - | SRM 1963a | JSR SC-010-S | |
| DMAS | 101.0 | 100.1 | 1.2 |
| SEM | 99.0 | 98.8 | 2.2 |
| AFM | 99.1 | 99.0 | 2.3 |
| EAB[94] | - | 101.7 | 0.4 |

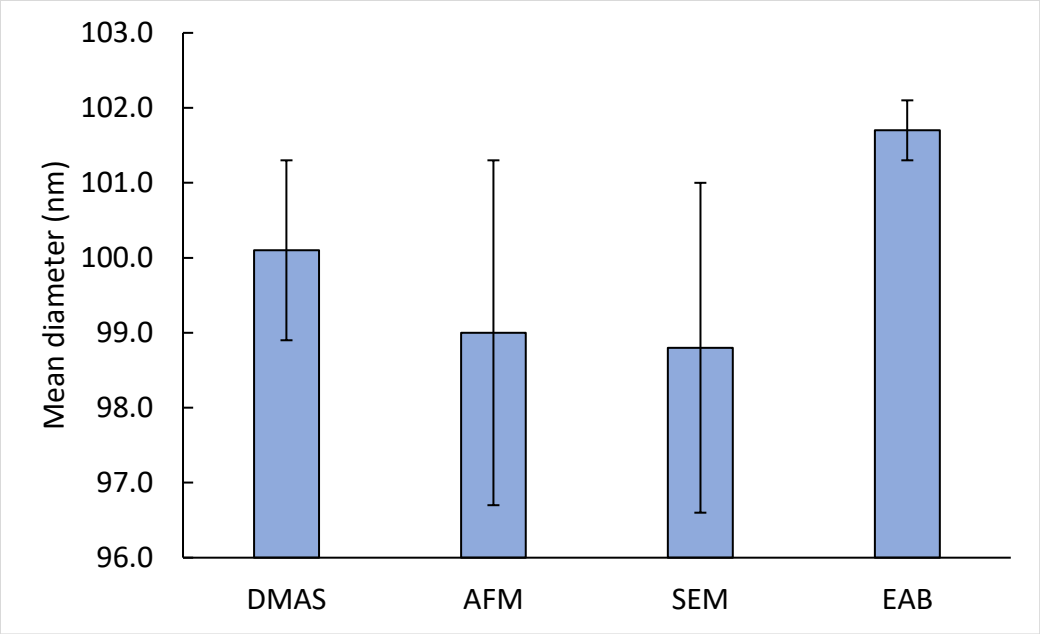


**Figure 5.6:** Comparison of the number average diameters of JSR SC-010-S determined by DMAS, AFM, SEM, and EAB. The error bars indicate the expanded uncertainties with a coverage factor of 2.

### *5.4 Discussion*

Different traceable standards were used for some of the measurements in this comparison. The DMAS measurements are traceable to the wavelength of light for a He-Ne laser (633 nm) used to determine the mean size of SRM 1690 by light scattering measurements of the particle suspension.[92] Nominally 1 μm PSL particles, SRM 1690 was validated by measuring the light scattering of the suspension using a different polarity of incident light, measuring the light scattering of individual aerosolized particles by two lasers independently, and measuring the row length of close-packed arrays with optical microscopy.[112] Each measurement included a detailed uncertainty analysis and all the results agreed within the uncertainty of the measurements, though the final certificate was tied specifically to the light scattering measurements of the suspension. SRM 1690 was used as a calibration particle for DMAS measurements of SRM 1963, nominally

100 nm PSL. Due to the large size of SRM 1690, the certification was completed using the +3 and +4 charge states, and good agreement was determined for the size of SRM 1963 calibrated by the two states.[98] Finally, due to aggregation, SRM 1963 was eventually replaced with SRM 1963a, also nominally 100 nm PSL. SRM 1963 was used as a calibration particle for DMAS measurements of SRM 1963a and SRM 1964 (nominally 60 nm PSL).[56] SRM 1963a also eventually aggregated, though techniques capable of differentiating monomers from larger aggregates, such as DMAS, can still use the particles as calibration particles traceable to the wavelength of light from the initial light scattering measurements of SRM 1690.

The AFM and SEM measurements are traceable to an Iodine-stabilized He-Ne laser (633 nm wavelength) used by the displacement interferometer in the calibrated AFM at NIST. The calibrated AFM is a carefully designed metrology grade instrument that is used to certify size standards such as the height and pitch standards used to calibrate the AFM and SEM measurements presented here.[93]

The EAB is used as a primary measurement of average particle mass, and it does not have any direct traceability. This may not be a large issue for particle size measurements, since the uncertainty in the particle diameter obtained by the other techniques is more than a decade larger than the uncertainty in the wavelength standard. On the other hand, the EAB theory relating the size of the particle to the electric field is rigorous and simple in comparison with the two traceable approaches. A thorough uncertainty analysis for the EAB was presented, and comparison measurements were made of several size standards certified by different measurements. Good agreement was determined for seven PSL particles ranging from 100 nm – 1000 nm, including a variety of traceable standards such as SRM 1963, SRM 1691, and SRM 1690. However, repeat measurements by the EAB over several years showed some drift in the measured size of JSR SC-

010-S and led to further uncertainty analysis. It was shown that the work function of the electrode had a significant and potentially temporally changing influence on the measurement due to electrode degradation. For the 100 nm PSL particles, the work function and the linear regression for the survival function were the largest contribution to the uncertainty and led to a new certified value for JSR SC-010-S: 101.71 nm ± 0.39 nm. The uncertainty analysis is complex because of the inclusion of correlation effects related to the work function of the electrodes. The presence of this previously unknown contribution to the measurement and uncertainty could alter the previous agreement between the EAB and other measurement techniques for the 100 nm PSL standards. The theory relating the size of the particle to the electric potential for the EAB measurements is rigorous and simple in comparison to the other instruments if there is not an issue with the work function, as is the case for larger particles. For a 300 nm particle, the nominal voltage would be 30 V, which is about 30 times larger than the value for the 100 nm particles. For the 300 nm particles the work function correction is minimal.

There are also some lingering uncertainty issues with the other techniques. For the case of the SEM, there is an issue determining where the physical edge of the particle is compared with the SEM image, or even what the edge of a particle means. In AFM, the sphericity of the particles is affected by surface forces when depositing the particles on a substrate during sample preparation, and by tip-particle deformation during imaging.[9] For DMAS, it is possible that the uncertainty associated with the slip correction, the relation between mobility and diameter for nanoscale aerosols, of the particle is larger than the current estimate. Many values have been reported for the empirical fits to the slip correction as knowledge of particle size and the mean free path of air improved, but only the values used here include a quantitative uncertainty analysis. Also, the effect of age on the size of the monomer calibration particles has not been studied. Over

the years, the PSL standards have been found to agglomerate. The particle size standards continue to be used, since the size of the primary particles appear to remain unchanged. However, there has been little effort to study the effect of a decade (or more) of aging on the primary sphere size. The SEM and AFM measurements involve particles on a surface, while DMAS and EAB measure the aerosolized particles after droplet evaporation. Perhaps the different environments affect the thickness of some unknown coating on the surface of the spheres. Ehara et al. estimated that the effect of nonvolatile impurities is negligible for the 100 nm PSL spheres.[111] However, it is possible that there is a surfactant coating that is not removed by centrifuging and resuspending the spheres. Also, it is possible that a coating of water (one or more layers) remains after drying and influences the microscopy differently than the aerosol measurements.[113]

The listed potential measurement biases have all been considered and corrected to the best of my current understanding, and the uncertainties in the corrections or the remaining uncorrected uncertainties are all included in the reported overall uncertainty estimates for the respective measurements. However, these are possible explanations for the discrepancy between the instruments. Regardless of the source of the difference in the measured size, the difference is significant and will likely lead to future disagreement. The EAB is being used to certify size standards by the National Metrology Institute of Japan (NMIJ), while the AFM and SEM methods described here may be used to certify the next generation size standards at NIST. The difference illustrated here is expected to also be true for these future standards, with the NIST values being slightly smaller and the NMIJ values being slightly larger and the error bars nearly overlapping. This may complicate future international comparisons as the results may vary depending on the source of calibration standard.

## *5.5 Conclusions*

The results represent a careful study of a nearly monodisperse nano-size spherical particle distribution using a variety of measurement methods. The total range in the number average diameters for the six measurements of the JSR SC-010-S is slightly less than 3% of the mean of the values. For many applications, the use of these standards would enhance the quality of size distribution measurements for aerosols and colloids. However, the 95% confidence intervals for some of the measurements barely overlap, raising the concern that some uncertainty components may have been underestimated or some measurement biases may have been overlooked. This difference may become significant as AFM, SEM, and EAB are intended to be used in the manner described here for the certification of future nanoparticle size standards. Improvements in these measurements or the use of other techniques such as small angle x-ray and neutron scattering are important for progress in fundamental aerosol and colloidal research.

# Chapter 6: Conclusion and Future Work

In this dissertation I have demonstrated some new uses for differential mobility analysis (DMAS). I have shown DMAS measurements of protein aggregation kinetics validated by asymmetrical flow field flow fractionation. This clarifies that DMAS can be used to measure aggregation in common protein formulations without significant changes to the measured rate due to the necessary buffer exchange into ammonium acetate. DMAS is a relatively fast measurement technique that requires minimal sample and therefore is ideal for expensive protein therapeutics such as monoclonal antibodies. I demonstrated a method for calibrated mass distribution measurements by DMAS with an inductively coupled plasma mass spectrometer (ICP-MS) for a detector. An ionic standard of certified mass concentration was sufficient to calibrate measurements of various gold nanoparticles. For polydisperse titania carrier particles coated with gold ($Au@TiO_2$), a multiple charge correction was necessary to improve the agreement with the ionic standard. The agreement may improve further with a thorough analysis of the spray source. I demonstrated good agreement between step voltage mode and scan voltage mode (SMPS) measurements of monodisperse gold nanoparticle samples by DMAS. Both measurements were calibrated with a traceable nanoparticle size standard, and a thorough uncertainty analysis was presented for the step voltage mode measurements. The same SMPS data calibrated by an alternative technique differed from the size standard calibration, though it was within the error bars of the step voltage mode measurement. Key parameters for the SMPS were analyzed, such as scan time, delay time, distribution width, and measurement range. The SMPS has the potential to improve future certifications of nanoparticle size standards due to the short measurement time. Finally, I demonstrated measurements of a 100 nm PSL size standard by four independent techniques: DMAS, scanning electron microscopy (SEM), atomic force microscopy (AFM), and

electro-gravitational aerosol balance (EAB). Two independent traceability pathways were used: one for DMAS, and one for SEM and AFM. EAB is considered a primary measurement due to its thorough uncertainty analysis, rigorous theory, and low uncertainty. The measurements agreed within 3%, though the error bars of EAB and the microscopy techniques did not overlap. This difference may prove to be significant if these techniques are used to certify future 100 nm size standards.

Several other projects showed promise but were not investigated thoroughly due to time limitations. A collaboration with Scott Brown at Chemours found that a specific batch of pegylated titania particles (R746) were undetectable by the condensation particle counter (CPC) when electrosprayed. The particles were detectable by the CPC when atomized and they were detectable by ICP-MS when electrosprayed. The CPC is generally considered a universal detector, except for a lower size limit, so it would be of interest to understand if and why a certain class of particles is not detectable. Also, as mentioned previously, some disagreement between the ionic standard and $Au@TiO_2$ was unresolved in chapter 3. Preliminary measurements indicate good agreement when a nebulizer was used instead of the nano electrospray (nES). The method presented in chapter 3 could be modified to use the nebulizer in place of the nES, or further work could be done to study the influence of the nES on the measurement. Measurements with the nebulizer would result in more droplet aggregation for particles around 100 nm and smaller, so determining representative mass distributions would be more complicated. Also, size certification measurements with DMAS were made with a variety of size standards for calibration. Significant differences were determined between values calibrated by SRM 1964, SRM 1963a, and JSR SC-010-S. Specifically of concern is the difference between SRM 1964 and SRM 1963a, as both particles were certified at the same time by DMAS. Perhaps there is has been some effect of aging on the primary sphere size over the

decade since their release. Comparison measurements of several standards by several measurement techniques may help to identify trends between standards. However, determining which standard is accurate may require repeating the initial traceable measurement, starting with the light scattering measurements of SRM 1690. Finally, efforts were made to negatively stain microscopy grids that were coated with particles post nES and DMA. Generally, particles such as proteins or nanocellulose were deposited for several hours at a concentration expected to apply good coverage, and then the grid was stained by pipetting a small volume of uranyl acetate onto the surface. Several minor variations of this approach failed to properly stain the particles, and a simpler solution may be to electrospray bionanoparticles dispersed in uranyl acetate or other heavy metal to dye the particles during aerosolization.

# References


(1) Schoenmaker, L.; Witzigmann, D.; Kulkarni, J. A.; Verbeke, R.; Kersten, G.; Jiskoot, W.; Crommelin, D. J. A. mRNA-Lipid Nanoparticle COVID-19 Vaccines: Structure and Stability. *Int. J. Pharm.* **2021**, *601*. DOI: 10.1016/j.ijpharm.2021.120586.
(2) Pardi, N.; Tuyishime, S.; Muramatsu, H.; Kariko, K.; Mui, B. L.; Tam, Y. K.; Madden, T. D.; Hope, M. J.; Weissman, D. Expression Kinetics of Nucleoside-Modified mRNA Delivered in Lipid Nanoparticles to Mice by Various Routes. *J. Control. Release* **2015**, *217*, 345-351. DOI: 10.1016/j.jconrel.2015.08.007.
(3) Kobayashi, H.; Brechbiel, M. W. Nano-Sized MRI Contrast Agents with Dendrimer Cores. *Adv. Drug Deliv. Rev.* **2005**, *57* (15), 2271-2286. DOI: 10.1016/j.addr.2005.09.016.
(4) Tenzer, S.; Docter, D.; Rosfa, S.; Wlodarski, A.; Kuharev, J.; Rekik, A.; Knauer, S. K.; Bantz, C.; Nawroth, T.; Bier, C.; et al. Nanoparticle Size Is a Critical Physicochemical Determinant of the Human Blood Plasma Corona: A Comprehensive Quantitative Proteomic Analysis. *ACS Nano* **2011**, *5* (9), 7155-7167. DOI: 10.1021/nn201950e.
(5) Bohren, C. F.; Huffman, D. R. *Absorption and Scattering of Light by Small Particles*; John Wiley & Sons, Inc., 1983.
(6) Blanchet, C. E.; Svergun, D. I. Small-Angle X-Ray Scattering on Biological Macromolecules and Nanocomposites in Solution. *Annu. Rev. Phys. Chem.* **2013**, *64*, 37-54. DOI: 10.1146/annurev-physchem-040412-110132.
(7) Gonzalez, A. L.; Noguez, C.; Ortiz, G. P.; Rodriguez-Gattorno, G. Optical Absorbance of Colloidal Suspensions of Silver Polyhedral Nanoparticles. *J. Phys. Chem. B* **2005**, *109* (37), 17512-17517. DOI: 10.1021/jp0533832.
(8) Egerton, R. F. Control of Radiation Damage in the TEM. *Ultramicroscopy* **2013**, *127*, 100-108. DOI: 10.1016/j.ultramic.2012.07.006.
(9) Dagata, J. A.; Farkas, N.; Kavuri, P.; Vladar, A. E.; Wu, C.-L.; Itoh, H.; Ehara, K. Method for Measuring the Diameter of Polystyrene Latex Reference Spheres by Atomic Force Microscopy. Special Publication (NIST SP) 260-185: 2016.
(10) Planken, K. L.; Colfen, H. Analytical Ultracentrifugation of Colloids. *Nanoscale* **2010**, *2* (10), 1849-1869. DOI: 10.1039/c0nr00215a.
(11) Knutson, E. O.; T., W. K. Aerosol Classification by Electric Mobility: Apparatus, Theory, and Applications. *Aerosol Sci.* **1975**, *6*, 443-451.
(12) Millikan, R. A. Coefficients of Slip in Gases and the Law of Reflection of Molecules from the Surfaces of Solids and Liquids. *Physical Review* **1923**, *21* (3), 217-238. DOI: 10.1103/PhysRev.21.217.
(13) Willeke, K. Temperature Dependence of Particle Slip in a Gaseous Medium. *J. Aerosol Sci.* **1976**, *7*, 381-387.
(14) Allen, M. D.; Raabe, O. G. Re-Evaluation of Millikan's Oil Drop Data for the Motion of Small Particles in Air. *J. Aerosol Sci.* **1982**, *13* (6), 537-547.
(15) Hamshere, J. L. The Mobility of Ions in Air. *Proc. R. Soc. Lond. A* **1930**, *127* (805), 298-314. DOI: 10.1098/rspa.1930.0059.
(16) Hewitt, G. W. The Charging of Small Particles for Electrostatic Precipitation. *Transactions of the American Institute of Electrical Engineers, Part 1: Communication and Electronics* **1957**, *76* (3), 300-306.
(17) Wang, S. C.; Flagan, R. C. Scanning Electrical Mobility Spectrometer. *Aerosol Sci. Technol.* **1990**, *13* (2), 230-240. DOI: 10.1080/02786829008959441.
(18) Chen, D. R.; Pui, D. Y. H.; Hummes, D.; Fissan, H.; Quant, F. R.; Sem, G. J. Design and Evaluation of a Nanometer Aerosol Differential Mobility Analyzer (Nano-DMA). *J. Aerosol Sci.* **1998**, *29* (5-6), 497-509. DOI: 10.1016/s0021-8502(97)10018-0.

(19) Kaufman, S. L. Analysis of Biomolecules Using Electrospray and Nanoparticle Methods: The Gas-Phase Electrophoretic Mobility Molecular Analyzer (GEMMA). *J. Aerosol Sci.* **1998**, *29* (5-6), 537-552. DOI: 10.1016/s0021-8502(97)00462-x.
(20) Tsai, D. H.; Pease, L. F.; Zangmeister, R. A.; Tarlov, M. J.; Zachariah, M. R. Aggregation Kinetics of Colloidal Particles Measured by Gas-Phase Differential Mobility Analysis. *Langmuir* **2009**, *25* (1), 140-146. DOI: 10.1021/la703164j.
(21) Guha, S.; Pease, L. F.; Brorson, K. A.; Tarlov, M. J.; Zachariah, M. R. Evaluation of Electrospray Differential Mobility Analysis for Virus Particle Analysis: Potential Applications for Biomanufacturing. *J. Virol. Methods* **2011**, *178* (1-2), 201-208. DOI: 10.1016/j.jviromet.2011.09.012.
(22) Li, M.; Guha, S.; Zangmeister, R.; Tarlov, M. J.; Zachariah, M. R. Method for Determining the Absolute Number Concentration of Nanoparticles from Electrospray Sources. *Langmuir* **2011**, *27* (24), 14732-14739. DOI: 10.1021/la202177s.
(23) Taylor, G. Disintegration of Water Drops in an Electric Field. *R. Soc. Lond.* **1964**, *280*, 383-397.
(24) Li, M. D.; Guha, S.; Zangmeister, R.; Tarlov, M. J.; Zachariah, M. R. Quantification and Compensation of Nonspecific Analyte Aggregation in Electrospray Sampling. *Aerosol Sci. Technol.* **2011**, *45* (7), 849-860. DOI: 10.1080/02786826.2011.566901.
(25) Ranz, W. E.; Wong, J. B. Impaction of Dust and Smoke Particles on Surface and Body Collectors. *Ind. Eng. Chem.* **1952**, *44* (6), 1371-1381. DOI: 10.1021/ie50510a050.
(26) Leppa, J.; Mui, W.; Grantz, A. M.; Flagan, R. C. Charge Distribution Uncertainty in Differential Mobility Analysis of Aerosols. *Aerosol Sci. Technol.* **2017**, *51* (10), 1168-1189. DOI: 10.1080/02786826.2017.1341039.
(27) Wiedensohler, A. An Approximation of the Bipolar Charge Distribution for Particles in the Submicron Size Range. *J. Aerosol Sci.* **1988**, *19*, 387-389.
(28) Hoppel, W. A.; Frick, G. M. The Nonequilibrium Character of the Aerosol Charge-Distributions Produced by Neutralizers. *Aerosol Sci. Technol.* **1990**, *12* (3), 471-496. DOI: 10.1080/02786829008959363.
(29) Agarwal, J. K.; Sem, G. J. Continuous-Flow, Single-Particle-Counting Condensation Nucleus Counter. *J. Aerosol Sci.* **1980**, *11* (4), 343-357. DOI: 10.1016/0021-8502(80)90042-7.
(30) Hering, S. V.; Stolzenburg, M. R.; Quant, F. R.; Oberreit, D. R.; Keady, P. B. A Laminar-Flow, Water-Based Condensation Particle Counter (WCPC). *Aerosol Sci. Technol.* **2005**, *39* (7), 659-672. DOI: 10.1080/02786820500182123.
(31) Yang, Y. X.; Yu, T. Z.; Zhang, J. S.; Wang, J.; Wang, W. Y.; Gui, H. Q.; Liu, J. G. On the Performance of an Aerosol Electrometer with Enhanced Detection Limit. *Sensors* **2018**, *18* (11). DOI: 10.3390/s18113889.
(32) Myojo, T.; Takaya, M.; Ono-Ogasawara, M. DMA as a Gas Converter from Aerosol to "Argonsol" for Real-Time Chemical Analysis using ICP-MS. *Aerosol Sci. Technol.* **2002**, *36* (1), 76-83. DOI: 10.1080/027868202753339096.
(33) Carazzone, C.; Raml, R.; Pergantis, S. A. Nanoelectrospray Ion Mobility Spectrometry Online with Inductively Coupled Plasma-Mass Spectrometry for Sizing Large Proteins, DNA, and Nanoparticles. *Anal. Chem.* **2008**, *80* (15), 5812-5818. DOI: 10.1021/ac7025578.
(34) Thomas, R. A Beginner's Guide to ICP-MS - Part III: The Plasma Source. *Spectroscopy* **2001**, *16* (6), 26-30.
(35) Thomas, R. A Beginner's Guide to ICP-MS - Part V: The Ion Focusing System. *Spectroscopy* **2001**, *16* (9), 38-44.
(36) Elzey, S.; Tsai, D. H.; Yu, L. L.; Winchester, M. R.; Kelley, M. E.; Hackley, V. A. Real-Time Size Discrimination and Elemental Analysis of Gold Nanoparticles Using ES-DMA Coupled to ICP-MS. *Anal. and Bioanal. Chem.* **2013**, *405* (7), 2279-2288. DOI: 10.1007/s00216-012-6617-z.

(37) Borzova, V. A.; Markossian, K. A.; Kleymenov, S. Y.; Kurganov, B. I. A Change in the Aggregation Pathway of Bovine Serum Albumin in the Presence of Arginine and its Derivatives. *Sci. Rep.* **2017**, *7*. DOI: 10.1038/s41598-017-04409-x.
(38) Weijers, M.; Barneveld, P. A.; Stuart, M. A. C.; Visschers, R. W. Heat-Induced Denaturation and Aggregation of Ovalbumin at Neutral pH Described by Irreversible First-Order Kinetics. *Protein Sci.* **2003**, *12* (12), 2693-2703. DOI: 10.1110/ps.03242803.
(39) Ejima, D.; Yumioka, R.; Arakawa, T.; Tsumoto, K. Arginine as an Effective Additive in Gel Permeation Chromatography. *J. Chromatogr. A* **2005**, *1094* (1-2), 49-55. DOI: 10.1016/j.chroma.2005.07.086.
(40) Burgess, R. R. A Brief Practical Review of Size Exclusion Chromatography: Rules of Thumb, Limitations, and Troubleshooting. *Protein Expr. Purif.* **2018**, *150*, 81-85. DOI: 10.1016/j.pep.2018.05.007.
(41) Clodfelter, D. K.; Nussbaum, M. A.; Reilly, J. Comparison of Free Solution Capillary Electrophoresis and Size Exclusion Chromatography for Quantitating Non-Covalent Aggregation of an Acylated Peptide. *J. Pharm. Biomed. Anal.* **1999**, *19* (5), 763-775. DOI: 10.1016/s0731-7085(98)00302-1.
(42) Moore, J. M. R.; Patapoff, T. W.; Cromwell, M. E. M. Kinetics and Thermodynamics of Dimer Formation and Dissociation for a Recombinant Humanized Monoclonal Antibody to Vascular Endothelial Growth Factor. *Biochemistry* **1999**, *38* (42), 13960-13967. DOI: 10.1021/bi9905516.
(43) Gabrielson, J. P.; Arthur, K. K.; Kendrick, B. S.; Randolph, T. W.; Stoner, M. R. Common Excipients Impair Detection of Protein Aggregates during Sedimentation Velocity Analytical Ultracentrifugation. *J. Pharm. Sci.* **2009**, *98* (1), 50-62. DOI: 10.1002/jps.21403.
(44) Pease, L. F.; Elliott, J. T.; Tsai, D. H.; Zachariah, M. R.; Tarlov, M. J. Determination of Protein Aggregation With Differential Mobility Analysis: Application to IgG Antibody. *Biotechnol. Bioeng.* **2008**, *101* (6), 1214-1222. DOI: 10.1002/bit.22017.
(45) Guha, S.; Wayment, J. R.; Tarlov, M. J.; Zachariah, M. R. Electrospray-Differential Mobility Analysis as an Orthogonal Tool to Size-Exclusion Chromatography for Characterization of Protein Aggregates. *J. Pharm. Sci.* **2012**, *101* (6), 1985-1994. DOI: 10.1002/jps.23097.
(46) Hofmeister, F. Zur Lehre von der Wirkung der Salze. *Arch. Exp. Path. Pharm.* **1888**, *24*, 247-260.
(47) Wahlund, K. G.; Giddings, J. C. Properties of an Asymmetrical Flow Field-Flow Fractionation Channel Having One Permeable Wall. *Anal. Chem.* **1987**, *59* (9), 1332-1339. DOI: 10.1021/ac00136a016.
(48) Li, Y.; Ogunnaike, B. A.; Roberts, C. I. Multi-Variate Approach to Global Protein Aggregation Behavior and Kinetics: Effects of pH, NaCl, and Temperature for alpha-Chymotrypsinogen A. *J. Pharm. Sci.* **2010**, *99* (2), 645-662. DOI: 10.1002/jps.21869.
(49) Gill, S. C.; Vonhippel, P. H. Calculation of Protein Extinction Coefficients from Amino-Acid Sequence Data. *Anal. Biochem.* **1989**, *182* (2), 319-326. DOI: 10.1016/0003-2697(89)90602-7.
(50) Hartley, B. S. Amino-Acid Sequence of Bovine Chymotrypsinogen-A. *Nature* **1964**, *201* (492), 1284-1287. DOI: 10.1038/2011284a0.
(51) Velev, O. D.; Kaler, E. W.; Lenhoff, A. M. Protein Interactions in Solution Characterized by Light and Neutron Scattering: Comparison of Lysozyme and Chymotrypsinogen. *Biophys. J.* **1998**, *75* (6), 2682-2697. DOI: 10.1016/s0006-3495(98)77713-6.
(52) M., S. *Handbook of Biochemistry*; The Chemical Rubber Co., 1970.
(53) Kaufman, S. L.; Skogen, J. W.; Dorman, F. D.; Zarrin, F.; Lewis, K. C. Macromolecule Analysis Based on Electrophoretic Mobility in Air: Globular Proteins. *Anal. Chem.* **1996**, *68* (11), 1895-1904. DOI: 10.1021/ac951128f.
(54) Guha, S.; Wayment, J. R.; Li, M. D.; Tarlov, M. J.; Zachariah, M. R. Protein Adsorption-Desorption on Electrospray Capillary Walls - No Influence on Aggregate Distribution. *J. Colloid Interface Sci.* **2012**, *377*, 476-484. DOI: 10.1016/j.jcis.2012.03.059.
(55) Kousaka, Y.; Okuyama, K.; Adachi, M. Determination of Particle-Size Distribution of Ultra-Fine Aerosols Using a Differential Mobility Analyzer. *Aerosol Sci. Technol.* **1985**, *4* (2), 209-225. DOI: 10.1080/02786828508959049.

(56) Mulholland, G. W.; Donnelly, M. K.; Hagwood, C. R.; Kukuck, S. R.; Hackley, V. A.; Pui, D. Y. H. Measurement of 100 nm and 60 nm Particle Standards by Differential Mobility Analysis. *J. Res. Natl. Inst. Stand. Technol.* **2006**, *111* (4), 257-312. DOI: 10.6028/jres.111.022.
(57) Taylor, J. R. *An Introduction to Error Analysis*; University Science Books, 1997.
(58) Andrews, J. M.; Roberts, C. J. Non-Native Aggregation of alpha-Chymotrypsinogen Occurs Through Nucleation and Growth with Competing Nucleus Sizes and Negative Activation Energies. *Biochemistry* **2007**, *46* (25), 7558-7571. DOI: 10.1021/bi700296f.
(59) Kayser, V.; Chennamsetty, N.; Voynov, V.; Forrer, K.; Helk, B.; Trout, B. L. Glycosylation Influences on the Aggregation Propensity of Therapeutic Monoclonal Antibodies. *Biotechnol. J.* **2011**, *6* (1), 38-44. DOI: 10.1002/biot.201000091. Spiegel, T. Whey Protein Aggregation under Shear Conditions - Effects of Lactose and Heating Temperature on Aggregate Size and Structure. *Int. J. Food Sci. Technol.* **1999**, *34* (5-6), 523-531. DOI: 10.1046/j.1365-2621.1999.00309.x.
(60) Chen, D. R.; Pui, D. Y. H.; Kaufman, S. L. Electrospraying of Conducting Liquids for Monodisperse Aerosol Generation in the 4 nm to 1.8 mu-m Diameter Range. *J. Aerosol Sci.* **1995**, *26* (6), 963-977. DOI: 10.1016/0021-8502(95)00027-a.
(61) Bendixen, N.; Losert, S.; Adlhart, C.; Lattuada, M.; Ulrich, A. Membrane-Particle Interactions in an Asymmetric Flow Field Flow Fractionation Channel Studied with Titanium Dioxide Nanoparticles. *J. Chromatogr. A* **2014**, *1334*, 92-100. DOI: 10.1016/j.chroma.2014.01.066.
(62) Gabrielson, J. P.; Brader, M. L.; Pekar, A. H.; Mathis, K. B.; Winter, G.; Carpenter, J. F.; Randolph, T. W. Quantitation of Aggregate Levels in a Recombinant Humanized Monoclonal Antibody Formulation by Size-Exclusion Chromatography, Asymmetrical Flow Field Flow Fractionation, and Sedimentation Velocity. *J. Pharm. Sci.* **2007**, *96* (2), 268-279. DOI: 10.1002/jps.20760.
(63) Hawe, A.; Friess, W.; Sutter, M.; Jiskoot, W. Online Fluorescent Dye Detection Method for the Characterization of Immunoglobulin G Aggregation by Size Exclusion Chromatography and Asymmetrical Flow Field Flow Fractionation. *Anal. Biochem.* **2008**, *378* (2), 115-122. DOI: 10.1016/j.ab.2008.03.050.
(64) Arosio, P.; Barolo, G.; Muller-Spath, T.; Wu, H.; Morbidelli, M. Aggregation Stability of a Monoclonal Antibody During Downstream Processing. *Pharm. Res.* **2011**, *28* (8), 1884-1894. DOI: 10.1007/s11095-011-0416-7.
(65) Lee, J. P.; Chen, D. C.; Li, X. X.; Yoo, S.; Bottomley, L. A.; El-Sayed, M. A.; Park, S.; Liu, M. L. Well-Organized Raspberry-Like Ag@Cu Bimetal Nanoparticles for Highly Reliable and Reproducible Surface-Enhanced Raman Scattering. *Nanoscale* **2013**, *5* (23), 11620-11624. DOI: 10.1039/c3nr03363e.
(66) Ashfaq, M.; Verma, N.; Khan, S. Copper/Zinc Bimetal Nanoparticles-Dispersed Carbon Nanofibers: A Novel Potential Antibiotic Material. *Mater. Sci. Eng. C Mater. Biol. Appl.* **2016**, *59*, 938-947. DOI: 10.1016/j.msec.2015.10.079.
(67) Turner, M.; Golovko, V. B.; Vaughan, O. P. H.; Abdulkin, P.; Berenguer-Murcia, A.; Tikhov, M. S.; Johnson, B. F. G.; Lambert, R. M. Selective Oxidation with Dioxygen by Gold Nanoparticle Catalysts Derived from 55-Atom Clusters. *Nature* **2008**, *454* (7207), 981-984. DOI: 10.1038/nature07194.
(68) White, R. J.; Luque, R.; Budarin, V. L.; Clark, J. H.; Macquarrie, D. J. Supported Metal Nanoparticles on Porous Materials. Methods and Applications. *Chem. Soc. Rev.* **2009**, *38* (2), 481-494. DOI: 10.1039/b802654h.
(69) Holm, A.; Goodman, E. D.; Stenlid, J. H.; Aitbekova, A.; Zelaya, R.; Diroll, B. T.; Johnston-Peck, A. C.; Kao, K. C.; Frank, C. W.; Pettersson, L. G. M.; et al. Nanoscale Spatial Distribution of Supported Nanoparticles Controls Activity and Stability in Powder Catalysts for CO Oxidation and Photocatalytic H-2 Evolution. *J. Am. Chem. Soc.* **2020**, *142* (34), 14481-14494. DOI: 10.1021/jacs.0c03842.
(70) Prieto, G.; Meeldijk, J. D.; de Jong, K. P.; de Jongh, P. E. Interplay between Pore Size and Nanoparticle Spatial Distribution: Consequences for the Stability of CuZn/SiO2 Methanol Synthesis Catalysts. *J. Catal.* **2013**, *303*, 31-40. DOI: 10.1016/j.jcat.2013.02.023.

(71) Chan, S. C.; Barteau, M. A. Preparation of Highly Uniform Ag/TiO2 and Au/TiO2 Supported Nanoparticle Catalysts by Photodeposition. *Langmuir* **2005**, *21* (12), 5588-5595. DOI: 10.1021/la046887k.
(72) Weyland, M.; Midgley, P. A.; Thomas, J. M. Electron Tomography of Nanoparticle Catalysts on Porous Supports: A New Technique Based on Rutherford Scattering. *J. Phys. Chem. B* **2001**, *105* (33), 7882-7886. DOI: 10.1021/jp011566s.
(73) Yang, Q.; Liu, W. X.; Wang, B. Q.; Zhang, W. N.; Zeng, X. Q.; Zhang, C.; Qin, Y. J.; Sun, X. M.; Wu, T. P.; Liu, J. F.; et al. Regulating the Spatial Distribution of Metal Nanoparticles within Metal-Organic Frameworks to Enhance Catalytic Efficiency. *Nat. Commun.* **2017**, *8*. DOI: 10.1038/ncomms14429.
(74) Munnik, P.; Velthoen, M. E. Z.; de Jongh, P. E.; de Jong, K. P.; Gommes, C. J. Nanoparticle Growth in Supported Nickel Catalysts during Methanation Reaction-Larger is Better. *Angew. Chem. Int. Ed.* **2014**, *53* (36), 9493-9497. DOI: 10.1002/anie.201404103.
(75) Gommes, C. J.; Prieto, G.; Zecevic, J.; Vanhalle, M.; Goderis, B.; de Jong, K. P.; de Jongh, P. E. Mesoscale Characterization of Nanoparticles Distribution Using X-Ray Scattering. *Angew. Chem. Int. Ed.* **2015**, *54* (40), 11804-11808. DOI: 10.1002/anie.201505359.
(76) Ohata, M.; Sakurai, H.; Nishiguchi, K.; Utani, K.; Gunther, D. Direct Analysis of Ultra-Trace Semiconductor Gas by Inductively Coupled Plasma Mass Spectrometry Coupled with Gas to Particle Conversion-Gas Exchange Technique. *Anal. Chim. Acta* **2015**, *891*, 73-78. DOI: 10.1016/j.aca.2015.06.048.
(77) Saetveit, N. J.; Bajic, S. J.; Baldwin, D. P.; Houk, R. S. Influence of Particle Size on Fractionation with Nanosecond and Femtosecond Laser Ablation in Brass by Online Differential Mobility Analysis and Inductively Coupled Plasma Mass Spectrometry. *J. Anal. At. Spectrom.* **2008**, *23* (1), 54-61. DOI: 10.1039/b709995a.
(78) Tan, J. J.; Cho, T. J.; Tsai, D. H.; Liu, J. Y.; Pettibone, J. M.; You, R. A.; Hackley, V. A.; Zachariah, M. R. Surface Modification of Cisplatin-Complexed Gold Nanoparticles and Its Influence on Colloidal Stability, Drug Loading, and Drug Release. *Langmuir* **2018**, *34* (1), 154-163. DOI: 10.1021/acs.langmuir.7b02354.
(79) Tan, J. J.; Liu, J. Y.; Li, M. D.; El Hadri, H.; Hackley, V. A.; Zechariah, M. R. Electrospray-Differential Mobility Hyphenated with Single Particle Inductively Coupled Plasma Mass Spectrometry for Characterization of Nanoparticles and Their Aggregates. *Anal. Chem.* **2016**, *88* (17), 8548-8555. DOI: 10.1021/acs.analchem.6b01544.
(80) Tan, J. J.; Yang, Y.; El Hadri, H.; Li, M. D.; Hackley, V. A.; Zachariah, M. R. Fast quantification of nanorod geometry by DMA-spICP-MS. *Analyst* **2019**, *144* (7), 2275-2283. DOI: 10.1039/c8an02250j.
(81) Pace, H. E.; Rogers, N. J.; Jarolimek, C.; Coleman, V. A.; Higgins, C. P.; Ranville, J. F. Determining Transport Efficiency for the Purpose of Counting and Sizing Nanoparticles via Single Particle Inductively Coupled Plasma Mass Spectrometry. *Anal. Chem.* **2011**, *83* (24), 9361-9369. DOI: 10.1021/ac201952t.
(82) Hess, A.; Tarik, M.; Losert, S.; Ilari, G.; Ludwig, C. Measuring Air Borne Nanoparticles for Characterizing Hyphenated RDD-SMPS-ICPMS Instrumentation. *J. Aerosol Sci.* **2016**, *92*, 130-141. DOI: 10.1016/j.jaerosci.2015.10.007.
(83) Peng, S.; Lee, Y. M.; Wang, C.; Yin, H. F.; Dai, S.; Sun, S. H. A Facile Synthesis of Monodisperse Au Nanoparticles and Their Catalysis of CO Oxidation. *Nano Res.* **2008**, *1* (3), 229-234, Article. DOI: 10.1007/s12274-008-8026-3.
(84) Cargnello, M.; Chen, C.; Diroll, B. T.; Doan-Nguyen, V. V. T.; Gorte, R. J.; Murray, C. B. Efficient Removal of Organic Ligands from Supported Nanocrystals by Fast Thermal Annealing Enables Catalytic Studies on Well-Defined Active Phases. *J. Am. Chem. Soc.* **2015**, *137* (21), 6906-6911, Article. DOI: 10.1021/jacs.5b03333.
(85) Taurozzi, J. S.; Hackley, V. A.; Wiesner, M. R. A Standardised Approach for the Dispersion of Titanium Dioxide Nanoparticles in Biological Media. *Nanotoxicology* **2013**, *7* (4), 389-401. DOI: 10.3109/17435390.2012.665506.

(86) Duelge, K. J.; Parot, J.; Hackley, V. A.; Zachariah, M. R. Quantifying Protein Aggregation Kinetics using Electrospray Differential Mobility Analysis. *J. Pharm. Biomed. Anal.* **2020**, *177*. DOI: 10.1016/j.jpba.2019.112845.
(87) Kim, J. H.; Mulholland, G. W.; Kukuck, S. R.; Pui, D. Y. H. Slip Correction Measurements of Certified PSL Nanoparticles Using a Nanometer Differential Mobility Analyzer (nano-DMA) for Knudsen Number from 0.5 to 83. *J. Res. Natl. Inst. Stand. Techol.* **2005**, *110* (1), 31-54. DOI: 10.6028/jres.110.005.
(88) Larriba-Andaluz, C.; Carbone, F. The Size-Mobility Relationship of Ions, Aerosols, and Other Charged Particle Matter. *J. Aerosol Sci.* **2021**, *151*. DOI: 10.1016/j.jaerosci.2020.105659.
(89) ISO 15900: Determination of Particle Size Distribution - Differential Electrical Mobility Analysis for Aerosol Particles. Geneva, 2020.
(90) He, M. L.; Dhaniyala, S. A Multiple Charging Correction Algorithm for Scanning Electrical Mobility Spectrometer Data. *J. Aerosol Sci.* **2013**, *61*, 13-26. DOI: 10.1016/j.jaerosci.2013.03.007.
(91) Fu, H. J.; Patel, A. C.; Holtzman, M. J.; Chen, D. R. A New Electrospray Aerosol Generator with High Particle Transmission Efficiency. *Aerosol Sci. Technol.* **2011**, *45* (10), 1176-1183. DOI: 10.1080/02786826.2011.582899.
(92) Mulholland, G. W.; Hartman, A. W.; Hembree, G. G.; Marx, E.; Lettieri, T. R. Development of a One-Micrometer-Diameter Particle-Size Standard Reference Material. *J. Res. Natl. Inst. Stand. Technol.* **1985**, *90* (1), 3-26. DOI: 10.6028/jres.090.001.
(93) Dixson, R.; Koning, R.; Tsai, V. W.; Fu, J.; Vorburger, T. V. Nanometer-Scale Dimensional Metrology with the NIST Calibrated Atomic Force Microscope. *Microsc. Microanal.* **1999**, *5*, 958-959.
(94) Takahata, K.; Sakurai, H.; Ehara, K. Accurate Determination of Mass and Diameter of Monodisperse Particles by the Electro-Gravitational Aerosol Balance: Correction for the Work Function Imbalance between the Electrode Surfaces. *Aerosol Sci. Technol.* **2020**, *54* (12), 1386-1398. DOI: 10.1080/02786826.2020.1787324.
(95) Elahi, N.; Kamali, M.; Baghersad, M. H. Recent Biomedical Applications of Gold Nanoparticles: A Review. *Talanta* **2018**, *184*, 537-556. DOI: 10.1016/j.talanta.2018.02.088.
(96) Lamberg, H.; Sippula, O.; Joutsensaari, J.; Ihalainen, M.; Tissari, J.; Lahde, A.; Jokiniemi, J. Analysis of High-Temperature Oxidation of Wood Combustion Particles Using Tandem-DMA Technique. *Combust. Flame* **2018**, *191*, 76-85. DOI: 10.1016/j.combustflame.2017.12.027.
(97) Gibson, E. R.; Hudson, P. K.; Grassian, V. H. Aerosol Chemistry and Climate: Laboratory Studies of the Carbonate Component of Mineral Dust and its Reaction Products. *Geophys. Res. Lett.* **2006**, *33* (13). DOI: 10.1029/2006gl026386.
(98) Mulholland, G. W.; Bryner, N. P.; Croarkin, C. Measurement of the 100 nm NIST SRM 1963 by Differential Mobility Analysis. *Aerosol Sci. Technol.* **1999**, *31* (1), 39-55. DOI: 10.1080/027868299304345.
(99) DerSimonian, R.; Laird, N. Meta-Analysis in Clinical Trials. *Control. Clin. Trials* **1986**, *7*, 177-188.
(100) Higgins, J. P. T.; Thompson, S. G.; Spiegelhalter, D. J. A Re-Evaluation of Random-Effects Meta-Analysis. *J. R. Stat. Soc. Ser. A Stat. Soc.* **2009**, *172*, 137-159. DOI: 10.1111/j.1467-985X.2008.00552.x.
(101) Tokonami, S.; Knutson, E. O. The Scan Time Effect on the Particle Size Distribution Measurement in the Scanning Mobility Particle Sizer System. *Aerosol Sci. Technol.* **2000**, *32* (3), 249-252. DOI: 10.1080/027868200303786.
(102) Kinney, P. D.; Pui, D. Y. H.; Mulholland, G. W.; Bryner, N. P. Use of the Electrostatic Classification Method to Size 0.1 mu-m SRM Particles - A Feasibility Study. *J. Res. Natl. Inst. Stand. Technol.* **1991**, *96* (2), 147-176. DOI: 10.6028/jres.096.006.
(103) Chen, D. R.; Pui, D. Y. H.; Mulholland, G. W.; Fernandez, M. Design and Testing of an Aerosol Sheath Inlet for High Resolution Measurements with a DMA. *J. Aerosol Sci.* **1999**, *30* (8), 983-999. DOI: 10.1016/s0021-8502(98)00767-8.
(104) Mai, H. J.; Flagan, R. C. Scanning DMA Data Analysis I. Classification Transfer Function. *Aerosol Sci. Technol.* **2018**, *52* (12), 1382-1399. DOI: 10.1080/02786826.2018.1528005.

(105) Bustos, A. R. M.; Petersen, E. J.; Possolo, A.; Winchester, M. R. Post hoc Interlaboratory Comparison of Single Particle ICP-MS Size Measurements of NIST Gold Nanoparticle Reference Materials. *Anal. Chem.* **2015**, *87* (17), 8809-8817. DOI: 10.1021/acs.analchem.5b01741.
(106) Wiedensohler, A.; Birmili, W.; Nowak, A.; Sonntag, A.; Weinhold, K.; Merkel, M.; Wehner, B.; Tuch, T.; Pfeifer, S.; Fiebig, M.; et al. Mobility Particle Size Spectrometers: Harmonization of Technical Standards and Data Structure to Facilitate High Quality Long-Term Observations of Atmospheric Particle Number Size Distributions. *Atmos. Meas. Tech.* **2012**, *5* (3), 657-685. DOI: 10.5194/amt-5-657-2012.
(107) Koenders, L.; Bergmans, R.; Garnaes, J.; Haycocks, J.; Korolev, N.; Kurosawa, T.; Meli, F.; Park, B. C.; Peng, G. S.; Picotto, G. B. Comparison on Nanometrology: Nano 2-Step Height. *Metrologia* **2003**, *40*. DOI: 10.1088/0026-1394/40/1a/04001.
(108) Dai, G. L.; Koenders, L.; Fluegge, J.; Bosse, H. Two Approaches for Realizing Traceability in Nanoscale Dimensional Metrology. *Opt. Eng.* **2016**, *55* (9). DOI: 10.1117/1.oe.55.9.091407.
(109) Taylor, B. N.; Kuyatt, C. E. Guidelines for Evaluating and Expressing the Uncertainty of NIST Measurement Results. Commerce, D. o., Ed.; National Institute of Standards and Technology: 1994; pp 1-20.
(110) Ehara, K.; Takahata, K.; Koike, M. Absolute Mass and Size Measurement of Monodisperse Particles Using a Modified Millikan's Method: Part I - Theoretical Framework of the Electro-Gravitational Aerosol Balance. *Aerosol Sci. Technol.* **2006**, *40* (7), 514-520. DOI: 10.1080/02786820600714379.
(111) Ehara, K.; Takahata, K.; Koike, M. Absolute Mass and Size Measurement of Monodisperse Particles Using a Modified Millikan's Method: Part II - Application of Electro-Gravitational Aerosol Balance to Polystyrene Latex Particles of 100 nm to 1 mu m in Average Diameter. *Aerosol Sci. Technol.* **2006**, *40* (7), 521-535. DOI: 10.1080/02786820600714387.
(112) Marx, E.; Mulholland, G. W. Size and Refractive-Index Determination of Single Polystyrene Spheres. *J. Res. Natl. Bur. Stand.* **1983**, *88* (5), 321-338. DOI: 10.6028/jres.088.016.
(113) Yesilbas, M.; Boily, J. F. Particle Size Controls on Water Adsorption and Condensation Regimes at Mineral Surfaces. *Sci. Rep.* **2016**, *6*. DOI: 10.1038/srep32136.